Spectroscopy of exotic charm mesons from lattice QCD

Gavin Cheung

St John's College

University of Cambridge

Department of Applied Mathematics and Theoretical Physics

Faculty of Mathematics

Supervisor: Dr. Christopher Thomas

This dissertation is submitted for the degree of Doctor of Philosophy.

July 2018

Declaration

This dissertation is the result of my own work and includes nothing which is the outcome of work done in collaboration except as declared in the Preface and specified in the text.

It is not substantially the same as any that I have submitted, or, is being concurrently submitted for a degree or diploma or other qualification at the University of Cambridge or any other University or similar institution except as declared in the Preface and specified in the text. I further state that no substantial part of my dissertation has already been submitted, or, is being concurrently submitted for any such degree, diploma or other qualification at the University of Cambridge or any other University or similar institution except as declared in the Preface and specified in the text.

Signed _____

(Gavin Cheung)

Date _____

Summary

Exotic mesons are mesons that cannot be described as a quark-antiquark pair. The number of exotic mesons has been growing every year in the charm sector and the theoretical understanding of them is often conflicted amongst the community. Some possible explanations include hybrid mesons where the quark-antiquark pair is coupled to a gluonic excitation, compact tetraquarks where four quarks are bound into a localised state and molecules which consists of pairs of extended mesons. To study exotic mesons from first principles, lattice QCD provides the framework to perform spectroscopy calculations numerically. I will give a review and describe the relevant techniques used in this thesis.

After doing so, I will calculate masses of charmonium with angular momentum up to four. The results show QCD permits states with exotic quantum numbers that are not accessible by a quark-antiquark pair. I will identify states that are consistent with the quark-antiquark picture and then show that the remaining states in the extracted spectra can be interpreted to be the lightest and first excited hybrid meson supermultiplet.

Whilst the mass is one quantity that can be computed, hadron spectroscopy is also concerned with the calculation of the unstable properties of resonances which can decay into meson-meson states. These meson-meson states have four quarks and could also mix with tetraquarks. I will describe how to correctly extract the energies of four quark states within lattice QCD by reviewing operators resembling meson-mesons and then constructing a general class of operators resembling tetraquarks. I will then calculate a variety of spectra in the isospin-1 hidden charm sector and the doubly charmed sector. No evidence of a bound state or narrow resonance is found in these channels.

Having described how to include multi-meson states in lattice QCD, I will describe how to relate the lattice QCD spectrum to the scattering amplitudes and perform a calculation of elastic DK scattering amplitudes which is relevant for the exotic $D_{s0}(2317)$. By analytically continuing the scattering amplitudes into the complex plane, I find a bound state pole near threshold which is in good agreement with what is found experimentally.

Acknowledegments

Firstly, I would like to thank the Cambridge European Trust, St John's College and the Science and Technology Facilities Council (STFC) [grant number ST/P000681/1] for funding my studies.

This work used the DiRAC Data Analytic system at the University of Cambridge, operated by the University of Cambridge High Performance Computing Service on behalf of the STFC DiRAC HPC Facility (www.dirac.ac.uk). This equipment was funded by BIS National E-infrastructure capital grant ST/K001590/1, STFC capital grants ST/H008861/1 and ST/H00887X/1, and STFC DiRAC Operations grant ST/K00333X/1. This work also used the DiRAC Complexity system, operated by the University of Leicester IT Services, which forms part of the STFC DiRAC HPC Facility (www.dirac.ac.uk). This equipment is funded by BIS National E-Infrastructure capital grant ST/K000373/1 and STFC DiRAC Operations grant ST/K0003259/1. DiRAC is part of the National E-Infrastructure. Computations were also performed at Jefferson Laboratory under the USQCD Initiative, the LQCD ARRA project and the Scientific Discovery through Advanced Computing (ScIDAC) program.

The software codes `Chroma` [1], `QUDA` [2, 3], `QPhiX` [4], and `QOPQDP` [5, 6] were used to compute the propagators required for this project. This work also used the Wilkes GPU cluster at the University of Cambridge High Performance Computing Service (http://www.hpc.cam.ac.uk/), provided by Dell Inc., NVIDIA and Mellanox, and part funded by STFC with industrial sponsorship from Rolls Royce and Mitsubishi Heavy Industries.

This research was supported in part under an ALCC award, and used resources of the

Oak Ridge Leadership Computing Facility at the Oak Ridge National Laboratory, which is supported by the Office of Science of the U.S. Department of Energy under Contract No. DE-AC05-00OR22725. This research is also part of the Blue Waters sustained-petascale computing project, which is supported by the National Science Foundation (awards OCI-0725070 and ACI-1238993) and the state of Illinois. Blue Waters is a joint effort of the University of Illinois at Urbana-Champaign and its National Center for Supercomputing Applications. This work is also part of the PRAC "Lattice QCD on Blue Waters". This research used resources of the National Energy Research Scientific Computing Center (NERSC), a DOE Office of Science User Facility supported by the Office of Science of the U.S. Department of Energy under Contract No. DEAC02-05CH11231. I acknowledge the Texas Advanced Computing Center (TACC) at The University of Texas at Austin for providing HPC resources that have contributed to the research results reported within this work.

Gauge configurations were generated using resources awarded from the U.S. Department of Energy INCITE program at the Oak Ridge Leadership Computing Facility, the NERSC, the NSF Teragrid at the TACC and the Pittsburgh Supercomputer Center, as well as at Jefferson Lab.

Last but not least, I would like to express my gratitude to my supervisor, Christopher Thomas, for all the time and effort that he has given me. This work would not be possible without his guidance. I thank my collaborators in the Hadron Spectrum Collaboration who have offered substantial help towards my studies. I also thank my officemates Judd Harrison and Antoni Woss for all the good times. Finally, I thank all my family and friends who I can see again after this thesis.

Contents

Chapter 1

Introduction

In an attempt to describe all hadrons, Gell-Man [7] and Zweig [8] proposed in 1964 that hadrons are composite particles where the fundamental particles are fermions with fractional electrical charge called quarks. The field theory description of quarks, with the strong interaction mediated through gluons, is given by quantum chromodynamics (QCD) which has highly non-trivial behaviour across different energy scales. In the high-energy regime, QCD exhibits asymptotic freedom and the quarks interact weakly [9, 10]. On the other end of the spectrum, the quarks are confined, impossible to isolate freely, and form the hadrons that we observe at low-energies. Even today, this mechanism, for confinement in QCD and the crossover between scales, is not yet fully understood.

Motivated by QCD and phenomenology, a simpler model of mesons can be made within a constituent quark model where mesons consist of a constituent quark and antiquark bound by some interacting potential. It is important to distinguish between the quark fields that enter in the QCD Lagrangian, and constituent quarks which are quasiparticles and enter as the effective degrees of freedom. The constituent quarks can be thought of to arise from the dressing of the quark fields by the sea of gluons, quarks and antiquarks: their properties and interactions are determined phenomologically. The potential between the two constituent quarks is dominated by a spin-independent term, that is approximately Coulombic at short distances and linearly confining at large distances, to reproduce the properties of QCD. Other terms can be included in the potential such as a spin-spin or spin-orbit term. The spins of the quark and antiquark couple to give the total spin S which then couples to the relative orbital angular momentum L between the quark-antiquark to give total angular momentum J. Energies of the states are obtained from solutions to the Schrödinger equation which are labelled by $n^{2S+1}L_J$ where

n is the radial quantum number. The parity of a state is given by $P = (-1)^{L+1}$ and the charge conjugation symmetry is $C = (-1)^{L+S}$. From this, the $L = 0$ multiplet contains states $J^{PC} = 0^{-+}, 1^{--}$; the $L = 1$ multiplet contains states $J^{PC} = 1^{+-}, 0^{++}, 1^{++}, 2^{++}$; the $L = 2$ multiplet contains states $J^{PC} = 2^{-+}, 1^{--}, 2^{--}, 3^{--}$ and so on. A good example of a constituent quark model is the Godfrey-Isgur model [11] and its indubitable success in explaining the experimental spectrum of mesons when it was first conceived in 1985 is summarised in the abstract by the authors: "We show that mesons – from the π to the Υ – can be described in a unified quark model with chromodynamics."

Despite the success of the quark model in 1985, are these effective models sufficiently able to describe the entire meson spectrum as we know it today? Whilst the quark model explains the features of many of the experimental states, there is a plethora of experimentally observed mesons that do not agree with the quark model picture. A meson with properties that does not fit the pattern of constituent quark models is deemed to be *exotic*. A clear example of an exotic meson is a state with $J^{PC} = 0^{--}, 0^{+-}, 1^{-+}, \ldots$ that has *exotic* J^{PC} *quantum numbers* not accessible by a quark-antiquark pair and if such a state is confirmed experimentally, it would be undeniably exotic. There is evidence of such a meson with $J^{PC} = 1^{-+}$ in the light sector [12, 13] which demands an explanation beyond quark models. Whilst there are other examples of exoticness in the light sector and the issue is interesting in its own right, I will focus this thesis on charm mesons which contain at least one charm quark. The charm sector is a particularly attractive area because in general, the experimental signals for these states are cleaner and they are described better by effective models due to being reasonably non-relativistic from the heaviness of the charm quark.

In the hidden-charm sector, the charmonium ($c\bar{c}$) spectrum is rife with exotic mesons as shown in Figure 1.1. The green lines show the observed states that are identified with conventional quark model states and the black lines show the mass of the predicted Godfrey-Isgur state that has not yet been identified experimentally [14]. The red and purple lines show the majority of observed charmonium whose properties do not align

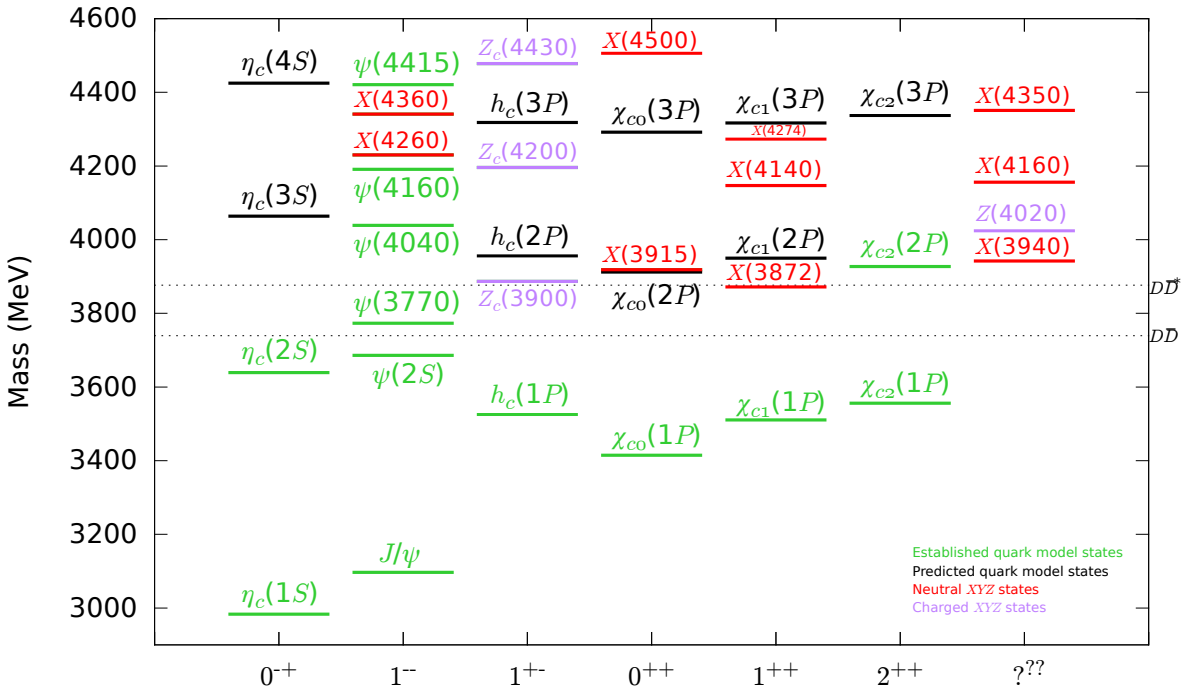

Figure 1.1: The charmonium spectrum shown by the solid lines labelled by J^{PC}. Black lines give the predicted mass of the conventional $c\bar{c}$ state in the Godfrey-Isgur model that has not yet been observed [14]. Green lines show the states observed experimentally and identified with conventional $c\bar{c}$ states. Red lines give some of the observed XYZ states that are considered exotic and purple lines show the charged Z states [15]. The dotted lines represent the $D\bar{D}$ and $D\bar{D}^*$ kinematic thresholds.

with the patterns predicted by quark models, known as the XYZ *states*, listed by the Particle Data Group [15], and many of them are still not fully understood. Whilst the charmonium states below kinematic threshold are well studied and interpreted to be quark model states, it is above threshold when the spectrum becomes particularly intriguing. Taking the most historic example, $X(3872)$ [16] was the first experimental state to be considered as an exotic charmonium. It has sparked interest due to its significantly large isospin-violating decay to $J/\psi\pi\pi$ that makes it difficult to identify as a conventional $c\bar{c}$ state which must have isospin-0. Other examples of exoticness in this sector are the charged Z states which cannot be pure $c\bar{c}$ states due to their non-

zero electric charge. Another striking example of exoticness is in the vector channel where all the quark model states below 4500 MeV have been identified and therefore, any additional states within that region must have some origin beyond the quark model. Most recently, the exotics, $X(4500)$ and $X(4700)$, were discovered by LHCb in 2017 [17]. Currently, there is no experimental charmonium state with exotic J^{PC} quantum numbers since this quantum number is difficult to access experimentally but QCD suggests they exist as shown later in this work and there is promising experimental work to probe this channel in times to come. Looking towards the future, there is excitement surrounding upcoming studies to further understand the properties of the XYZ states and possible new discoveries are expected to be made with current experiments such as Belle II, BES III, LHCb and the planned experiment PANDA.

In addition to the hidden-charm sector, the open-charm sector immediately shows prominent examples of exoticness in the low-lying spectrum. Quark model predictions in the charm-strange sector expect a scalar and axial vector above the respective DK and D^*K threshold [11] but the experimental states $D_{s0}^*(2317)$ and $D_{s1}(2460)$ are found to lie below threshold [15]. This is puzzling when comparing to the corresponding charm-light sector where the experimental states $D_0^*(2400)$ and $D_1(2420)$ are found to be in agreement with quark model predictions above the analogous $D\pi$ and $D^*\pi$ threshold, and decay as broad resonances. It is even more peculiar how light the experimental charm-strange states are compared to their charm-light counterparts and there is clearly a contradiction in identifying $D_{s0}^*(2317)$ as a conventional $c\bar{s}$ state since this state should be heavier than the $c\bar{l}$ state, $D_0^*(2400)$, given that the strange quark is heavier than the light quarks. Due to difficulties in assigning $D_{s0}^*(2317)$ and $D_{s1}(2460)$ as conventional quark model states, they have been considered exotic in this sense.

The previous discussions demonstrate that there is an abundance of exotic mesons in the charm sector that require a description beyond the quark model picture. Numerous models have been constructed in an attempt to explain the exotic mesons and I will give a brief summary but this list is in no means exhaustive; see Refs. [18, 19] and

further references in this paragraph for a more comprehensive review. If QCD can give rise to constituent quarks, it seems reasonable to consider QCD also giving rise to constituent gluons. A meson consisting entirely of constituent gluons is known as a glueball [20] whilst one consisting of gluons and quarks is known as a hybrid meson [21]. Another way to extend the quark model of mesons is to increase the number of quarks and antiquarks from two to four and the four quarks could possibly arrange themselves as a spatially compact tetraquark bound by gluons or an extended molecule of two conventional mesons [22, 23, 24]. Alternatively, some of these exotic mesons may not be dynamical objects but arise due to kinematical effects from the opening of thresholds that produces an enhancement in the cross section [25].

I have given a brief taste of some of the models used to attempt to describe the experimental exotic states but nevertheless, there is no unanimous agreement within the phenomological community on the correct intepretation of the majority of these exotics. Whilst these models are useful for our understanding of the exotics, the underlying properties of every meson should be described and encompassed by the fundamental theory of the strong interactions, QCD. Necessarily, a complete understanding of mesons from first principles can only be made within the confines of QCD. Additionally, it would be interesting to study how QCD could realise these phenomological models. Ultimately, the validity of a phenomological model is made by testing its predictions with the outcomes of QCD and experiment. As a strongly coupled field theory at hadronic energies, performing QCD calculations is a challenging and daunting task. A non-perturbative method, known as *lattice QCD*, originating from Wilson [26] is to regulate the theory using a discretised and finite spacetime with the quark fields living on the lattice sites and the gauge fields linking the sites together. This formulation provides a means to study QCD that is ab-initio and systematically improvable, unlike those from effective models. The lattice spacing introduces an ultraviolet cutoff rendering the theory well defined such that physical observables can be computed numerically using Monte Carlo techniques. Hadron spectroscopy calculations in lattice QCD have progressed to

the point where determinations of masses of hadrons, stable under the strong interaction, have entered the precision era [27, 28, 29, 30, 31, 32, 33] with calculations having full control over all systematic uncertainties at the few percent level [34] and a state-of-the-art calculation measuring the mass difference of the neutron-proton [35].

Besides obtaining the masses of hadrons, spectroscopy is also concerned with the unstable properties of hadrons above thresholds that decay through the strong interaction. It is important to be able to measure these observables since the majority of the mesons we have observed are resonances that are not stable under the strong interaction and exotic mesons are generally found above or in close proximity to thresholds. Experimentalists observe resonances through cross sections of scattering hadrons and the theoretical quantities that describe them are the scattering amplitudes. Resonances and bound states are rigorously identified as poles in the scattering amplitudes which are analytically continued into the complex plane. Computing the scattering amplitudes within lattice QCD is a novel field as these quantities are notoriously difficult to calculate within lattice field theory for reasons which will be discussed later. A general formalism, known as the *Lüscher method* [36, 37, 38, 39], to determine two-body scattering amplitudes from the finite-volume spectrum of lattice QCD has been developed and extensions to include three or more particles are underway [40, 41, 42, 43]. The last decade has seen a huge number of such scattering amplitude calculations using the Lüscher method by many different groups but there have only been a handful of studies in the charm sector [44, 45, 46, 47, 48], necessitating further studies. Besides strong decays, it is also possible to determine the electroweak transitions of mesons and the hadronic transition matrix elements can be calculated non-perturbatively in lattice QCD, for example in Refs. [49, 50]. Obtaining the transition rates from a first principles calculation is extremely important for understanding exotic mesons in terms of phenomology, whilst comparing with experiment, as the corresponding predictions within separate models are usually very different.

In an attempt to further understand exotic mesons from a first principles approach,

this thesis is concerned with spectroscopy of exotic charm mesons using lattice QCD. It should be emphasised that the goal is to carry out exploratory computations and demonstrate novel techniques as proof of principle with less emphasis on precision calculations, which are computationally demanding but desirable for future studies. To give an outline of the thesis, the next chapter gives an introduction to lattice QCD and the framework to calculate the finite-volume spectrum of lattice QCD. Chapter 3 contains a demonstration of the framework and presents a calculation of charmonium spectra across a large range of quantum numbers and energies. In the spectra, states that are consistent with quark model patterns are found but in addition, a number of states are identified to belong in the lightest and first excited hybrid meson supermultiplet. To pave the way for scattering amplitude calculations, Chapter 4 introduces the necessary technology to study four-quark states that could arrange themselves as compact tetraquarks or extended meson-mesons. Finite-volume spectra, in channels with flavour quantum numbers not accessible by quark model states, are calculated in the isospin-1 hidden charm sector and doubly charmed sector, and it is concluded that there are no indications for compact tetraquark states in the spectra. In addition, the spectra did not qualitatively show the signs of a narrow resonance which could be identified with the charged Z states. Chapter 5 discusses the problems with calculating scattering amplitudes in lattice QCD and reviews the Lüscher method to overcome these complications. An explicit application of this method, in combination with the computational framework developed in this thesis, is used to calculate isospin-0 DK scattering amplitudes which are relevant for the exotic $D_{s0}^*(2317)$ state. The amplitudes are found to contain a shallow bound state near threshold which is consistent with the experimental findings. A brief summary and outlook is given in Chapter 6.

Chapter 2

Lattice QCD

Due to the strongly coupled nature of QCD at hadronic energies, a non-perturbative method is required to perform calculations which can be provided by lattice QCD. In this chapter, I will introduce and review the important aspects of the framework required to calculate physical observables, i.e. the finite-volume spectrum of lattice QCD. For more details on lattice QCD, see Refs. [51, 52, 53].

2.1 Continuum QCD

The action for continuum QCD in Euclidean space is given by

$$S = S_{\text{fermion}}[q, \bar{q}, A] + S_{\text{gauge}}[A]. \tag{2.1}$$

The reasons for working in Euclidean space by Wick rotating the time coordinate will be clear later. In the fermion sector,

$$S_{\text{fermion}}[q, \bar{q}, A] = \int d^4x \ \sum_f \bar{q}_f(x)(\gamma^\mu D_\mu[A] + m_f)q_f(x) \tag{2.2}$$

where f labels the flavour of the quark field, q, and D_μ is the gauge-covariant derivative. The gauge action is described by

$$S_{\text{gauge}}[A] = \int d^4x \ \frac{1}{4} F_{\mu\nu}F^{\mu\nu}. \tag{2.3}$$

In the path integral formulation, the continuum partition function is given by

$$Z = \int \mathcal{D}[q, \bar{q}] \ \mathcal{D}[A] \ e^{-S_{\text{fermion}}[q,\bar{q},A] - S_{\text{gauge}}[A]}. \tag{2.4}$$

From a mathematical perspective, the path integral is infinite-dimensional and is not rigorously well-defined. Nevertheless, this formulation has been employed with great success in calculating the observables of a quantum theory. For theories with a small coupling, perturbation theory can be used to calculate quantities to some order of the coupling. Unfortunately, perturbation theory cannot be applied to QCD at the hadronic scale due to its strong coupling and therefore, whatever method used must necessarily be non-perturbative. Regulating QCD on a discrete lattice is one possibility such that the path integral is finite-dimensional and can be computed numerically.

2.2 Discretisation of gauge fields

To begin the discretisation of QCD, consider a four-dimensional spacetime lattice

$$\Lambda \equiv \{x = (x_1, x_2, x_3, x_4) : x_i = (0, 1, \ldots, N-1) \cdot a\} \tag{2.5}$$

with N points in each direction separated by lattice spacing, a, such that the volume of the lattice is $L^4 = (aN)^4$ and periodic or anti-periodic boundary conditions are chosen at the boundary. The fields take values only at the lattice points and the continuous derivative and integral are replaced by discretised versions

$$\partial_\mu q(x) \to \frac{1}{2a}\left[q(x + a\hat{\mu}) - q(x - a\hat{\mu})\right], \qquad \int d^4x \to a^4 \sum_{x \in \Lambda}. \tag{2.6}$$

To discretise the gauge action, it is more convenient to consider the link variables

$$U_\mu(x) = \exp\left[iagA_\mu(x)\right] \tag{2.7}$$

in terms of the gauge field A_μ. This link variable has the property of a parallel transporter such that under a gauge transformation, $q(x) \to G(x)q(x)$,

$$U_\mu(x) \to U'_\mu(x) = G(x)U_\mu(x)G(x + a\hat{\mu})^\dagger \tag{2.8}$$

which is not gauge invariant but this shows that gauge invariant quantities can be constructed from the trace of closed loops of link variables. The link variable can also

be defined in the other direction as $U_{-\mu}(x) = U_\mu(x - a\hat{\mu})^\dagger$. The simplest closed loop that can be constructed is the *plaquette*,

$$U_{\mu\nu}(x) = U_\mu(x)U_\nu(x + a\hat{\mu})U_\mu^\dagger(x + a\hat{\nu})U_\nu^\dagger(x) \tag{2.9}$$

and a discretised action for gauge fields in terms of these plaquettes is given by

$$S_{\text{gauge}}[U] = \frac{2}{g^2}\sum_{x\in\Lambda}\sum_{\mu<\nu}\Omega_{U_{\mu\nu}}(x) \tag{2.10}$$

where $\Omega_{U_{\mu\nu}} = \text{Re}[\text{tr}(\mathbb{1} - U_{\mu\nu})]$. This gauge action can be expanded using Equation (2.7) giving

$$S_{\text{gauge}} = \frac{a^4}{4}\sum_{x\in\Lambda}\sum_{\mu,\nu}F_{\mu\nu}^2(x) + \mathcal{O}(a^2) \tag{2.11}$$

which shows that the correct continuum limit is recovered when $a \to 0$. However, since numerical calculations cannot be performed at this limit, results for physical observables will always be contaminated by lattice artefacts. It will be shown later how to modify this discretised action to reduce unwanted discretisation effects arising from the $\mathcal{O}(a^2)$ corrections such that the simulations for a given lattice spacing have a better resemblance to its desired continuum limit.

2.3 Discretisation of fermions

Having discretised the gluons, I discuss the discretisation of the quark action. The link variables are used to construct a discretised version of the symmetrised gauge-covariant derivative operator

$$\nabla_\mu q(x) = \frac{1}{2a}\left[U_\mu(x)q(x + a\hat{\mu}) - U_{-\mu}(x)q(x - a\hat{\mu})\right]. \tag{2.12}$$

A discretised version of the fermion action is given by

$$S_{\text{fermion}}[q, \bar{q}, U] = a^4\sum_{x\in\Lambda}\sum_f \bar{q}_f(x)\ D^f\ q_f(x) \tag{2.13}$$

where the discretised Dirac operator, D^f, is given by $D^f = m_f + \gamma^\mu\nabla_\mu$. Note that this operator acts on colour space but the colour indices have been suppressed for brevity.

This naive discretisation of fermions suffers from a highly non-trivial problem known as fermion doubling. To illustrate this problem, consider the propagator in momentum space in the absence of gauge fields,

$$\left[D^f\right]^{-1}(p) = \frac{-i\gamma_\mu \sin(ap_\mu)/a + m_f}{\sum_\mu \sin^2(ap_\mu)/a^2 + m_f^2}. \tag{2.14}$$

This propagator has the correct continuum limit and in the massless case, it contains a pole at $p = (0, 0, 0, 0)$. However, there are additional unphysical poles whenever the momentum components are $p_\mu = \pi/a$. One possible solution to remove these unwanted poles is to add an irrelevant term, referred to as the *Wilson term*, to the action such that the mass of the doublers is $\mathcal{O}(\pi/a)$ and they decouple from the theory in the continuum limit. The Dirac operator with the Wilson term is given by

$$D_W^f = m_f + \gamma^\mu W_\mu \tag{2.15}$$

where $W_\mu = \nabla_\mu - \frac{a}{2}\gamma_\mu \Delta_\mu$,[1] and

$$\Delta_\mu q(n) = \frac{1}{a^2}\left[U_\mu(n)q(n+\hat{\mu}) + U_{-\mu}(n)q(n-\hat{\mu}) - 2q(n)\right] \tag{2.16}$$

is the discretised version of the symmetrised second-order gauge covariant derivative. This Wilson fermion action also has the correct continuum limit and has leading order discretisation effects at $\mathcal{O}(a)$ from the addition of the Wilson term. In a similar manner to the gauge fields, it is desirable to minimise contamination from lattice artefacts. The details on reducing leading order discretisation effects will be given in the next section. Whilst there are other strategies to remove the fermion doublers, I will not discuss them here as I will use the Wilson prescription in this work due its relatively low computational cost compared to other methods.

2.4 Anisotropic and improved actions

Before discussing the reduction of discretisation effects in the lattice action, I will need to introduce the *anisotropic lattice*, where the temporal lattice spacing, a_t, is smaller

[1] There is no sum over indices here

than the spatial lattice spacing, a_s, on a lattice of size $(L/a_s)^3 \times (T/a_t)$. Ideally, both lattice spacings should be as small as possible but it will be shown later that spectrum is extracted from exponential functions in time, e^{-Et}. Therefore, it is more desirable to reduce the temporal lattice spacing, at a reasonable cost, than the spatial lattice spacing to obtain better resolution in calculating the energies of excited states. To implement an anisotropic lattice, the temporal and spatial components of the terms in the action are separated out and weighted differently with an anisotropy parameter. This does introduce a new parameter into the theory that requires tuning to reproduce the desired ratio between the temporal and spatial lattice spacings. The lattices used in this work will be anisotropic and with this topic covered, I will now discuss the discretised QCD action used in this work that has reduced leading order discretisation effects.

In a practical application, one would use the lattice QCD action given above that has the correct continuum limit and compute observables that will contain systematic errors arising from discretisation effects. In principle, the discretisation effects can be accounted for by calculating quantities at various lattice spacings and extrapolating to the continuum but this procedure comes with a large computational cost having to perform calculations for multiple lattices. As the main focus of this work is on exploratory calculations, to understand the physics from a qualitative point of view, and to demonstrate the feasibility of some of the techniques, I will use a single lattice spacing but it would be interesting for future work to study the dependence on the lattice spacing. One would want to maximise the efficiency of the calculation, at a given lattice spacing, by minimising the systematic effects arising from lattice artefacts. One approach, known as *Symanzik improvement*, provides an efficient method to reduce discretisation effects for a lattice with fixed lattice spacing. In this approach, the discretisation effects are systematically removed by directly adding irrelevant terms of higher dimensions to the action. This does not add new parameters to the theory since the coefficients of the terms in the improved action are determined by demanding that the terms reproduce the correct continuum action to some given accuracy.

Before giving the improved action, it is necessary to discuss *tadpole improvement* to remove large divergences arising from tadpoles. These tadpoles arise from the expansion of the link variables,

$$U_\mu(x) = 1 + iagA_\mu(x) - \frac{a^2g^2}{2}A_\mu^2(x) + \dots. \tag{2.17}$$

When this quantity is contracted, one naively expects the quadratic term to be suppressed by a^2 but the contraction of the gauge fields cancels this factor so it is proportional to g^2 which can become large. These tadpole divergences arise from the UV and can be removed from the link variables by tadpole-improvement where the link variables are divided out by the mean field value u_0 of the link variable [54]. This improvement relies on the assumption that the gauge fields can be split into infrared and ultraviolet parts and the ultraviolet part can integrated out,

$$U_\mu = e^{iagA_\mu} = e^{iag(A_\mu^{\mathrm{IR}}+A_\mu^{\mathrm{UV}})} = u_0\tilde{U}_\mu \tag{2.18}$$

such that the divergences arising from tadpole contributions can be removed. A common choice for u_0 is to take the fourth root of the expectation value of the plaquette.

With all of this in mind, I will give explicitly the lattice QCD action used throughout this thesis. For the gauge action, there are no five-dimensional irrelevant terms due to gauge invariance so the gauge action is automatically $\mathcal{O}(a)$ improved. The on-shell $\mathcal{O}(a^2)$ improvement was done by Lüscher and Weisz and they found, at tree-level, that the rectangular six-link loop is the only six-dimensional operator needed to improve the gauge action. The Symanzik improved gauge action described by the anisotropic Lüscher-Weisz action [55, 56] with tree-level tadpole-improved coefficients is given by

$$S_{\mathrm{gauge}} = \frac{2}{\gamma_g g^2}\left(\sum_{x,s\neq s'}\left[\frac{5}{6u_s^4}\Omega_{U_{ss'}} - \frac{1}{12u_s^6}\Omega_{R_{ss'}}\right] + \sum_{x,s}\gamma_g^2\left[\frac{4}{3u_s^2u_t^2}\Omega_{U_{st}} - \frac{1}{12u_s^4u_t^2}\Omega_{R_{st}}\right]\right) \tag{2.19}$$

where u_s and u_t are the spatial and temporal tadpole factors, $R_{\mu\nu}$ is the 2×1 rectangular Wilson loop, s and s' run over spatial indices, and the parameter γ_g is the bare gauge anisotropy. This gauge action has leading discretisation error at $\mathcal{O}(a_s^4, a_t^2, g^2a_s^2)$.

For the fermion action, it can be shown using the equations of motion that only one five-dimensional operator is needed to improve the action at leading order. The on-shell $\mathcal{O}(a)$ improvement of the Wilson fermion action is described by the anisotropic Sheikholeslami-Wohlert fermion action [57, 58],

$$S_{\text{fermion}} = \sum_x \bar{\hat{q}}_f(x) D_C^f \hat{q}_f(x) \tag{2.20}$$

where

$$D_C^f = \frac{1}{\tilde{u}_t}\left\{\tilde{u}_t \hat{m}_f + \gamma_t \hat{W}_t + \frac{1}{\gamma_f}\gamma_s \hat{W}_s - \frac{1}{2}\left[c_t \sigma_{ts}\hat{F}_{ts} + \frac{c_s}{\gamma_g}\sigma_{ss'}\hat{F}_{ss'}\right]\right\}. \tag{2.21}$$

Hats denote dimensionless variables: quark fields $\hat{q}_f = a_s^{3/2} q_f$, bare quark masses $\hat{m}_f = a_t m_f$, dimensionless Wilson operator $\hat{W}_\mu = \nabla_\mu - \frac{1}{2}\gamma_\mu \Delta_\mu$,[2] and gauge field strength $\hat{F}_{\mu\nu} = a_\mu a_\nu F_{\mu\nu}$. $F_{\mu\nu}$ is represented by Wilson lines that resemble a four-leaf clover and is given explicitly in Ref. [57]. Whilst it is possible to calculate the Clover coefficients non-perturbatively [59], this is quite a daunting task so an estimate is made by setting them to the classical tadpole-improved values [58]

$$c_t = \frac{1}{2}\left(\frac{\gamma_g}{\gamma_f} + \frac{1}{\xi_R}\right)\frac{1}{\tilde{u}_t \tilde{u}_s^2}, \qquad c_s = \frac{\gamma_g}{\gamma_f}\frac{1}{\tilde{u}_s^3}. \tag{2.22}$$

The link variables in the fermion action are chosen to be three-dimensionally stout smeared [60] to reduce mixing with high frequency modes so that $\tilde{u}_s$ and $\tilde{u}_t$ are used to denote the corresponding spatial and temporal tadpole factors for smeared gauge links. $\gamma_{t,s}$ are Dirac gamma matrices. γ_f is the bare fermion anisotropy and $\xi_R = a_s/a_t$ is the desired renormalised anisotropy. I will utilise the ensembles generated by the Hadron Spectrum Collaboration (HadSpec) where $\beta = 6/g^2 = 1.5$ and the tuning of the coefficients/parameters can be found in Refs [61, 62] that gives the explicit values. Further details of the lattices that I use will be given in Section 2.9. As mentioned earlier, an anisotropic lattice introduces extra bare anisotropy parameters that require tuning to obtain the desired anisotropy. The renormalised gauge anisotropy is obtained

[2]There is no sum over indices here.

from the static quark potential by measuring ratios of Wilson loops in the temporal direction and spatial direction. The renormalised fermion anisotropy is determined from the continuum relativistic dispersion relation $E^2 = m^2 + \vec{p}^2/\xi_f^2$. It is important to say that once the parameters here have been set, the theory is completely predictive.

2.5 Numerical calculation of observables in lattice QCD

With QCD discretised appropriately, the theory can be quantised using the path integral formulation and the partition function is given by

$$Z = \int \prod_{x\in\Lambda} \prod_{f} dq_f(x)\ d\bar{q}_f(x)\ \prod_{\mu} dU_\mu(x)\ e^{-S_{\text{fermion}}[q,\bar{q},U]-S_{\text{gauge}}[U]} \tag{2.23}$$

where the colour and spin components have been suppressed. The most important detail is that this integral is finite-dimensional and well-defined compared to the continuum case. Computing this integral by hand is practically impossible due to the enormous number of degrees of freedom, even for a modestly sized lattice, and therefore, the solution is to turn to numerical integration. Due to the large number of dimensions, a suitable approach is to use Monte Carlo methods by sampling over a finite number of configurations and the accuracy is improved with larger sample sizes. This method crucially relies on the Wick rotation to Euclidean space as the exponentials in this integral behave as a Boltzmann weight which exponentially suppresses field configurations far away from the classical solution. In contrast, if this integral was in Minkowski space, the exponentials would contain an imaginary factor and oscillate so wildly that the Monte Carlo method would not work.

To be able to numerically integrate the partition function, the quark fields can be integrated out to give

$$Z = \int \prod_{x\in\Lambda} \prod_{\mu} dU_\mu(x)\ e^{-S_{\text{gauge}}[U]} \prod_{f} \det(D_C^f[U]). \tag{2.24}$$

It was a common practice to employ the *quenched* approximation where the determinants are set to one to reduce computation time but modern calculations are now able to include the fermionic determinant. The calculations in this work will use unquenched light and strange quarks and quenched charm quarks. The up and down quarks are degenerate so that isospin is a good symmetry as isospin breaking effects are expected to be negligible and mostly unimportant for this work unless mentioned explicitly. The quenching of the charm quark introduces a systematic uncertainty but it is expected that the effects are fairly small due to the heaviness of the charm quark and it is empirically found to be the case in calculations such as Ref. [33, 63].

This partition function allows for the calculation of correlation functions

$$\langle \mathcal{O} \rangle = \frac{1}{Z} \int \prod_{x \in \Lambda} \prod_{\mu} dU_\mu(x)\ e^{-S_{\text{gauge}}[U]} \prod_f \det(D_C^f[U])\ \mathcal{O}[(D_C^f)^{-1}[U], U] \tag{2.25}$$

for some operator $\mathcal{O}$. Using Monte Carlo integration, this quantity can be estimated numerically and is given by an average over N configurations,

$$\langle \mathcal{O} \rangle \approx \frac{1}{N} \sum_{n=1}^{N} \mathcal{O}\left[(D_C^f)_n^{-1}[U_n], U_n\right] \tag{2.26}$$

where for the n'th configuration, the gauge configurations, U_n, are importance sampled from the distribution

$$e^{-S_{\text{gauge}}[U]} \prod_f \det(D_C^f[U]) \tag{2.27}$$

and $(D_C^f)^{-1}$ is the quark propagator. The gauge configurations that I use have been generated by HadSpec with rational hybrid Monte Carlo algorithms described in Refs. [61, 62] where the configurations are evolved by numerically integrating the equations of motion of a pseudo-Hamiltonian. The generation of propagators will be described later.

As the configurations are generated from a Markov chain process that relies on the previous configurations, they are statistically correlated and this requires consideration to reliably obtain an estimate of the statistical uncertainty. One rudimentary prescription to handle this is to use bootstrap techniques to create subsets of configurations from the original sample. In particular, I will calculate the statistical uncertainty using

jackknife resampling where an observable $\hat{O}$ is calculated from a sample of N configurations and the quantity $\hat{O}_n$ is calculated for N data sets with $N-1$ configurations by removing the n'th configuration of the original set with $n = 1, \ldots, N$. The estimator of the statistical uncertainty is given by

$$\sigma_{\hat{O}} = \sqrt{\frac{N-1}{N} \sum_{n=1}^{N} \left(\hat{O}_n - \hat{O}\right)^2}. \tag{2.28}$$

One of the major advantages of lattice QCD compared to other methods is its systematic improvability. The statistical uncertainty can be decreased by sampling over a larger set of configurations and in principle, all systematic uncertainties can be controlled and reduced at the cost of computational expenditure.

2.6 Extracting finite-volume spectrum

Having discussed how to numerically compute correlation functions, I will describe how to extract the finite-volume spectrum of lattice QCD from them. To obtain the spectrum, I will calculate two-point correlation functions for some interpolating operator, $\mathcal{O}^\dagger(t)$. The correlators can be re-expressed by inserting a complete set of eigenstates, $|\mathfrak{n}\rangle$, of the QCD Hamiltonian,

$$C(t) \equiv \langle \mathcal{O}(t)\mathcal{O}^\dagger(0)\rangle = \sum_{\mathfrak{n}} \frac{1}{2E_{\mathfrak{n}}} |\langle 0|\mathcal{O}|\mathfrak{n}\rangle|^2 e^{-E_{\mathfrak{n}}t}. \tag{2.29}$$

It is important to point out that this sum over the eigenstates is completely discrete due to the finite-volume. Writing in Euclidean energy space,

$$\tilde{C}(E) = \int dt\ e^{iEt} C(t) = \sum_{\mathfrak{n}} |\langle 0|\mathcal{O}|\mathfrak{n}\rangle|^2 \frac{1}{E_{\mathfrak{n}}^2 + E^2} \tag{2.30}$$

assuming that the lattice used has a large temporal extent such that e^{-ET} corrections are exponentially suppressed. Therefore, $E_{\mathfrak{n}}$ give the location of the poles that appear in the finite-volume two-point correlation functions in Minkowski space. It is sufficient to extract the spectrum, $E_{\mathfrak{n}}$, from the exponential fall-off of the correlation functions

in time to obtain the spectrum without having to analytically continue the correlation functions in Euclidean space to Minkowski space. The matrix elements $\langle 0|\mathcal{O}|\mathfrak{n}\rangle$ are also interesting quantities to extract but they will require renormalisation to obtain their physical values. The situation becomes more complicated for unstable resonances, that decay into multi-particle final states with a continuous range of energy above threshold, and resonances can be identified as poles in the complex plane. Since the correlation functions in lattice QCD can only be numerically calculated at discrete points in energy with finite precision, analytically continuing to Minkowski space is practically impossible. The Lüscher method that overcome this obstacle will be discussed in later chapters but nevertheless, this method will require knowledge of the finite-volume spectrum to determine the scattering amplitudes in infinite volume.

To extract the spectrum from the two-point correlation functions, it is straightforward to obtain the ground state energy by taking the large time limit,

$$E_0 = \lim_{t \gg 1} \ln \left[C(t)/C(t+1) \right], \tag{2.31}$$

such that the excited states are exponentially suppressed and only the ground state dominates. To further extract the energies of excited states, it is advantageous to have large temporal resolution in the exponentials and this is the main reason for utilising an anisotropic lattice with a finer lattice spacing in the temporal direction. In principle, it is possible to fit multiple exponentials to the correlation functions in order to obtain the excited state energies. In practice, this is often difficult given that excited energy levels may be nearly degenerate, the statistical precision is limited and there is no clear criteria on how many exponentials to include. A more sophisticated method to reliably extract the spectrum makes use of a variational method [64, 65, 66] where a matrix of two-point correlation functions $C_{ij}(t) = \langle \mathcal{O}_i(t)\mathcal{O}_j(0)^\dagger \rangle$ is calculated for a basis of operators $\{\mathcal{O}_i\}$. The correlation matrix can be expressed as a spectral decomposition

$$C_{ij}(t) = \sum_{\mathfrak{n}} \frac{1}{2E_{\mathfrak{n}}} Z_i^{\mathfrak{n}*} Z_j^{\mathfrak{n}} e^{-E_{\mathfrak{n}} t} \tag{2.32}$$

where $Z_i^{\mathfrak{n}} = \langle \mathfrak{n}|\mathcal{O}_i^\dagger|0\rangle$ are the operator-state matrix elements referred to as *overlaps*. A

generalised eigenvalue equation for the correlation matrix is solved,

$$C(t)v^{\mathfrak{n}}(t) = \lambda_{\mathfrak{n}}(t)C(t_0)v^{\mathfrak{n}}(t) \tag{2.33}$$

where t_0 is some choice in time, $\lambda_{\mathfrak{n}}$ are the eigenvalues referred to as *principal correlators* related to the energy by $\lambda_{\mathfrak{n}}(t) \sim e^{-E_{\mathfrak{n}}(t-t_0)}$, and $v^{\mathfrak{n}}$ are the eigenvectors related to the overlaps by $Z_i^{\mathfrak{n}} = \sqrt{2E_{\mathfrak{n}}}e^{E_{\mathfrak{n}}t_0/2}v_j^{\mathfrak{n}*}C_{ji}(t_0)$. The eigenvectors are also useful later for constructing an *optimised operator*, $\Omega_{\mathfrak{n}}^{\dagger} \sim \sum_i v_i^{\mathfrak{n}}\mathcal{O}_i^{\dagger}$, which is the optimal linear combination of operators that interpolates state $\mathfrak{n}$ [67]. Using the implementation described in Refs. [68, 69], the energy levels are extracted from the principal correlators by fitting them to the function

$$\lambda^{\mathfrak{n}}(t) = (1 - A_{\mathfrak{n}})e^{-E_{\mathfrak{n}}(t-t_0)} + A_{\mathfrak{n}}e^{-E'_{\mathfrak{n}}(t-t_0)} \tag{2.34}$$

where the fit parameters are $E_{\mathfrak{n}}$, $E'_{\mathfrak{n}}$ and $A_{\mathfrak{n}}$. The second exponential is used to account for possible contamination in the principal correlator due to excited states. The choice of t_0 needs to be high enough to reduce excited state contamination but low enough such that the signal-to-noise ratio is adequate. This choice can introduce a systematic error in how one chooses to fit the spectrum but the error is generally found to be negligible for low-lying spectrum. An example of a systematic test of varying t_0 can be found in Ref. [69] where it was found that spectrum was reasonably stable under changes in t_0 partly due to the use of the second exponential that absorbs effects from other unwanted states.

As the two-point correlation functions contain the entire finite-volume spectrum of QCD, it should be possible to completely extract the energy levels from them but in practice, the ability to extract spectrum can depend on the operator basis used. If the basis is not sufficiently diverse such that the overlap for a state onto all the operators is small, it can be difficult to reliably extract the energy of that state due to limited statistical precision. Therefore, it is desirable to construct a basis of operators with substantial overlap onto the lowest-lying states to ensure a robust and correct extraction of the spectrum. A general construction of operators with structures resembling single-mesons, meson-mesons and tetraquarks will be given later in the next chapters. One

method to increase the overlap onto lower-lying states is to smear the quark fields that appear in operators and this will be described in Section 2.8. The smearing method used here offers a framework to compute propagators and calculate correlation functions in an efficient manner. Another method is to construct operators that transform in irreducible representations of the symmetries of the lattice ensuring that only states with the same quantum numbers as the operators will have non-zero overlap.

2.7 Symmetries of the lattice

From Equation (2.29), the two-point correlation function contains a summation over all possible energy eigenstates of the theory and this sum can be drastically truncated by constructing operators that transform definitely under the symmetries of the theory. If a theory is invariant under a symmetry, then the symmetry commutes with the Hamiltonian and a basis of simultaneous eigenstates of the symmetry and energy can be chosen. By constructing the interpolating operators to transform irreducibly under the symmetries, only the eigenstates with the same quantum numbers as the operators will have non-zero operator-state overlap.

In the continuum and infinite volume, the operators can be projected to definite momentum and constructed to transform irreducibly in angular momentum representation J (row m) of the rotational group. At rest, the rows of the representation are labelled by the z-component of spin, $m = J_z$, but this is generally not a good quantum number for non-zero momentum. For states at non-zero momentum, the rotational group is broken to the group of rotations that leaves the momentum invariant and the rows, $m = \lambda$, are labelled by the helicity λ which is the angular momentum projected along the direction of momentum. A detailed construction of a basis of helicity states with appropriate conventions can be found in Ref. [70]. To be completely clear, I use the letter m as a general symbol to denote the rows of the continuum irrep which is given by J_z when at rest and the helicity λ when at non-zero momentum.

On the cubic lattice, the rotational group is broken such that angular momentum

J	Λ
0	A_1
1	T_1
2	$E \oplus T_2$
3	$A_2 \oplus T_1 \oplus T_2$
4	$A_1 \oplus E \oplus T_1 \oplus T_2$

Table 2.1: Subduction of continuum spin J into lattice irreps Λ of O for $J \leq 4$ [71].

is not a good quantum number. The remnant symmetry group on the cubic lattice is the octahedral group, O_h, at rest. At non-zero momentum $\vec{P}$, the symmetry is reduced further to the little group, $\mathrm{LG}(\vec{P})$, that leaves the momentum invariant and a noticeable distinction between the continuum is that the little group depends on $\vec{P}$. Operators can be projected to definite momentum by $\mathcal{O}(\vec{P},t) = \sum_{\vec{x}} e^{i\vec{P}\cdot\vec{x}}\mathcal{O}(\vec{x},t)$. In a finite-volume, the momentum is quantised due to the periodic boundary conditions, $\vec{P} = \frac{2\pi}{L}\vec{n}$ where $\vec{n} = (n_x, n_y, n_z)$ is a triplet of integers. I will use the shorthand notation where the intergers $[n_x n_y n_z]$ are understood to denote $\vec{P}$.

Operators are constructed to transform irreducibly under the symmetries of the lattice by first constructing continuum operators transforming in J (row m) and then distributing the rows into the irreducible representations Λ (row μ) of the relevant lattice symmetry group. This distribution will be referred to as *subduction* and the subduction coefficients, $S^{J,m}_{\Lambda,\mu}$, are defined by

$$S^{J,m}_{\Lambda,\mu} = \langle J, m | \Lambda, \mu \rangle \tag{2.35}$$

that subduces a continuum state $|J,m\rangle$ into lattice state $|\Lambda,\mu\rangle$ by $|\Lambda,\mu\rangle = \sum_m S^{J,m}_{\Lambda,\mu}|J,m\rangle$. The subduction of J into Λ at rest is given in Table 2.1 [71]. It can be seen in the table that the problems with the breaking of rotational symmetry by the lattice become apparent with angular momentum not being conserved. For example, how does one identify the spin of a state in the $\Lambda = T_1$ irrep which can have $J = 1, 3, \ldots$? This

issue will be addressed in the next chapter. To obtain the subduction coefficients at rest, it can be seen that the trivial representation $J = 0$ subduces purely into the trivial representation $\Lambda = A_1$ of O and therefore, the subduction coefficients are trivially given by $S^{0,0}_{A_1,1} = 1$. Furthermore, the fundamental representation, $J = 1$, subduces purely into $\Lambda = T_1$ so that $m = 1, 0, -1$ is in one-to-one correspondence with $\mu = 1, 2, 3$ and it is straightforward to take $S^{1,m}_{T_1,\mu} = \delta_{\mu,2-m}$. From this, the simplest way to calculate subduction coefficients for zero momentum is iteratively, using the formula from the definition of the subduction coefficients,

$$\begin{aligned} S^{J,m}_{\Lambda,\mu} =& N \sum_{\mu_1,\mu_2} \sum_{m_1,m_2} \langle J, m | J_1, m_1; J_2, m_2 \rangle \langle J_1, m_1; J_2, m_2 | \Lambda_1, \lambda_1; \Lambda_2, \lambda_2 \rangle \langle \Lambda_1, \lambda_1; \Lambda_2, \lambda_2 | \Lambda, \mu \rangle \\ =& N \sum_{\mu_1,\mu_2} \sum_{m_1,m_2} \langle J, m | J_1, m_1; J_2, m_2 \rangle S^{J_1,m_1}_{\Lambda_1,\mu_1} S^{J_2,m_2}_{\Lambda_2,\mu_2} \langle \Lambda_1, \lambda_1; \Lambda_2, \lambda_2 | \Lambda, \mu \rangle \end{aligned} \tag{2.36}$$

where N is a normalisation factor that ensures the subduction coefficients are orthonormal, $\sum_m S^{J,m}_{\Lambda,\mu} S^{J,m*}_{\Lambda',\mu'} = \delta_{\Lambda,\Lambda'}\delta_{\mu,\mu'}$. $\langle \Lambda_1, \lambda_1; \Lambda_2, \lambda_2 | \Lambda, \mu \rangle$ are octahedral group Clebsch-Gordan coefficients for $\Lambda_1 \otimes \Lambda_2 \to \Lambda$ [72] and $\langle J, m | J_1, m_1; J_2, m_2 \rangle$ are $SO(3)$ Clebsch-Gordan coefficients for $J_1 \otimes J_2 \to J$. I use the octahedral group subduction coefficients given in Ref. [69].

For non-zero momentum, the subduction differs from the rest case as the group is broken down to the little group such that J_z and parity are no longer good quantum numbers. Following the conventions of Ref. [70], a helicity state where the spin component is measured along the direction of momentum (helicity λ) is given by

$$|\vec{P}; J, \lambda\rangle = R L_z(P) |J, \lambda\rangle = \sum_{J_z} \mathcal{D}^{J}_{J_z\lambda}(R) L(\vec{P}) |J, J_z\rangle \tag{2.37}$$

where $\mathcal{D}^{J}_{J_z\lambda}(R)$ are Wigner-D matrices, R is a rotation that rotates the z-axis to the direction of $\vec{P}$, $L_z(P)$ is the Lorentz boost along the z-axis with magnitude P and $L(\vec{P}) = R L_z(P) R^{-1}$ is the Lorentz boost in the direction of $\vec{P}$ with magnitude P. This helicity state has the property that rotations leave the helicity invariant, $\tilde{R}|\vec{P}; J, \lambda\rangle = |\tilde{R}\vec{P}; J, \lambda\rangle$. The distribution of the continuum irrep into the lattice irreps is governed by the helicity and can be found by the action of the relevant little group on the helicity

	Λ		
λ	$\mathrm{Dic}_4([n00])$	$\mathrm{Dic}_2([nn0])$	$\mathrm{Dic}_3([nnn])$
0^+	A_1	A_1	A_1
0^-	A_2	A_2	A_2
1	E_2	$B_1 \oplus B_2$	E_2
2	$B_1 \oplus B_2$	$A_1 \oplus A_2$	E_2
3	E_2	$B_1 \oplus B_2$	$A_1 \oplus A_2$

Table 2.2: Subduction of helicity λ into lattice irreps Λ for various $LG(\vec{P})$ with $\lambda \leq 3$ [73]. $\vec{P}$ is given in units of $\frac{2\pi}{L}$ and n is an integer. The symmetry associated with a reflection in the plane containing the momentum direction is preserved for $\lambda = 0$ and the superscript denotes the eigenvalue of this symmetry. This is given by $P(-1)^J$ where P is the parity of the state at rest.

state. This distribution into the irreps of the little group up to $\vec{P} = [nnn]$ is given in Table 2.2 [73]. The problem mentioned earlier with angular momentum no longer being conserved is even more severe here as the mixing of angular momentum is more pronounced. For example, the irrep $\Lambda = E_2$ for $\vec{P} = [n00]$ contains all states with $J \geq 1$ making it substantially harder to identify the continuum spin. The subduction coefficients that I will use can be found in Ref. [70]. In summary, with the subduction coefficients obtained, an operator that originally transforms in continuum irrep J is subduced to transform in lattice irrep by $\mathcal{O}^{\Lambda,\mu}(\vec{P},t) = \sum_m S^{J,m}_{\Lambda,\mu}\mathcal{O}^{J,m}(\vec{P},t)$.

In addition to these symmetries, there are also the standard discrete symmetries. For states at rest, there is parity P but this is generally not a good quantum number for non-zero momentum. Depending on the flavour of the quarks in the interpolating operator, there may also be charge-conjugation symmetry C. In the case that the up and down quarks are degenerate, there is a generalisation when isospin is a good symmetry known as G-parity and can be defined as $\hat{G} = \hat{C}e^{i\pi I_2}$ i.e. a rotation by π around the second

axis of isospin space followed by charge-conjugation. In general, the G-parity is given by $G = C(-1)^I$ where I is the isospin.

2.8 Calculation of correlation functions using distillation

Another method to improve the extraction of spectrum, besides the use of symmetry, is to smear the quark fields in the interpolating operators as mentioned previously. The correlation functions will be calculated within the *distillation* framework [74] which firstly provides a smearing of the quark fields to increase overlap onto lower-lying states and more importantly, allows for an efficient means to calculate correlation functions through a convenient factorisation. To motivate the distillation framework, I will discuss the difficulties in computing correlation functions by considering, as an example, the two-point correlation function for an operator resembling a single-meson projected to zero momentum, $\mathcal{O}(t) = \sum_{\vec{x}} \bar{q}(\vec{x}, t)\Gamma q(\vec{x}, t)$,

$$\begin{aligned}\langle \mathcal{O}(t)\mathcal{O}^\dagger(0)\rangle = \sum_{\vec{x},\vec{y}} \Big[&- \operatorname{tr}\left(D_C^{-1}(\vec{x}, t; \vec{y}, 0)\Gamma D_C^{-1}(\vec{y}, 0; \vec{x}, t)\Gamma\right) \\ &+ \operatorname{tr}\left(D_C^{-1}(\vec{x}, t; \vec{x}, t)\Gamma\right) \operatorname{tr}\left(D_C^{-1}(\vec{y}, 0; \vec{y}, 0)\Gamma\right) \Big] \end{aligned} \tag{2.38}$$

where the quark fields have been evaluated under the path integral. It can be seen that the numerical evaluation of the two-point correlation function requires the propagator which can be calculated by inverting the Dirac operator for each gauge configuration. The second term, known as a *disconnected* contribution, is highly problematic in computation as it requires knowledge of the propagator on the entire spacetime lattice. Computationally storing and manipulating these propagators is not practically feasible due to their huge size.

One method to circumvent this problem is to smear the quark fields using distillation [74]. The distillation operator on timeslice t acting in 3-space ($\vec{x}$ and $\vec{y}$) and colour

space (a and b) is defined as

$$\Box(\vec{x},a;\vec{y},b;t) = \sum_{n=1}^{N_{\text{vecs}}} \xi_n(\vec{x},a;t)\xi_n^\dagger(\vec{y},b;t) \tag{2.39}$$

where ξ_n are the lowest N_{vecs} eigenvectors of the gauge-covariant Laplacian, ∇^2. The quark fields are smeared by the distillation operator, $q \to \Box q$, in the interpolating operators to reduce overlap onto high-frequency modes. For the rest of this thesis, any mention of quark fields is implied to be smeared with the distillation operator. This operator is a truncated eigenvector representation of a smearing function, $\exp(\sigma\nabla^2(t))$, where σ is the smearing width as the exponential suppresses all the modes of the Laplacian except for those with the lowest eigenvalues.

The same two-point correlation function in terms of this smeared quark field is

$$\langle \mathcal{O}(t)\mathcal{O}^\dagger(0)\rangle = -\operatorname{tr}\left[\tau(t,0)\Phi(t)\tau(0,t)\Phi(0)\right] + \operatorname{tr}\left[\tau(t,t)\Phi(t)\right]\operatorname{tr}\left[\tau(0,0)\Phi(0)\right] \tag{2.40}$$

where the *perambulators*,

$$\tau_{nm}(t,0) = \sum_{\vec{x},a;\vec{y},b} \xi_n^\dagger(\vec{x},a;t)D_C^{-1}(\vec{x},a;t;\vec{y},b;0)\xi_m(\vec{y},b;0), \tag{2.41}$$

and the *elementals*,

$$\Phi_{nm}(t) = \sum_{\vec{x},a;\vec{y},b} \xi_n^\dagger(\vec{x},a;t)\Gamma_{\vec{x},a;\vec{y},b}(t)\xi_m(\vec{y},b;t), \tag{2.42}$$

are square matrices of dimension $(4N_{\text{vecs}})^2$ in *distillation space* and the Dirac indices have been suppressed. N_{vecs} can be suitably chosen such that distillation space is far smaller compared to the full colour-coordinate space of the propagators. This means that perambulators and elementals can be generated and stored on disk in an efficient manner to remedy the problem described above involving disconnected contributions. The cost of performing the contraction of perambulators and elementals is far smaller than the contraction in the full colour-coordinate space. This framework offers a convenient way of factorising the correlation functions to solely describe the propagation of quarks by the perambulators, and the momentum and spin structure of the operators is entirely

encoded in the elementals. The elementals will be extended later to generally describe operators with various structures projected onto definite momentum.

In addition, the computational cost of calculating propagators in this framework is drastically reduced since perambulators belong to a smaller distillation space. The perambulators can be obtained by numerically inverting the Clover operator on the sources ξ_m, i.e. a numerical solver is used to find $y = D_C^{-1}\xi_m$ and this quantity is then left-multiplied by $\xi_n^\dagger$. The software codes `Chroma` [1], `QUDA` [2, 3], `QPhiX` [4], and `QOPQDP` [5, 6] were used to compute the propagators required for this project. The lattices that the perambulators were computed on will be discussed in the next section.

2.9 Lattice details

This work was performed using the improved action on anisotropic lattices of size $(L/a_s)^3 \times (T/a_t)$ where a_t is smaller than the spatial lattice spacing, $a_s \approx 0.12$ fm, with an anisotropy $\xi = 3.5$. The details of each lattice are summarised in Table 2.3 with the main differences being the size $(L/a_s)^3 \times (T/a_t)$ and the corresponding pion mass M_π; future references to these lattices will make use of these labels. There are $N_f = 2+1$ flavours of dynamical quarks where the two degenerate light quarks are tuned to give a corresponding pion mass, $M_\pi = 236$ MeV for the 32^3 lattice [75], and $M_\pi = 391$ MeV for the 16^3 and 24^3 lattices [61, 62]. The remaining quark is tuned to approximate the physical strange quark. The charm quark is described by the same relativistic action but is quenched and tuned to reproduce the physical η_c mass [76, 77]. The systematic effect from quenching the charm quark was discussed in Section 2.5 and expected to be small. Discretisation effects from the charm quark action will be described later.

To give results in physical units, the scale is set using the mass of the Ω baryon measured from lattice calculations and the experimental value [78] via $a_t^{-1} = M_\Omega^{\text{phys}}/(a_t M_\Omega)$. On the $M_\pi = 391$ MeV ensemble, $a_t M_\Omega^{\text{latt.}} = 0.2951(22)$ [79] giving $a_t^{-1} = \frac{M_\Omega^{\text{exp.}}}{a_t M_\Omega^{\text{latt.}}} = 5667$. For the $M_\pi = 236$ MeV ensemble, $a_t M_\Omega = 0.2789(16)$ [75] leading to $a_t^{-1} = 5997$ MeV. The uncertainty arising from the ambiguity in scale setting can be estimated by using

Lattice Size	M_π (MeV)	N_{cfgs}	N_{tsrcs}	N_{vecs}
$16^3 \times 128$	391	478	1	64
$24^3 \times 128$	391	553	32	162
$32^3 \times 256$	236	484	1	384

Table 2.3: The lattice gauge field ensembles used. The size is given as $(L/a_s)^3 \times (T/a_t)$ where L and T are respectively the spatial and temporal extents of the lattice. The number of gauge field configurations used, N_{cfgs}, and number of perambulator time-sources used per configuration, N_{tsrcs}, is shown along with the number of eigenvectors used in the distillation framework, N_{vecs}.

other observables to set the scale. For example, for the $M_\pi = 236$ MeV ensemble, setting the scale using the $h_c - \eta_c$ mass splitting gives $a_t^{-1} = 5960$ MeV which is 0.6% lower than from using the Ω baryon. Another example would be to use the $\eta_c(2S) - \eta_c(1S)$ mass splitting which gives $a_t^{-1} = 5787$ MeV, 4% lower than the first value.

Another source of uncertainty comes from the unphysically heavy light quark mass. As the bare mass parameter of the light quark is decreased, the fermion matrix becomes increasingly singular and difficult to numerically invert. This is one reason why lattice QCD calculations are typically performed using unphysically heavy quarks and this work is no exception. Although advances in algorithms and computing power have allowed for calculations at physical point to be possible, rigorous scattering amplitude calculations in lattice QCD are limited by the Lüscher formalism which can only describe two-body thresholds at the moment. A large pion mass gives a larger energy region to compute spectrum before encountering three-or-more-body thresholds. Whilst calculating at heavier light quark masses may seem like a disadvantage at first, these computations provide a window to explore how the physics differs as the light quark mass parameter is varied. This is particularly important for validating models, as for example, it may be easy to tune the parameters of an effective molecular or tetraquark model to reproduce

the experimental results but varying the quark masses in these different models could lead to drastically different physics which can be compared with lattice QCD calculations. It is also interesting for scattering calculations to study how thresholds move and how the stability of resonances changes as the pion mass is varied. These points will be discussed in more detail in the chapter on scattering.

Related to this are finite-volume corrections for stable particles which scale with the pion mass as $e^{-M_\pi L}$ [37] so lattice QCD calculations typically require large volumes. The lattices here will have at least $M_\pi L \gtrsim 3.5$ such that finite-volume corrections are expected to be negligible for all of the work in this thesis. In addition, $M_\pi T$ is large such that $e^{-M_\pi T}$ temporal corrections are also expected to be small.

Chapter 3

Excited and Exotic Charmonium

Using the techniques in the previous chapter, I describe the calculation of charmonium spectra, across a wide range of channels and energies, for the 32^3 lattice with $M_\pi = 236$ MeV described in Section 2.9. This sector is where the exotic XYZ mesons are found and it would be interesting to compare the computed spectra with the experimental results. To obtain spectra, two-point correlation function matrices are computed for operators resembling charmonium including those with a hybrid meson structure and spectra are extracted from them using the variational method. As mentioned previously, angular momentum is no longer a good quantum number on the lattice so I will describe the method used to identify the continuum spin of a state. The extracted spectra are interpreted phenomologically using expectations of quark models and hybrid meson models. This work was published in Ref. [77].

In addition, I will compare the results I have with previous HadSpec results [76] obtained with the same framework on the 24^3 lattice with $M_\pi = 391$ MeV. That work was noteable for the identification of the lightest and first-excited hybrid meson supermultiplet, due to the technology allowing for a reliable identification of spin and an extraction of spectra across many channels and different energies. The work here will gauge the systematic effects arising from the unphysical light quarks by studying how the spectra behave at these two different light quark masses.

The charm quark is described by the same relativistic action as the other quarks except it is quenched when generating gauge configurations. This does introduce a systematic effect but as discussed in Section 2.5, it is expected to be fairly small. The lattice spacings are fine enough, giving $a_t m_c \ll 1$ and $a_s m_c < 1$, such that the action is suitable to describe the charm quark and discretisation effects should be relatively

small. To assess the quality of tuning of the parameters of the charm quark action on the 32^3 lattice, Figure 3.1 shows a successful fit, $\chi^2/N_{\text{d.o.f}} = 1.08$, of the momentum dependence of the η_c energy to the relativistic dispersion relation

$$(a_t E)^2 = (a_t M)^2 + \left(\frac{2\pi}{\xi L/a_s}\right)^2 n^2 \tag{3.1}$$

giving $\xi_{\eta_c} = 3.456(4)$ which is consistent with the anisotropy for the light mesons measured using the pion dispersion relation, $\xi_\pi = 3.453(6)$ [75]. In addition, the fit gives the mass of the η_c to be 2945(17) MeV compared to the experimental value 2983.6(6) MeV [78] and so the systematic uncertainty arising from the tuning of the charm quark mass is of the percent level. To reduce the systematic uncertainty from tuning the charm quark, the final results will show the energy levels in the spectra with the mass M_{η_c} subtracted. The figure also shows the momentum dependence of the D meson energy which gives $\xi_D = 3.443(7)$, in reasonable agreement with the previous values. Further fits, to a dispersion relation with a higher order term $(a_s P)^4$ and a lattice dispersion relation $\cosh(a_t E) = \cosh(a_t M) + 2\sin^2(a_s P_\mu/2)$, were found to be consistent with the relativistic dispersion relation and had larger $\chi^2/N_{\text{d.o.f.}}$ suggesting that discretisation effects are small. Overall, the agreement of the energy levels with the relativistic dispersion relation suggests that the discretisation effects from the charm quark action are manageable, at least up to these values of momentum. A similar conclusion was made in Ref. [76] for the 24^3 lattice which also gave a rough estimate of the uncertainty arising from discretisation effects. To estimate this, the authors note that the Clover coefficients in the $\mathcal{O}(a)$-improved action are set to the tree-level tadpole-improved values but their values are expected to be larger if determined non-perturbatively [59]. A rough estimate of the uncertainty was found to be approximately 40 MeV [76] by manually increasing the Clover coefficients in an ad hoc manner.

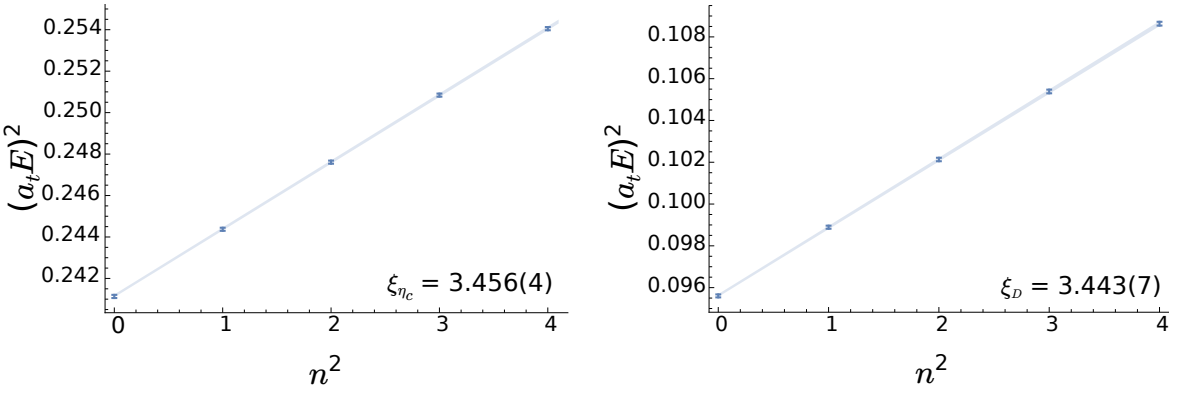

Figure 3.1: The dependence of the η_c (left panel) and D (right panel) energy on momentum shown by the points; error bars show the one sigma statistical uncertainty on either side of the mean. Lines are fits to the relativistic dispersion relation in Equation (3.1), giving $\xi_{\eta_c} = 3.456(4)$ ($\chi^2/N_{\text{d.o.f}} = 1.08$) and $\xi_D = 3.443(7)$ ($\chi^2/N_{\text{d.o.f}} = 0.38$).

3.1 Single-meson operators

In order to calculate two-point correlation functions and extract spectra for charmonium, the simplest interpolating operators that can be constructed are colour-singlet fermion bilinears of the form $\sum_{\vec{x}} e^{i\vec{P}\cdot\vec{x}}\bar{q}(\vec{x},t)\Gamma q(\vec{x},t)$ where Γ is a Dirac gamma matrix. For general purposes later, the quarks in these operators could be of different flavours but here, I will take them to be charm quarks so the operators have a structure that resembles charmonium. In this case, charge conjugation C is a good quantum number and for the work here, I will take $\vec{P} = 0$ such that parity, P, is a good quantum number. As a reminder, the quark fields are smeared with the distillation operator to improve overlap onto low-lying states. The naming convention here for Γ is given in Table 3.1 along with the corresponding J^{PC} of the operator with this Γ. The set of operators constructed in this way is limited as only a small number of J^{PC} can be accessed. To access higher spins and exotic J^{PC} quantum numbers forbidden by quark-antiquark pairs, the fermion bilinears can be extended by including a number of gauge-covariant

derivatives, $\overleftrightarrow{D} \equiv \overleftarrow{D} - \overrightarrow{D}$, following the methods in Ref. [69], as

$$\mathcal{O}^{J,m}(\vec{P},t) = \sum_{\vec{x}} e^{i\vec{P}\cdot\vec{x}} \bar{q}(\vec{x},t)(\Gamma \overleftrightarrow{D} \overleftrightarrow{D} \dots)^{J,m} q(\vec{x},t) \tag{3.2}$$

where $(\Gamma \overleftrightarrow{D} \overleftrightarrow{D} \dots)^{J,m}$ denotes that Γ and the gauge-covariant derivatives are coupled using $SO(3)$ Clebsch-Gordan coefficients to transform in continuum irrep J, m. This class of operators will be referred to as *single-meson operators* as they have structure resembling single-mesons. The gamma matrices and gauge-covariant derivatives are chosen to be in a circular basis such that they transform like spin-1 and couple in a straightforward manner. I will use the notation $(\Gamma \times D^{[N]}_{J_D})^J$ to denote a single-meson operator with gamma matrix Γ and N derivatives coupled to spin J_D, overall coupled to spin J. For a single derivative, coupling a gamma matrix and one derivative to either $J = 0, 1, 2$ is given by

$$(\Gamma \times D^{[1]}_{J_D=1})^{J,m} \sim \sum_{m_1,m_2} \langle J_1, m_1; 1, m_2 | J, m \rangle \Gamma_{m_1} \overleftrightarrow{D}_{m_2}. \tag{3.3}$$

It is straightforward to include more gauge-covariant derivatives but then there is some freedom in how to couple the spins together. The convention for coupling up to three derivatives will follow the one given in Ref. [69] to ensure that charge-conjugation symmetry is preserved. For two derivatives, the derivatives are coupled together first and then coupled to the gamma matrix as

$$(\Gamma \times D^{[2]}_{J_D})^{J,m} \sim \sum \langle J_3, m_3; J_D, m_D | J, m \rangle \langle 1, m_1; 1, m_2 | J_D, m_D \rangle \Gamma_{m_3} \overleftrightarrow{D}_{m_1} \overleftrightarrow{D}_{m_2} \tag{3.4}$$

and for three derivatives, the spins of the outermost derivatives are coupled together first followed by the middle derivative and then the gamma matrix as

$$\begin{aligned}(\Gamma \times D^{[3]}_{J_{13},J_D})^{J,m} \sim \sum & \langle J_4, m_4; J_D, m_D | J, m \rangle \langle 1, m_2; J_{13}, m_{13} | J_D, m_D \rangle \\ & \langle 1, m_1; 1, m_3 | J_{13}, m_{13} \rangle \Gamma_{m_4} \overleftrightarrow{D}_{m_1} \overleftrightarrow{D}_{m_2} \overleftrightarrow{D}_{m_3}.\end{aligned} \tag{3.5}$$

This procedure can be generalised to include as many derivatives as desired but for this work, the single-meson operators are constructed with up to three derivatives giving

	1	γ_5	$\gamma_0\gamma_5$	γ_0	γ_i	$\gamma_i\gamma_0$	$\gamma_5\gamma_i$	$[\gamma_i, \gamma_j]$
Γ	a_0	π	π_2	b_0	ρ	ρ_2	a_1	b_1
J^{PC}	0^{++}	0^{-+}	0^{-+}	0^{++}	1^{--}	1^{--}	1^{++}	1^{+-}

Table 3.1: The naming convention for the Dirac gamma matrices and their corresponding J^{PC} within a fermion bilinear.

access to spins up to $J = 4$. To obtain an operator that transforms in lattice irrep Λ, the operators are subduced by $\mathcal{O}^{\Lambda[J],\mu}(\vec{P}, t) = \sum_m S^{J,m}_{\Lambda,\mu} \mathcal{O}^{J,m}(\vec{P}, t)$. To repeat, the spectra will be calculated here at rest so $\vec{P} = 0$.

It is worthwhile to note that some operator constructions give access to exotic J^{PC} numbers that are forbidden by quark models. There are also some single-meson operators where two or more derivatives appear and couple to give the commutator of two derivatives, $[\overleftrightarrow{D}, \overleftrightarrow{D}]$, which is the gluonic field-strength tensor by definition for a non-abelian gauge theory. In other words, there are some operators proportional to $\bar{q}F_{\mu\nu}q$ and these operators have a structure resembling hybrid mesons – quark-antiquark pairs coupled to a gluonic excitation. The importance of these hybrid meson operators will become apparent once the final spin-identified spectrum is shown and I will give further comments on them later.

To calculate correlation functions involving single-meson operators in the distillation framework, the single-meson elemental is given by

$$\Phi^{\alpha\beta}_{nm}(\vec{P}, t) = \Gamma^{\alpha\beta} \sum_{\vec{x},a;\vec{y},b} \xi^{\dagger}_n(\vec{x}, a; t) e^{i\vec{P}\cdot\vec{x}} [\overleftrightarrow{D} \ldots]_{\vec{x},a;\vec{y},b}(t) \xi_m(\vec{y}, b; t) \tag{3.6}$$

where α, β label the Dirac spin indices. When computing the correlation functions, disconnected contributions due to annihilation between the charm and anticharm quark are neglected as they are expected to be small due to OZI suppression and this is found to be the case empirically in lattice calculations [80]. An effect from excluding annihilation effects is that this forbids charmonium from mixing with the light isoscalar states. This is a significant advantage as if this was not the case, the different mass scales of the light

Λ	Λ^{-+}	Λ^{--}	Λ^{++}	Λ^{+-}
A_1	12	6	13	5
A_2	4	6	5	5
T_1	18	26	22	22
T_2	18	18	22	14
E	14	12	17	9

Table 3.2: The number of single-meson operators, including up to three-derivatives, used to calculate the two-point correlation function matrix in each lattice irrep, Λ^{PC}.

and charm quarks would make extracting charmonium states amongst the light states practically infeasible.

3.2 Identifying the spin of a state

The number of single-meson operators (at rest and up to three derivatives) for each channel, Λ^{PC}, is shown in Table 3.2. Having calculated the two-point correlation function matrices, I obtain charmonium spectra using the variational method and show the extracted energy levels labelled by lattice irrep Λ^{PC} in lattice units in Figure 3.2. Each box in the figure gives the extracted energy level with the vertical size of the box representing the one-sigma statistical uncertainty on either side of the mean. The boxes are colour coded by their identified continuum spin using the spin identification method described in this section. Figure 3.3 shows a sample selection of extracted principal correlators from correlation functions in the T_1^{--} irrep and the leading time dependence, $e^{-M_{\mathfrak{n}}(t-t_0)}$, has been divided out to exhibit a plateau when a single exponential dominates. Each fit of the principal correlators to Equation (2.34) was successful with $\chi^2/N_{\text{d.o.f}} \sim 1$.

To connect the results with physical states, it is necessary to identify the continuum spin of these states. One rudimentary way to identify the lowest-lying $J = 0$ and 1 states

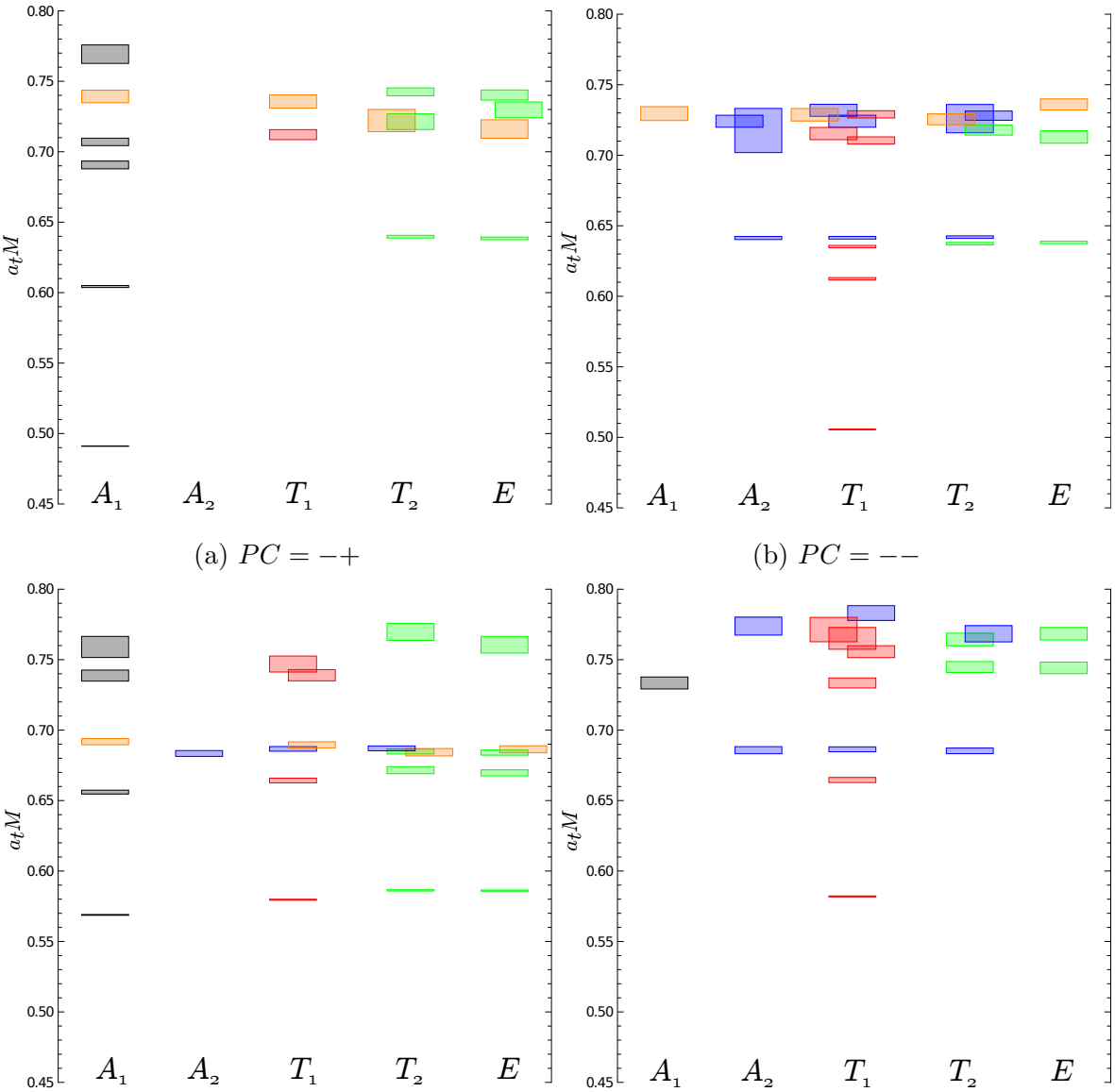

(a) $PC = -+$ (b) $PC = --$

(c) $PC = ++$ (d) $PC = +-$

Figure 3.2: Finite-volume spectrum of charmonium at rest in lattice units labelled by lattice irrep Λ^{PC}. Each box gives the extracted energy level with the vertical extent of the box representing the one-sigma statistical uncertainty on either side of the mean. The colour coding gives the spin of the state identified by the method described in the text: $J = 0$ (black), 1 (red), 2 (green), 3 (blue), 4 (orange).

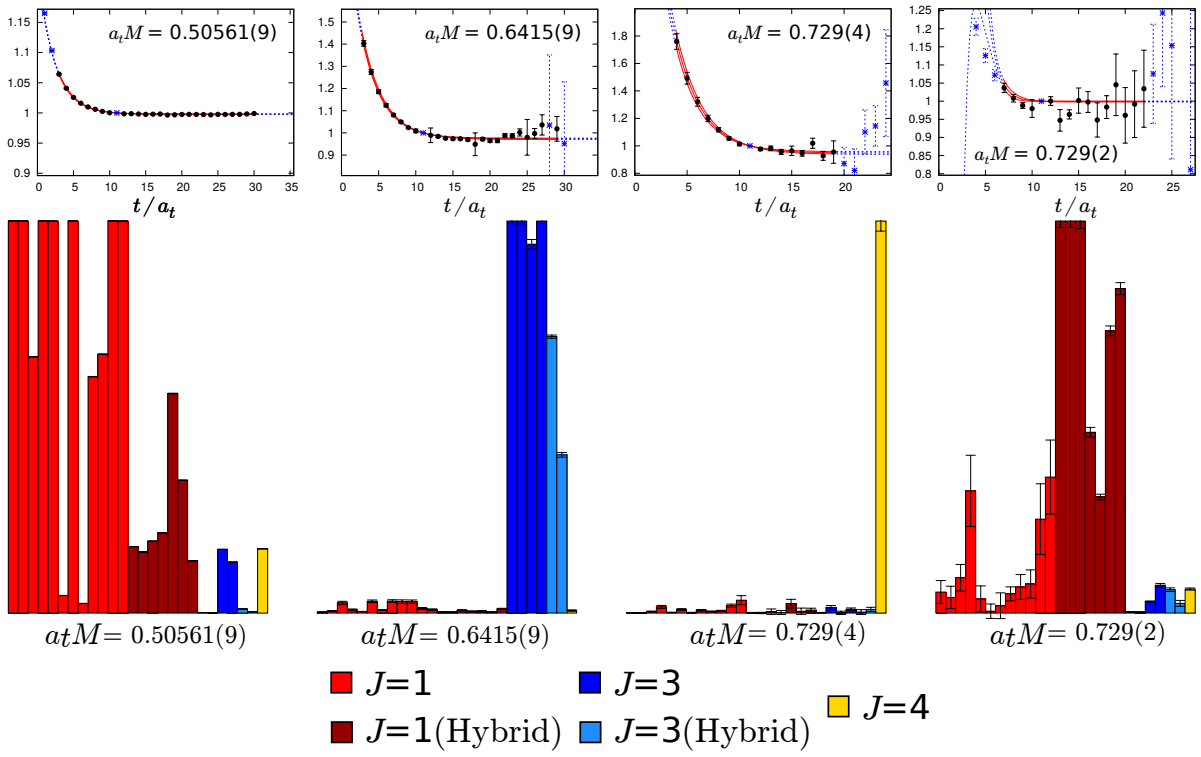

Figure 3.3: Top row shows the principal correlators for a selection of low-lying states in the T_1^{--} irrep. The data (points) and fits (curves) for $t_0 = 11$ are plotted as $\lambda^{\mathfrak{n}} e^{M_{\mathfrak{n}}}(t - t_0)$ showing the central values and one sigma statistical uncertainties. The corresponding operator-state overlaps, $Z_i^{\mathfrak{n}}$, for each operator are shown below. The overlaps are normalised so that the largest value for an operator across all states is equal to unity. The legend gives the colour coding for the continuum spin J of the operator before subduction and the operators labelled hybrid are proportional to the gluonic field-strength tensor.

would be to notice that they subduce purely into $\Lambda = A_1$ and T_1 respectively. With this in mind, one could identify the lowest-lying states in $\Lambda^{PC} = A_1^{-+}$ and T_1^{--} to be pseudoscalar and vector states respectively. However, this method cannot be generally applied for excited states, especially the regions near $a_tM \approx 0.75$, where a huge number of states is found across irreps. For example, there is no way to identify the excited states using only the energies in T_1^{--} which could possibly be $J = 1, 3, 4, \ldots$. Since

there are a finite number of lattice irreps compared to the infinite number of continuum spins, it is not possible to identify the spin of a given state in a one-to-one procedure without any extra information. In principle, one could determine the spin by repeating the calculation in every irrep for various lattice spacings, and find degeneracies across irreps appear according to the expected pattern of subductions as the lattice spacing is reduced. However, this method becomes costly having to simulate at finer lattice spacings and with limited statistical precision, it is practically impossible to disentangle degeneracies across lattice irreps amongst a densely populated spectrum.

To solve this problem, I will use the spin-identification method using the operator-state overlaps described in Ref. [69] that does not necessarily require calculations at multiple lattice spacings. This technique relies on the subduced single-meson operator, $\mathcal{O}^{\Lambda[J],\mu}$, that was originally constructed with continuum spin to carry a 'memory' of the spin. One expects that for a large volume and small lattice spacing where rotational symmetry is restored to a reasonable extent, states with continuum spin J would only overlap strongly onto smeared operators subduced from the same J and be suppressed for operators subduced from other J [81]. As an example, Figure 3.3 shows the operator-state overlaps of every operator for a selection of states in $\Lambda^{PC} = T_1^{--}$. The overlap values are normalised so that the maximum value for an operator across all states is equal to one. The operators were originally subduced from continuum spin J: red bars correspond to $J = 1$, blue to $J = 3$ and yellow to $J = 4$. It can clearly be seen that every state has a dominant overlap only onto operators with common J and the first and fourth state can be identified to be $J = 1$, the second state is $J = 3$ and the third state is $J = 4$.

However, this procedure only identifies the spin of a state within its lattice irrep but does not tell us anything more about how the states across lattice irreps are related. A single continuum state with spin J has its spin components subduced amongst multiple lattice irreps and the next problem is to figure out whether or not the extracted states across lattice irreps correspond to the same continuum state. It is shown in Ref. [69]

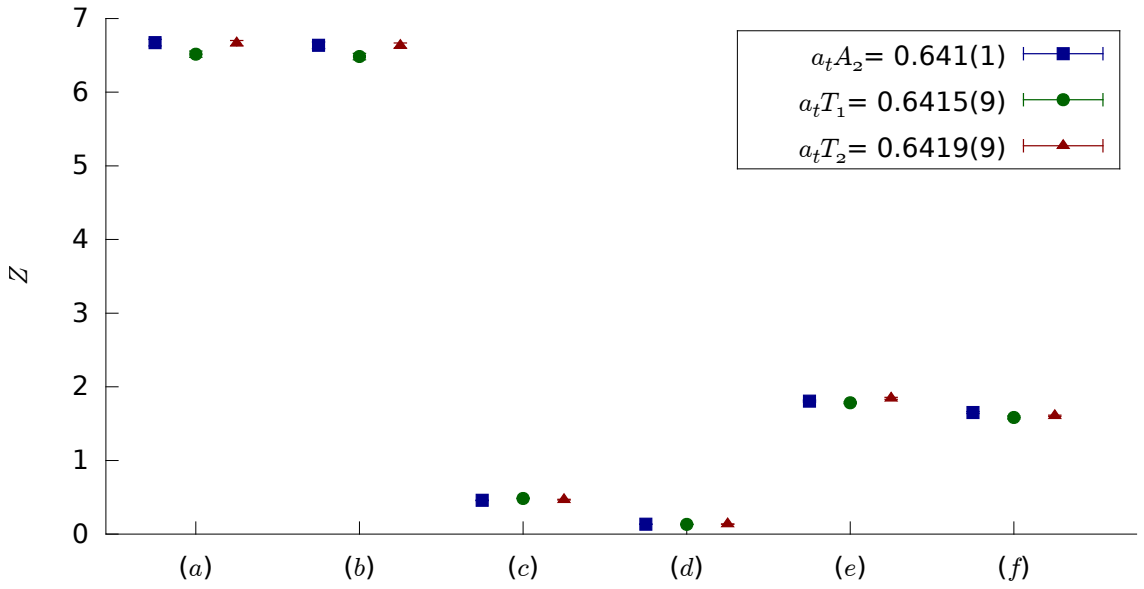

Figure 3.4: Overlaps, Z, for states in the irreps labelled by the legend that are suspected of being the same continuum $J = 3$ state. The error bars are smaller than the points shown. The operators are as follows: (a) $(\rho \times D^{[2]}_{J_D=2})^{J=3}$, (b) $(\rho_2 \times D^{[2]}_{J_D=2})^{J=3}$, (c) $(b_1 \times D^{[3]}_{J_{13}=1,J_D=2})^{J=3}$, (d) $(a_1 \times D^{[3]}_{J_{13}=2,J_D=2})^{J=3}$, (e) $(a_1 \times D^{[3]}_{J_{13}=2,J_D=3})^{J=3}$, (f) $(a_0 \times D^{[3]}_{J_{13}=2,J_D=3})^{J=3}$.

that the overlaps of a state onto a given operator of spin J are independent of the lattice irrep it is subduced to, up to discretisation effects. Therefore, a continuum state can be identified by comparing all the operator overlaps amongst each lattice irrep. For example, a $J = 3$ state will have the same operator-state overlap value in each of the A_2, T_1, T_2 irreps. To illustrate, Figure 3.4 shows some overlaps for states in the A_2, T_1, T_2 irreps that are believed to be the same continuum $J = 3$ state. It can be seen that the operator-state overlaps for each $J = 3$ operator are practically identical amongst the irreps and therefore, I conclude that these lattice states correspond to the same continuum state. This example is representative of all the other states in the spectrum and the identification of spin was done this way. After repeating this

procedure for each lattice state and identifying the continuum states, there is ambiguity in choosing how to quote the final energy of a state. The energies corresponding to the same continuum state may differ between irreps due to discretisation effects and other systematic uncertainties from the fitting procedure. The simplest way would be to extract energies from the principal correlators in each irrep and quote the average value. Instead, to minimise the fluctuations caused by the fitting, a simultaneous fit to Equation (2.34) of all the principal correlators in each irrep will be taken with a common fit parameter $E_{\mathfrak{n}}$ and irrep-specific parameters $\{E'^{\Lambda}_{\mathfrak{n}}\}, \{A^{\Lambda}_{\mathfrak{n}}\}$.

3.3 Spin-identified spectrum

The charmonium spectra in physical units after spin identification are shown in Figure 3.5 where each box gives the energy level and the vertical size of the box represents the one-sigma statistical uncertainty on either side of the mean. The masses are quoted with the η_c mass subtracted to reduce the systematic uncertainty arising from tuning of the charm quark mass parameter. Dashed lines indicate the location of some relevant thresholds for strong decay given that the charm quark does not annihilate. A wide range of excited states across a large number of channels up to $J = 4$ were extracted demonstrating the formidability of the computational techniques described up to now. There have been a variety of charmonium spectrum calculations in lattice QCD such as Ref. [30, 82, 83]. In these studies, a robust extraction of states across a large span of channels and energies is difficult and the identification of continuum spin is an obstacle since none of these studies use as extensive an operator basis like the one in this study.

An immediate highlight of the results here is the presence of states with exotic $J^{PC} = 1^{-+}, 0^{+-}, 2^{+-}$ quantum numbers forbidden by quark models which suggests that QCD supports exotic states beyond quark models. This result would not have been obtained without a reliable spin identification technique, as for example in $\Lambda^{PC} = T_1^{-+}$, one needs to be able to robustly distinguish states of $J^{PC} = 1^{-+}$ which is an exotic quantum number and $J^{PC} = 4^{-+}$ which is not. For a better understanding of these exotic states

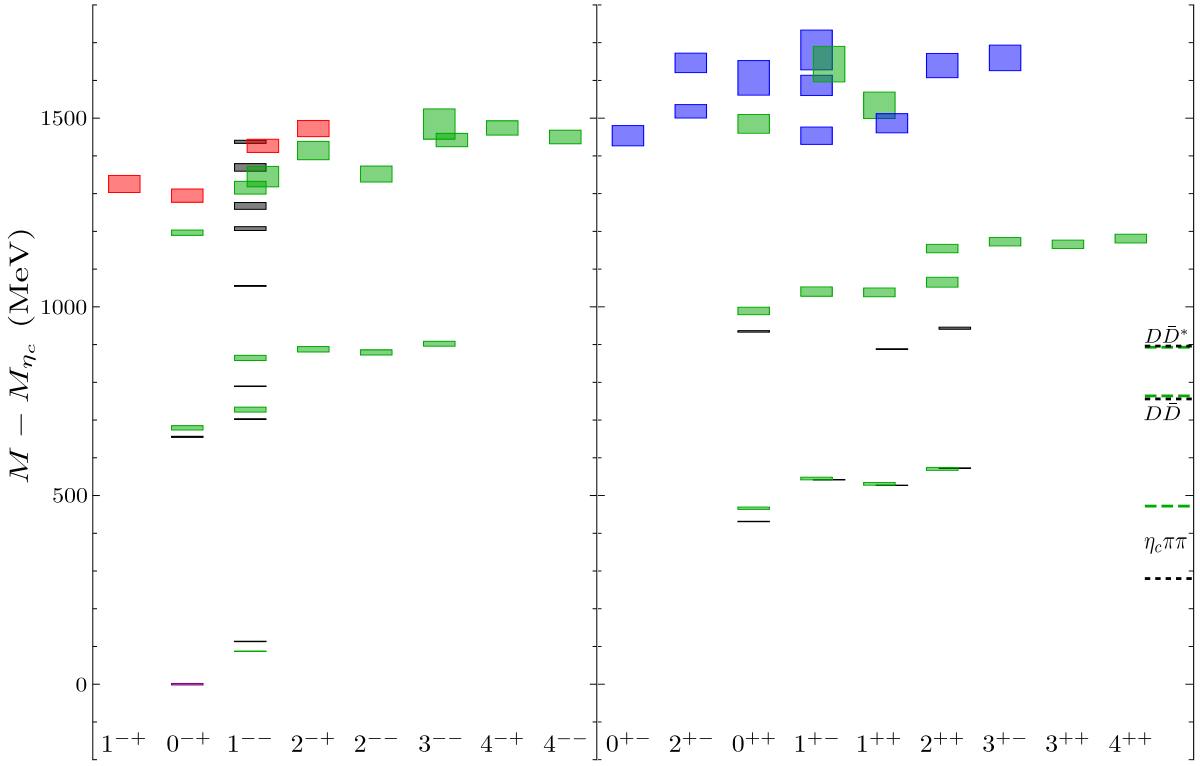

Figure 3.5: Charmonium spectrum up to around 4.5 GeV labelled by J^{PC}. Green, red and blue boxes show the energy levels that I computed whilst black boxes are experimental values taken from the PDG summary tables [78]. As discussed in the text, the calculated (experimental) energy levels are quoted with the calculated (experimental) η_c mass subtracted. The vertical size of the boxes represents the one-sigma statistical (experimental) uncertainty on either side of the mean. Red and blue boxes correspond to states identified as hybrid mesons grouped respectively into the lightest and first-excited supermultiplet as described in the text. Coarse green (fine grey) dashed lines show the location of some of the relevant thresholds for strong decay using computed (experimental) masses.

from a phenomological perspective, a model-depedent interpretation is given in the next section.

3.4 Interpretation of spectrum

Many of the states that I extracted appear to follow the usual $n^{2S+1}L_J$ pattern predicted by quark models [11]. The ground state S-wave set $[0^{-+}, 1^{--}]$ is observed along with its first radial excitation at ≈ 800 MeV and a second radial excitation at ≈ 1200 MeV. In the same parity sector, the D-wave states $[(1,2,3)^{--}, 2^{-+}]$ are found at ≈ 900 MeV along with the radial excitation at ≈ 1500 MeV. Below the $D\bar{D}$ threshold, there is a P-wave supermultiplet $[(0,1,2)^{++}, 1^{+-}]$ and its first radial excitation and part of the second radial excitation are found at $\approx 1000, 1500$ MeV respectively. Finally, the F-wave supermultiplet $[(2,3,4)^{++}, 3^{+-}]$ is found at ≈ 1200 MeV and some G-wave states are found at ≈ 1500 MeV. Extracting the remaining G-wave $J = 5$ state reliably would require four or more derivative single-meson operators in the calculation.

This quark model identification is further guided using the expected behaviour of overlaps in terms of a non-relativistic quark model [84, 85] by comparing operator-state overlaps for different states within a supermultiplet. For example, consider the operators $(\pi_{\mathrm{NR}} \times D^{[1]}_{J_D=1})^{J=1}$ with $J^{PC} = 1^{+-}$ and $(\rho_{\mathrm{NR}} \times D^{[1]}_{J_D=1})^{J=1}$ with $J^{PC} = (0,1,2)^{++}$, where $\pi_{\mathrm{NR}} = \frac{1}{2}\gamma_5(1-\gamma_0)$ and $\rho_{\mathrm{NR}} = \frac{1}{2}\gamma_i(1-\gamma_0)$. In this model, these operators have the structure of a quark-antiquark pair in a gauge-covariant version of a P-wave with $S = 0$ (π_{NR}) or $S = 1$ (ρ_{NR}). It is expected that the overlap values for each of these operators will be similar for all the states within a given supermultiplet. I found that the states within the proposed P-wave supermultiplet do indeed have large overlaps onto these operators[1] and their overlaps are found to be of similar value as shown in Figure 3.6 which provides further evidence that they belong to the same supermultiplet. Similar patterns were observed for the other supermultiplets. It is also interesting to measure the

[1]Technically, the operator is subduced but recall that the overlaps of a state onto a given operator of spin J are independent of the lattice irrep it is subduced to.

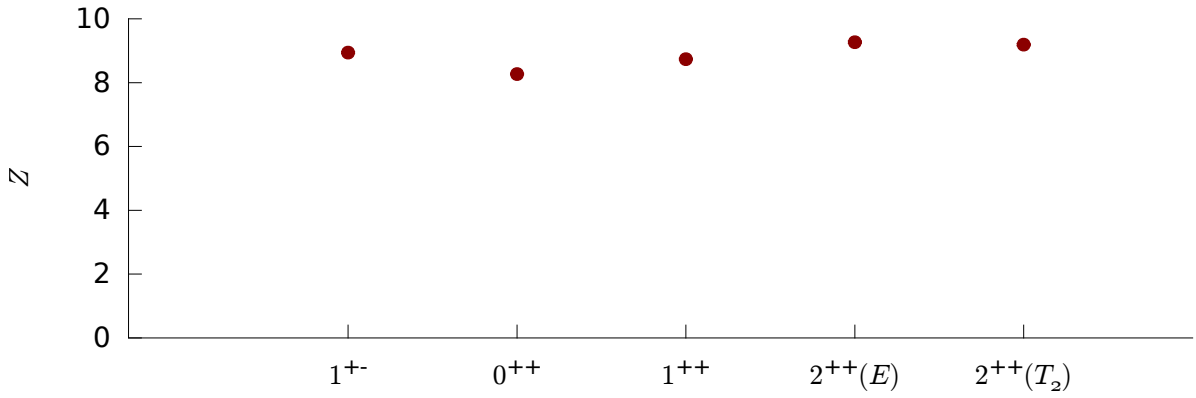

Figure 3.6: Operator-state overlaps, Z, of states suspected of belonging in the P-wave supermultiplet onto one of the operators $(\rho_{\mathrm{NR}} \times D^{[1]}_{J=1})^{J=0,1,2}$ or $(\pi_{\mathrm{NR}} \times D^{[1]}_{J=1})^{J=1}$. Error bars are smaller than the points.

overlap onto operators with $\frac{1}{2}\gamma_5(1+\gamma_0)$ and $\frac{1}{2}\gamma_i(1+\gamma_0)$ which are expected to be zero in the non-relativistic limit. These overlap values were indeed found to be relatively small which suggests that charmonium is fairly non-relativistic. Further quantitative conclusions cannot be made since the matrix elements require renormalisation.

After identifying the conventional quark model states, there are a plethora of remaining states around 1500 MeV, coloured in red and blue, in Figure 3.5. As mentioned earlier, some of these states have exotic J^{PC} quantum numbers and therefore, cannot solely be explained as a quark-antiquark pair. The near degeneracy of these energies gives a hint that they may have the same structure and belong to some supermultiplet of states. It is found that all of these states have a dominant overlap onto the hybrid meson operators that are proportional to the gluonic field-strength tensor, for example see the fourth state in Figure 3.3. In addition, the energy levels either have worse statistical precision or are not completely extracted at all if the hybrid meson operators are not included in the basis of interpolating operators. The four states with $J^{PC} = [(0,1,2)^{-+}, 1^{--}]$, coloured red in the figure, are consistent with the pattern of states predicted to form the lightest hybrid supermultiplet in the bag model [86, 87] and the P-wave quasiparticle gluon approach [88] and furthermore, this is not the pattern

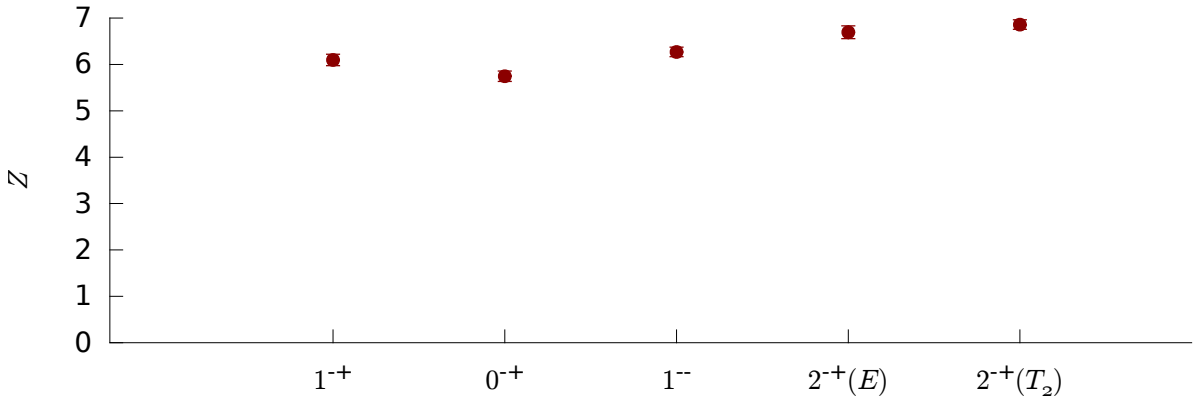

Figure 3.7: Operator-state overlaps, Z, of states suspected of belonging in the lightest hybrid supermultiplet onto one of the operators $(\rho_{\mathrm{NR}} \times D^{[2]}_{J=1})^{J=0,1,2}$ or $(\pi_{\mathrm{NR}} \times D^{[2]}_{J=1})^{J=1}$.

expected in the flux-tube model [89]. In more general terms, the pattern is consistent with a model where a quark-antiquark pair is coupled to a 1^{+-} gluonic excitation. In addition, the positive parity states with $J^{PC} = [0^{+-}, (1^{+-})^3, (2^{+-})^2, 3^{+-}, (0,1,2)^{++}]$, coloured in blue, are consistent with the number of states in the first excited hybrid supermultiplet where the quark-antiquark pair is in P-wave relative to the gluonic excitation. Whilst hybrid charmonia with exotic J^{PC} quantum numbers have been observed in lattice QCD calculations as early as 1997 [90], this calculation provides a much more comprehensive extraction of the charmonium spectrum with a reliable spin identification method such that the supermultiplets have been identified, placing strong constraints on the allowed hybrid meson models.

Further evidence of this hybrid meson model identification can be made by investigating the expected operator-overlaps onto the states [85] in greater detail as with the conventional quark model states. Consider for example, the operators $(\rho_{\mathrm{NR}} \times D^{[2]}_{J=1})^{J=0,1,2}$ with $J^{PC} = (0,1,2)^{-+}$ and $(\pi_{\mathrm{NR}} \times D^{[2]}_{J=1})^{J=1}$ with $J^{PC} = 1^{--}$ which have the structure of a colour-octet quark-antiquark pair in S-wave with $S = 1$ (ρ_{NR}) or $S = 0$ (π_{NR}) coupled to a gluonic excitation with $J^{PC} = 1^{+-}$. The expectations within the model are that the states in a supermultiplet should have a similar overlap value onto the relevant operator. Figure 3.7 shows the operator-state overlaps of the red states onto

these operators and they are indeed found to be similar which supports the identification of the states to belong in the lightest hybrid supermultiplet where a quark-antiquark pair in S-wave is coupled to a 1^{+-} gluonic excitation. Similar observations are made for the blue states to identify them as the first-excited hybrid supermultiplet with the quark-antiquark pair in P-wave relative to the 1^{+-} gluonic excitation. These results also suggest that a gluonic excitation has a mass of $\mathcal{O}(1500)$ MeV. Finally, the overall pattern and energy scale of the gluonic excitation is found to be consistent with other lattice QCD results found previously in the light meson sector [69, 91], light baryon sector [92], hidden-charm sector [76] and open-charm sector [93].

3.5 Systematic uncertainties and comparison with experimental results

With a phenomological understanding of these states in the spectrum, I now draw some comparisons with experimental results. Figure 3.5 shows the computed spectrum with the experimental states given by the black boxes. Note that the extracted levels only show the statistical uncertainty. For the low-lying states below 600 MeV which are stable and below the kinematic thresholds, there are some quantitative discrepancies between the experimental and extracted states, especially the S-wave hyperfine splitting which is underestimated. One of the largest systematic effects could possibly come from the discretisation of QCD as discussed in Ref. [76]. Other systematic uncertainties could arise from finite-volume effects although these are expected to be exponentially small due to $M_{\eta_c} L \sim 50$, and scale setting and quenching of the charm quark which were discussed in the previous chapter. Another error could stem from the unphysically heavy light quarks – one of the main purposes of this study is to explore this effect and further discussion will be postponed to the next section. Despite all these possible systematic effects and a full precision calculation being beyond the scope of the study, the qualitative pattern of states below threshold is found to be in good agreement with

the experimental observations. Above threshold for strong decay, the unstable nature is not accounted for in these calculations without including interpolating operators of multi-meson structure. This gives rise to a systematic uncertainty that is difficult to estimate and the next chapters will outline the strategy to address this issue. For now, a conservative approach is to consider the uncertainty to be of the order of the width of a given state [69].

Moving up to the excited spectrum in $J^{PC} = 1^{--}$, this channel is interesting because there is clearly an excess number of states found experimentally compared to the quark model. The $\psi(2S)$ and $\psi(3770)$ could possibly be identified with the computed $^3S_1$ and $^3D_1$ state. The hybrid meson that was extracted in this channel could be a suitable candidate for the exotic states $X(4260)$ or $X(4360)$. However, it is important to mention again that these energy levels are above the kinematic threshold and the unstable nature is not properly taken into account. To draw stronger conclusions, a calculation involving the extraction of multi-meson states would be required to obtain the scattering information. Another route would be to calculate the radiative transitions between states from lattice QCD which can be measured experimentally but this will require techniques beyond the scope of this study.

A significant discrepancy is seen in the 1^{++} channel where the $X(3872)$ resides near the $D\bar{D}^*$ threshold and the lattice result significantly overshoots this energy. However, the close proximity of the $X(3872)$ to the $D\bar{D}^*$ threshold suggests that the relevant multi-meson interpolating operators are required to reliably extract this state. Once again, the technology to tackle this problem will be discussed in future chapters. Another consideration is that the light quarks are degenerate in this lattice calculation which should have negligible effects on the majority of the results but $X(3872)$ has significant isospin-violating decays so that the light quarks may need to be non-degenerate to suitably probe this exotic state.

3.6 Comparison of spectra at two light quark masses

This work is compared with previous charmonium results that were calculated on the 24^3 lattice with a light quark mass corresponding to $M_\pi = 391$ MeV [76] described in Section 2.9. The comparison of spectra is shown in Figure 3.8 where for each J^{PC}, the $M_\pi = 236$ MeV results are shown by the darker box in the left column and the $M_\pi = 391$ MeV results are shown by the lighter box in the right column. The light quark dependence has an effect through the sea quark content in the dynamical gauge field configurations. In general, only a mild light quark mass dependence is observed throughout the spectra with no change in the overall pattern of states. The low-lying states are generally consistent between the two ensembles within statistical uncertainities except for the hyperfine splitting, $M_{J/\psi} - M_{\eta_c}$, where a small but statistically significant increase of about 8 MeV is found as the light quark mass is decreased. Looking at the excited states in the spectra, the energy levels are found to be generally higher at the smaller light quark mass, especially for the hybrids. However, it is important to note that the unstable nature of states above threshold is not taken into account which may have a significant impact. Despite this, the overall pattern of the quark model and hybrid meson supermultiplets is unaffected by decreasing the light quark mass. In summary, the decrease in light quark mass does not affect the overall qualitatives features or pattern of the spectrum.

One other observation to emphasise is that the spectrum here was calculated on a lattice with spatial extent $L \approx 3.8$ fm whilst the $M_\pi = 391$ MeV spectrum used a lattice with $L \approx 2.9$ fm. This drastic difference in volumes would have a huge effect on the energies of multi-meson states. To illustrate this, consider the energy of two mesons overall at rest assuming they do not interact,

$$E = \sqrt{M_1^2 + \vec{P}^{\,2}} + \sqrt{M_2^2 + \vec{P}^{\,2}} \tag{3.7}$$

where the momentum is quantised, $\vec{P} = \frac{2\pi}{L}\vec{n}$, when imposing periodic boundary conditions. For a given non-zero momentum, the energy decreases with increasing volume

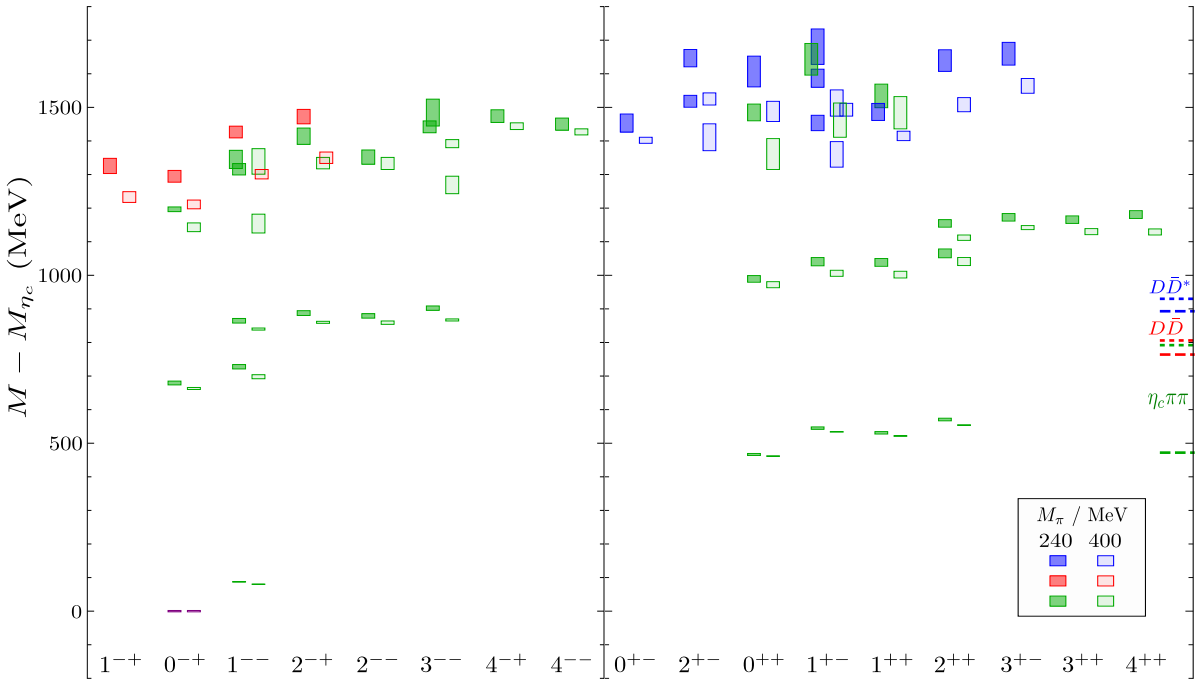

Figure 3.8: Charmonium spectra, labelled by J^{PC}, with $M_\pi = 236$ MeV (left column of darker boxes for each J^{PC}) compared to the spectrum with $M_\pi = 391$ MeV from Ref. [76] (right column of lighter boxes for each J^{PC}). As in earlier figures, red and blue boxes denote states identified as part of the lighest and first-excited supermultiplet of hybrid mesons. Dashed lines show some of the relevant thresholds using computed masses for $M_\pi = 236$ MeV (coarse dashing) and $M_\pi = 391$ MeV (fine dashing): green gives $\eta_c\pi\pi$, red is $D\bar{D}$ and blue gives $D\bar{D}^*$.

and there is no clear sign of this between the two spectra in Figure 3.8. Therefore, there are no obvious indications that I have extracted the complete spectrum that includes multiquark states. In fact, there are clear examples [69, 94, 75] which show that the construction of operators resembling multi-meson states is required to reliably extract the energies of such states which leads me to the next chapter on how to tackle this problem.

Chapter 4

Exotic Flavour States

In the previous chapter, one major caveat of the calculation was that the unstable nature of states above multi-meson thresholds was not taken into account and meson-meson levels were not extracted. Correlation functions of single-meson operators contain every possible state in the spectrum but if the overlap of a given meson-meson state is small onto all the single-meson operators, it may not be possible to reliably extract the energy of that state in a practical calculation. It is well known now that a reliable calculation of the finite-volume spectra requires a sufficiently diverse basis of operators that can suitably interpolate all the states in the energy region of interest [94, 75]. To overcome this limitation, I will give a review of one possible construction of a class of operators with structures resembling a pair of mesons to interpolate the meson-meson states. These meson-meson operators have proven very succesful in computations by HadSpec of finite-volume spectra which are then used to determine hadronic scattering amplitudes [67, 94, 95, 96, 75, 97, 98, 47, 99, 100] using the Lüscher method. The next chapter will introduce the Lüscher method that relates the finite-volume spectra from lattice QCD to the scattering amplitudes in infinite volume. For this chapter, I will concentrate on the reliable extraction of finite-volume spectra by using a sufficiently diverse set of operators and in particular, I will calculate spectra in exotic flavour channels, i.e. flavour quantum numbers that are not accessible by a quark-antiquark. The complete and reliable extraction of the finite-volume spectra is absolutely crucial to determine the correct scattering amplitudes. For example, see the systematic tests in studies of isospin-1 $\pi\pi$ scattering such as Ref. [94, 75] which attempt to compute scattering amplitudes, using spectra extracted with a operator basis consisting only of single-meson operators, and do not reproduce the resonance properties of the ρ.

Up until this work, scattering calculations by HadSpec have involved extraction of finite-volume (pseudo)scalar-(pseudo)scalar energy levels which are the simplest meson-meson type. The situation becomes more complicated when the mesons in the meson-meson levels have intrinsic spin and it will be explained in more detail later in the next section how this can lead to there being multiple finite-volume energy levels in the spectrum associated with a meson-meson. I will discuss how these multiple energy levels arise and how a sufficiently diverse set of meson-meson operators is needed to extract all these levels in the energy region of interest. This work is the first time that such multiple meson-meson levels were extracted by including all the relevant meson-meson operators. An example of where this would be interesting is to describe $D\bar{D}^*$ scattering which is relevant for the $X(3872)$ and therefore, it is important to be able to employ the right technology to extract and disentangle all the energy levels correctly in order to subsequently calculate the scattering amplitudes.

In addition to the meson-meson operators that I will review, I will construct a general class of four-quark operators resembling compact tetraquarks which have a spatially-local structure compared to the meson-meson operators. These operators can share the same quantum numbers as the meson-meson operators but so far, they have been omitted in scattering amplitude calculations from lattice QCD. Once again to emphasise, not including a sufficiently diverse set of relevant operators in the calculation could lead to an unreliable extraction of the finite-volume spectra and in turn, incorrect scattering amplitudes. Hence, it is desirable to consider such operators resembling tetraquarks, with the relevant colour-flavour-spin structures, and investigate whether their inclusion has any impact on the extracted spectra. In the previous chapter, the reliable extraction of energy levels of hybrid mesons required operators with a hybrid meson structure. In the same way, it may be expected that operators resembling tetraquarks will be required to reliably interpolate states of tetraquark nature. Operators resembling tetraquarks in the charm sector have been constructed and used to calculate spectra in other studies such as Refs. [101, 102, 103] but those studies have mostly been limited to one channel. A

comparison of these studies with the results here will be made later. It would be desirable to have a completely general construction of lattice operators resembling tetraquarks for lattice calculations in the same vein as the general class of single-meson operators in the previous chapter.

In this chapter, I will give a review of a construction of meson-meson operators in Section 4.1. Section 4.2 will present a construction of a general class of operators resembling compact tetraquarks which transform irreducibly under the symmetries of the lattice, have a range of colour-flavour-spin structures and respect other relevant discrete symmetries. I will discuss the strategy to perform calculations involving these tetraquark operators within the distillation framework in Section 4.3 and then give the specific calculational details in Section 4.4. As a demonstration of the tetraquark operators in conjunction with the meson-meson operators, I compute exotic flavour spectra in the isospin-1 hidden charm sector in Section 4.5 which is where the charged Z states reside, and the doubly-charmed sector in Section 4.6. These channels are particularly interesting experimentally and phenomologically as tetraquark states are expected and some of these channels have never been computed before in a lattice QCD calculation. Some discussion of systematic effects and stability of the extracted spectra will be given in Section 4.7. Section 4.8 will conclude this chapter with a discussion and interpretation of the results whilst comparing with experimental and theoretical studies. The work presented here was published in Ref. [104].

4.1 Meson-meson operators

I begin by reviewing the construction of *meson-meson operators* that have a structure resembling two mesons, M_1 and M_2. Following Refs. [67, 94], the meson-meson operator is constructed from products of two single-meson operators with overall momentum $\vec{P}$,

$$\mathcal{O}_{\Lambda,\mu}(\vec{P},t) = \sum_{\mu_1,\mu_2} \sum_{\substack{\vec{k}_i \in \{\vec{k}_i\}^* \\ \vec{k}_1+\vec{k}_2=\vec{P}}} \mathcal{C}(\vec{P},\Lambda,\mu;\vec{k}_1,\Lambda_1,\mu_1;\vec{k}_2,\Lambda_2,\mu_2)\ \Omega^{M_1}_{\Lambda_1,\mu_1}(\vec{k}_1,t)\Omega^{M_2}_{\Lambda_2,\mu_2}(\vec{k}_2,t) \quad (4.1)$$

where $\Omega^{M_i}_{\Lambda_i,\mu_i}$ is an optimised operator consisting of a linear combination of single-meson operators for interpolating stable meson M_i transforming in lattice irrep Λ_i (row μ_i) as described in Section 2.6. The implementation of optimised operators removes contamination from excited states and gives an early plateau onto the desired ground state meson. $\mathcal{C}$ are generalised Clebsch-Gordan coefficients that couple $\Lambda_1(\vec{k}_1) \otimes \Lambda_2(\vec{k}_2) \to \Lambda(\vec{P})$. The set of all momenta related to $\vec{k}_i$ by an allowed lattice rotation is given by the star of $\vec{k}_i$, $\{\vec{k}_i\}^*$, and the sum runs over this star with $\vec{k}_1 + \vec{k}_2 = \vec{P}$. Clebsch-Gordan coefficients are tabulated in Ref. [67] where a more detailed discussion on their derivation including conventions can be found. As mentioned already, the momentum is quantised to $\vec{P} = \frac{2\pi}{L}(n_x, n_y, n_z)$ where (n_x, n_y, n_z) is a triplet of integers and $[n_x n_y n_z]$ is used as a shorthand notation to denote the momentum type. For the rest of this chapter, I will consider $\vec{P} = 0$ and in this case, parity is a good quantum number.

In the ideal scenario, one should use a large number of meson-meson operators that share the same quantum numbers, with the individual single-meson operators combined in many different momentum and lattice irrep combinations, to calculate the correlation functions. In practice, the computational cost increases with each additional operator in the operator basis so some consideration as to which operators are most relevant is important. The operator basis is chosen here by considering the non-interacting meson-meson energy levels, with all possible meson pairs that give the desired flavour and other quantum numbers, in the energy region of interest. Once these levels are mapped out within an energy region, the corresponding meson-meson operators to these non-interacting levels are included in the basis as a minimum requirement. These levels are calculated from the relativistic dispersion relation

$$a_t E = \sqrt{(a_t M_1)^2 + \left(\frac{2\pi}{\xi L/a_s}\right)^2 \vec{n}_1^2} + \sqrt{(a_t M_2)^2 + \left(\frac{2\pi}{\xi L/a_s}\right)^2 \vec{n}_2^2} \tag{4.2}$$

for stable single-mesons.

In cases when a meson has non-zero intrinsic spin, there can be multiple ways to couple the orbital and spin angular momenta together in a meson-meson to obtain a given J^P. Taking an example in the continuum and infinite-volume, a pseudoscalar and vector

couple to $J^P = 1^+$ in S-wave and to $J^P = (1,2,3)^+$ in D-wave giving two ways to access $J^P = 1^+$. For scattering, this leads to these partial waves being dynamically coupled and even though there is only one threshold, the two partial waves should be considered as coupled channels. It is important to emphasise that this coupling of partial waves is physical and should not be confused with the unphysical mixing of angular momentum due to the breaking of rotational symmetry.

To see the effect of this on the spectrum in the finite-volume, consider the pseudoscalar with $\vec{k}_1 = [100]$ and the vector with $\vec{k}_2 = [-100]$ where the pseudoscalar-vector is overall at rest in the lattice irrep $\Lambda^P = T_1^+$. The single-mesons transform in the irreps of the little group Dic_4 as given in Table 2.2: the pseudoscalar subduces into the A_2 irrep while the helicity-0 and helicity-1 components of the vector subduce into the A_1 and E_2 irreps respectively. This gives two distinct energy levels in $\Lambda^P = T_1^+$ from the linearly independent irrep combinations, $A_2 \otimes A_1$ and $A_2 \otimes E_2$ [105], and these two pseudoscalar-vector levels would be degenerate in the non-interacting limit. A reliable extraction, in lattice QCD calculations, of the finite-volume energy levels associated with these two non-interacting levels requires the two corresponding linearly-independent operators transforming in T_1^+, obtained separately from the irrep combinations $A_2 \otimes A_1$ and $A_2 \otimes E_2$. A full demonstration of this will be shown later.

As another example, consider the non-interacting pseudoscalar-vector level when the mesons have momentum $\vec{k}_1 = -\vec{k}_2 = [110]$, where the relevant little group is Dic_2. From Table 2.2, the pseudoscalar transforms in the A_2 irrep and the helicities of the vector subduce into A_1, B_1 and B_2. There are a total of three linearly-independent combinations to obtain T_1^+ from coupling $A_2 \otimes A_1$, $A_2 \otimes B_1$, $A_2 \otimes B_2$ and therefore, there are three energy levels associated with this pseudoscalar-vector level. The three corresponding linearly-independent operators need to be included in the operator basis to reliably extract these levels.

In general, it is necessary to include a sufficient number of relevant meson-meson operators that are capable of extracting and disentangling these multiple energy levels

and this work is the first time that this was ever done in a lattice QCD calculation. I will show a systematic test later where not all the relevant meson-meson operators within an energy region are used and the complete finite-volume spectrum is not extracted. The importance of extracting these multiple energy levels should be emphasised since the scattering amplitudes are obtained from the finite-volume spectra.

4.2 Tetraquark operators

In the previous section, I reviewed the construction of operators resembling a pair of mesons. In this section, I will construct a general class of interpolating operators with the same quark content resembling a compact tetraquark by combining a diquark operator with an anti-diquark operator. The diquark operator is built from two quark fields coupled together to obtain appropriate colour, flavour and spin quantum numbers and analogously, the anti-diquark operator is built from two antiquarks. The diquark and anti-diquark are then combined into a colour singlet with the desired flavour and spin. These constructions provide, with no loss of generality, a convenient way to build a diverse class of *tetraquark operators* which have the required quantum numbers and respect appropriate symmetries. As with the single-meson operators, these operators are first constructed in the continuum and then subduced to transform definitely in some lattice irrep.

To construct the diquark operator, two quark fields are coupled together to definite colour, flavour and continuum spin irreps. In colour space, the quarks belong in the fundamental representation of $\mathrm{SU}(3)_C$ and so the diquark belongs in either the anti-symmetric $\underline{\bar{3}}$ representation or the symmetric $\underline{6}$ representation. In flavour space, I use $\mathrm{SU}(3)_F$ constructions to form a convenient basis of operators as any arbitrary flavour combination can be constructed from a linear combination of these operators. Note that this does not require or imply any assumption of $\mathrm{SU}(3)_F$ symmetry in the theory and this is just a choice of convenience. The up, down and strange quark (u, d, s) quark belong in the fundamental representation of $\mathrm{SU}(3)_F$ and the charm (c) quark is placed

in a flavour singlet. The quarks are coupled together to obtain the desired flavour irrep with the possible irrep combinations being $\underline{1}, \underline{3}, \bar{\underline{3}}$ or $\underline{6}$. For example, when coupling two u, d, s quarks as $\underline{3} \otimes \underline{3} \to \bar{\underline{3}}$, this irrep contains a component with flavour quantum numbers (isospin, strangeness) = (0,0) with flavour structure $\frac{1}{\sqrt{2}}(ud - du)$, and a $(1/2, -1)$ multiplet with $\frac{1}{\sqrt{2}}(us - su)$ and $\frac{1}{\sqrt{2}}(ds - sd)$. Another example would be coupling a c quark with a u, d, s quark as $\underline{1} \otimes \underline{3} \to \underline{3}$ which contains a (0,-1) component with flavour structure cs, and a $(1/2, 0)$ multiplet with flavour structure cu and cd.

Explicitly, the diquark operator in colour irrep R (row r), flavour irrep F (row f) and continuum spin J (J_z component m) is given by

$$\delta^{J[\Gamma]}_{RF;rfm}(\vec{x}, t) = \sum_{r_a, r_b} \langle \underline{3}, r_a; \underline{3}, r_b | R, r \rangle \sum_{f_a, f_b} \langle F_a, f_a; F_b, f_b | F, f \rangle \; q^T_{F_a;r_a f_a}(\vec{x}, t) C\Gamma_m q_{F_b;r_b f_b}(\vec{x}, t) \tag{4.3}$$

where spinor indices have been suppressed and $\langle D_a, d_a; D_b, d_b | D, d \rangle$ are Clebsch-Gordan coefficients that couple $D_a \otimes D_a \to D$ with d_a, d_b and d denoting the irrep rows. SU(3) Clebsch-Gordan coefficients can be calculated from products of SU(2) Clebsch-Gordan coefficients and isoscalar factors taken from Refs. [106, 107]. C is the charge conjugation matrix such that $\gamma_0 = C\gamma_0^T C$. Γ is a Dirac gamma matrix which determines the properties of the diquark operator, such as its spin J (row m), and the full details are summarised in Table 4.1. Under proper Lorentz transformations, the diquark operator transforms in the same way as the analogous fermion bilinear with the same Γ and this is summarised in the table. Under a parity transformation, the operator transforms to $\mathcal{P}\delta(\vec{x}, t)\mathcal{P}^{-1} = \eta_P q^T(-\vec{x}, t) C\Gamma q(-\vec{x}, t)$ where $\eta_P = \pm 1$ which later determines the parity of the tetraquark operator (see the table for values). Choosing Γ gives access to spins up to $J = 1$ – higher spins or excitations can be obtained by including gauge-covariant derivatives in a similar way to the single-meson operator constructions. I will not describe them here since this study is mainly concerned with the low-lying spectrum as a first demonstration of these operators.

Analogously, the anti-diquark operator consists of antiquarks which belong in the anti-fundamental representation of $\mathrm{SU}(3)_C$ and therefore couple to colour irrep $\underline{3}$ or $\bar{\underline{6}}$.

	1	γ_5	$\gamma_0\gamma_5$	γ_0	γ_i	$\gamma_i\gamma_0$	$\gamma_5\gamma_i$	$[\gamma_i,\gamma_j]$
Γ	a_0	π	π_2	b_0	ρ	ρ_2	a_1	b_1
J	0	0	0	0	1	1	1	1
η_P	$-$	$+$	$+$	$-$	$+$	$+$	$-$	$-$
h_Γ	$+$	$-$	$+$	$+$	$+$	$-$	$+$	$-$
s_Γ	$-$	$-$	$-$	$+$	$+$	$+$	$-$	$+$

Table 4.1: For different Dirac gamma matrices, the table gives the notation Γ used to denote the gamma matrix, the continuum spin J, the parity factor η_P, the hermiticity factor h_Γ and the spin coupling symmetry s_Γ.

The up, down and strange antiquarks belong in the $\underline{\bar{3}}$ irrep of SU(3)$_F$ and the charm antiquark is in the singlet giving access to the flavour representations $\underline{1}, \underline{3}, \underline{\bar{3}}, \underline{\bar{6}}$. The anti-diquark operator is defined as

$$\bar{\delta}^{J[\Gamma]}_{RF;rfm}(\vec{x},t) = \sum_{r_a,r_b} \langle \underline{\bar{3}}, r_a; \underline{\bar{3}}, r_b | R, r\rangle \sum_{f_a,f_b} \langle F_a, f_a; F_b, f_b | F, f\rangle \; \bar{q}_{F_a;r_a f_a}(\vec{x},t) \Gamma_m C \bar{q}^T_{F_b;r_b f_b}(\vec{x},t) \tag{4.4}$$

where compared to the diquark operator, the charge conjugation matrix enters after the Dirac gamma matrix so that under the charge conjugation operator, $\mathcal{C}\,\bar{\delta}^{J[\Gamma]}_{RF}\,\mathcal{C}^{-1} = \delta^{J[\Gamma]}_{\bar{R}\bar{F}}$. This provides a convenient definition of tetraquark operators with definite G-parity to be discussed later.

To obtain creation operators, the Hermitian conjugate is taken, $\delta^\dagger(\vec{x},t) = h_\Gamma s_C s_F \bar{\delta}(\vec{x},t)$, where the conjugation factor coming from the Dirac gamma matrix, $h_\Gamma = \pm 1$, is given in Table 4.1. $s = \xi_1\xi_3$ are SU(3) symmetry factors arising from the exchange symmetry of the colour (s_C) and flavour (s_F) Clebsch-Gordan coefficients. The symmetry factor $\xi_1 = \pm 1$ arises from reversing the order of the SU(3) irreps,

$$\langle D_1, d_1; D_2, d_2 | D, d\rangle = \xi_1 \langle D_2, d_2; D_1, d_1 | D, d\rangle, \tag{4.5}$$

and the symmetry factor $\xi_3 = \pm 1$ arises from complex conjugating the irreps,

$$\langle D_1, d_1; D_2, d_2 | D, d \rangle = \xi_3 \langle \bar{D}_1, \bar{d}_1; \bar{D}_2, \bar{d}_2 | \bar{D}, \bar{d} \rangle. \tag{4.6}$$

In this work, I will use the phase conventions given in Refs. [106, 107].

Due to Fermi symmetry, when the flavour irreps of the (anti)quarks are identical in the (anti-)diquark operator, the overall colour-flavour-spin coupling must be antisymmetric. The advantages of using this diquark formulation to construct a tetraquark operator is that the Fermi symmetry is manifestly apparent and this provides a constraint on the allowed diquark configurations. The symmetry of exchanging the quarks arising from spin $(C\Gamma)_{\alpha\beta} = s_\Gamma (C\Gamma)_{\beta\alpha}$ is given in Table 4.1.

Tetraquark operators are formed by coupling a diquark operator and anti-diquark operator to a colour singlet with definite flavour and spin. The only possible diquark and anti-diquark colour combinations which give a colour singlet are $\underline{\bar{3}} \otimes \underline{3}$ and $\underline{6} \otimes \underline{\bar{6}}$ restricting the number of possible diquark–anti-diquark configurations. The flavour quantum numbers of the tetraquark operator are obtained by coupling the appropriate flavour irreps of the diquark and anti-diquark and then choosing the desired row. The tetraquark operator, projected onto momentum $\vec{P}$ is,

$$\begin{aligned} \mathcal{T}^{J[\Gamma_1,\Gamma_2]}_{[R_1,R_2]F[F_1,F_2];fm}(\vec{P},t) = \sum_{\vec{x}} e^{i\vec{P}\cdot\vec{x}} \sum_{m_1,m_2} \langle J_1, m_1; J_2, m_2 | J, m \rangle \sum_{r_1,r_2} \langle R_1, r_1; R_2, r_2 | \underline{1} \rangle \\ \times \sum_{f_1,f_2} \langle F_1, f_1; F_2, f_2 | F, f \rangle \; \delta^{J_1[\Gamma_1]}_{R_1F_1;r_1f_1m_1}(\vec{x},t) \; \bar{\delta}^{J_2[\Gamma_2]}_{R_2F_2;r_2f_2m_2}(\vec{x},t) \, . \end{aligned} \tag{4.7}$$

In this chapter, only $\vec{P} = 0$ is considered and so this operator has definite parity P which is given by the product of the parity factors, η_P, from the gamma matrices Γ_1 and Γ_2. It is important to emphasise the differences between the tetraquark operators which contains one summation over the volume and the meson-meson operators in Equation 4.1 which contains two summations over the volume. In this sense to gain some intuition, the two operators have a different spatial structure where the tetraquark operators resemble the single-meson operators which also contain one summation whilst the meson-meson

operators can be thought of as extended objects. This point will be discussed in more detail in Section 4.7 in relation to the results later.

In channels where G-parity is a good quantum number, a tetraquark operator with definite G-parity is given by,

$$\mathcal{T}^{J[\Gamma_1,\Gamma_2],PG}_{[R_1,R_2]F[F_1,F_2];fm}(\vec{P}=\vec{0},t) = \mathcal{T}^{J[\Gamma_1,\Gamma_2]}_{[R_1,R_2]F[F_1,F_2];fm}(\vec{0},t) + \tilde{G}\,\mathcal{T}^{J[\Gamma_2,\Gamma_1]}_{[\bar{R}_2,\bar{R}_1]F[\bar{F}_2,\bar{F}_1];fm}(\vec{0},t)\,, \quad (4.8)$$

where $\tilde{G} = \pm 1$. This operator, under G-parity, has eigenvalue given by $G = \tilde{G}\xi_J\xi_1\xi_3$ where the symmetry factors arise from the Clebsch-Gordan coefficients in Equation (4.7). ξ_1, ξ_3 are the symmetry factors from $\mathrm{SU}(3)_F$ Clebsch-Gordan coefficients discussed earlier in Equations (4.5) and (4.6), and the symmetry factor $\xi_J = (-1)^{J-J_1-J_2}$ comes from reversing the order of the SU(2) Clebsch-Gordan coefficients. There is no symmetry factor arising from the $\mathrm{SU}(3)_C$ Clebsch-Gordan coefficients since they are always symmetric for a colour singlet.

Finally, the tetraquark operator is subduced to transform irreducibly under the symmetries of the lattice in the same manner as the single-meson operators and is given by

$$\mathcal{T}^{\Lambda[J[\Gamma_1,\Gamma_2]],P(G)}_{[R_1,R_2]F[F_1,F_2];f\mu}(\vec{P}=\vec{0},t) = \sum_m S^{J,m}_{\Lambda,\mu}\;\mathcal{T}^{J[\Gamma_1,\Gamma_2],P(G)}_{[R_1,R_2]F[F_1,F_2];fm}(\vec{P}=\vec{0},t)\,, \quad (4.9)$$

where S are the subduction coefficients. It is straightforward to generalise this to $\vec{P} \neq 0$ by constructing helicity operators and subducing to the little group of $\vec{P}$ as in the single-meson case.

4.3 Computing correlation functions with tetraquark operators

To calculate correlation functions involving tetraquark operators in the distillation framework, the tetraquark elementals are given by

$$\Psi^{\alpha\beta\gamma\delta}_{n_1n_2n_3n_4}(\vec{P}=\vec{0},t) = (C\Gamma_1)^{\alpha\beta}(\Gamma_2 C)^{\gamma\delta} \sum_{\vec{w}p,\vec{x}q,\vec{y}r,\vec{z}s} \mathbb{C}_{pqrs}\,\xi^\dagger_{n_3}(\vec{w}p;t)\xi^\dagger_{n_4}(\vec{x}q;t)\xi_{n_1}(\vec{y}r;t)\xi_{n_2}(\vec{z}s;t)\,, \quad (4.10)$$

where n_i index distillation vectors, Greek letters label the Dirac spinor indices and $\mathbb{C}_{pqrs}$ are combinations of $\mathrm{SU}(3)_C$ Clebsch-Gordan coefficients that couple the colour representations $\bar{\underline{3}} \otimes \bar{\underline{3}} \otimes \underline{3} \otimes \underline{3} \to \underline{1}$. Comparing with single-meson operators, the single-meson elementals in Equation (3.6) are matrices with $(4N_{\mathrm{vecs}})^2$ components whilst the tetraquark elementals are rank-4 with $(4N_{\mathrm{vecs}})^4$ independent components. Calculations using tetraquark operators, involving contractions over elementals and perambulators, are far more costly than with using the other operators described previously. Therefore, if the calculation including tetraquark operators is to be feasible, the number of distillation eigenvectors must not be too large. On the other hand, if the number of eigenvectors is too small, the tetraquark operator may be too smeared such that it does not sufficiently interpolate the states of interest and have poor resemblance to a compact tetraquark. To reach a compromise, the cost of contractions is kept reasonable by using a relatively small number of eigenvectors for tetraquark operators whilst maintaining a larger number of eigenvectors for the other operators by introducing a second distillation operator,

$$\tilde{\Box}(\vec{x}r, \vec{y}s; t) = \sum_{\tilde{n}=1}^{\tilde{N}_{\mathrm{vecs}}} \xi_{\tilde{n}}(\vec{x}r; t)\xi^{\dagger}_{\tilde{n}}(\vec{y}s; t) \tag{4.11}$$

composed of the lowest $\tilde{N}_{\mathrm{vecs}}$ eigenvectors of the gauge-covariant Laplacian where $\tilde{N}_{\mathrm{vecs}} < N_{\mathrm{vecs}}$. Quark and antiquark fields in tetraquark operators are smeared with $\tilde{\Box}$ whereas those in other operators are smeared with $\Box$. To see how this reduces the computational cost, consider a meson-meson operator of the form $\mathcal{O} \sim (\bar{c}\Box\Gamma\Box u)(\bar{d}\Box\Gamma\Box c)$ smeared with the original distillation operator and a tetraquark operator of the form $\mathcal{T} \sim \left((\tilde{\Box}c)^T C\Gamma(\tilde{\Box}u)\right)\left((\bar{c}\tilde{\Box})\Gamma C(\bar{d}\tilde{\Box})^T\right)$ smeared with the smaller operator. The connected contribution to the two-point correlation function between these two operators is, schematically,

$$\langle \mathcal{O}(t)\mathcal{T}(0)^{\dagger}\rangle \sim \Phi_{n_1 n_2}(t)\Phi_{n_3 n_4}(t)\tau_{\tilde{n}_3 n_1}(0,t)\tau_{\tilde{n}_4 n_3}(0,t)\tau_{n_4 \tilde{n}_1}(t,0)\tau_{n_2 \tilde{n}_2}(t,0)\Psi_{\tilde{n}_1\tilde{n}_2\tilde{n}_3\tilde{n}_4}(0)\,, \tag{4.12}$$

where $n_i = 1, \ldots, N_{\mathrm{vecs}}$, $\tilde{n}_i = 1, \ldots, \tilde{N}_{\mathrm{vecs}}$, and spinor indices are suppressed. Here, the perambulators $\tau(t,0)$ are $4N_{\mathrm{vecs}} \times 4\tilde{N}_{\mathrm{vecs}}$ rectangular matrices, $\Phi(t)$ are $4N_{\mathrm{vecs}} \times 4N_{\mathrm{vecs}}$

square matrices and $\Psi(0)$ is of rank-4 with $(4\tilde{N}_{\text{vecs}})^4$ components. The number of contractions to compute this quantity is clearly smaller than the case when the tetraquark operator is also smeared with $\Box$. The viability of having a lower number of distillation vectors for tetraquark operators and some tests of varying the number of vectors is discussed later in Section 4.7.

Another technique to further reduce the computation time involving tetraquark operators is to only calculate one half of the off-diagonal elements involving tetraquark operators in the two-point correlation function matrix and obtain the other half using the Hermiticity of the matrix. I performed some viability tests of this method with only single-meson operators by comparing the extracted spectrum from the full matrix and the triangular matrix. I generally found a marginal decrease in the statistical resolution with the triangular matrix but the central values were consistent which indicates this technique is feasible.

As in the previous chapter, contributions to the correlation functions where a charm quark and antiquark annihilate are neglected as they are expected to be small due to OZI suppression. As tests of these general constructions of tetraquark operators, I will study the isospin-1 hidden-charm sector and the isospin-0 doubly-charmed sector. The doubly-charmed sector is manifestly exotic as its flavour content cannot be accessed by a single-meson and due to the exclusion of charm quark annihilation, the isospin-1 hidden-charm sector is effectively exotic in flavour which means there are no single-meson operators in this channel. Therefore, only meson-meson and tetraquark operators will be used to calculate the matrix of two-point correlation functions in order to obtain the spectrum. A schematic representation of the types of Wick contractions required is shown in Figure 4.1.

Ideally, all of the possible tetraquark operators that can be constructed using this procedure should be included in the operator basis but the computational cost can become too high for the calculations to be practical. In some cases, I was able to include all the tetraquark operator constructions allowed by Fermi symmetry but in the majority

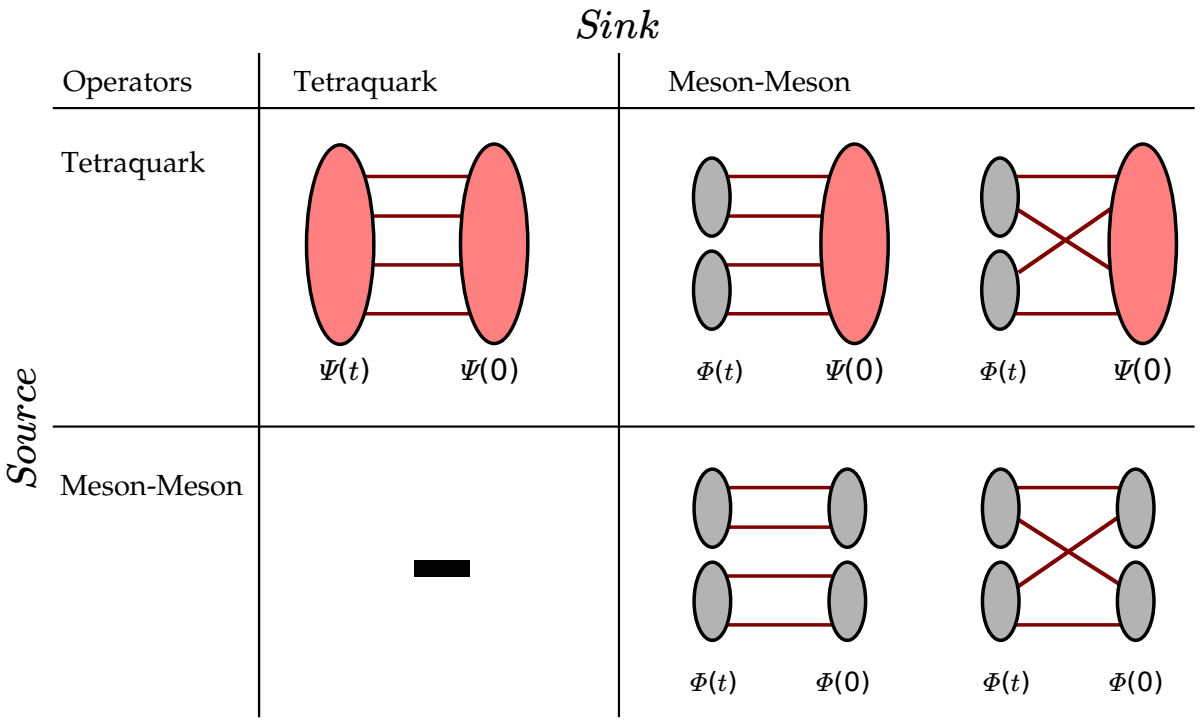

Figure 4.1: A schematic representation of the types of Wick contractions required to compute the two-point correlation function matrices involving tetraquark and meson-meson operators in this work. Φ (grey) is used to depict the single-meson elementals and Ψ (red) is used to depict the tetraquark elementals. Lines joining them denote perambulators.

of channels, the number of available operators is too large so I use a subset of tetraquark operators that are expected from phenomological models to overlap most strongly onto low-lying states. Some diquark model considerations are given in Appendix A and to summarise, it can be seen that tetraquark operators containing a diquark (anti-diquark) with a γ^5 or $\gamma^0\gamma^5$ gamma matrix and in colour irrep $\underline{\bar{3}}$ ($\underline{3}$) are expected to overlap most efficiently onto a ground-state tetraquark and at the very least, the operator basis should include such operators. However I found that the operators with γ^5 and $\gamma^0\gamma^5$ structures were not sufficiently distinct (i.e. the correlation function matrix contains approximately linearly-dependent rows/columns). Therefore, instead of having redundant operators in the basis, a selection of other operators were included to diversify the basis. The full list

of meson-meson and tetraquark operators for each channel that I investigated is found in the tables in Appendix B.

4.4 Calculational details

The calculations are performed on an anisotropic lattice with pion mass $M_\pi = 391$ MeV and size $(L/a_s)^3 \times (T/a_t) = 16^3 \times 128$ as a first demonstration where the computations are relatively affordable. Further details of the lattice can be found in Section 2.9. I will use $N_{\text{vecs}} = 64$ for meson-meson operators, which is adequate for scattering calculations on this volume [94], and $\tilde{N}_{\text{vecs}} = 24$ for tetraquark operators. Systematic tests of varying the number of eigenvectors will be presented in Section 4.7. Using several lattice volumes, the anisotropy was measured to be $\xi_\pi = 3.444(6)$ from the dispersion relation of the pion [67] and $\xi_D = 3.454(6)$ from the D [93]. I found, $\xi_{\eta_c} = 3.484(2)$, the anisotropy from the dispersion relation of the η_c on only the 16^3 volume. Since the anisotropy is only used in this chapter to compute the location of non-interacting meson-meson energy levels, which are mostly used as guides, I will use the value ξ_π for subsequent calculations.

For stable mesons, the non-interacting meson-meson energy levels are given by the relativistic dispersion relation in Equation 4.2. The masses of the relevant stable mesons on this lattice ensemble are given in Table 4.2 and when constructing meson-meson operators, the variationally-optimised operators for these mesons, $\Omega^M_{\Lambda\mu}$, are constructed from linear combinations of single-meson operators. An exception to this is the ρ meson which was found to be unstable on this lattice, with the mass above the $\pi\pi$ threshold [94]. For this case, the 'non-interacting $M - \rho$ energy levels' are considered, where the energy of M is computed from the relativistic dispersion relation and the ρ energies are directly obtained from the energy levels on this ensemble as given in Table 4.2, i.e. $E = \sqrt{m_M^2 + \vec{p}_M^{\,2}} + \rho^{\vec{p}}_\Lambda$. For the corresponding $M - \rho$ operators, the variationally optimised ρ operators, $\Omega^\rho_{\Lambda\mu}$, are given by linear combinations of meson-meson and single-meson operators [94] since single-meson operators alone do not reliably interpolate the ρ. It is important to point out that the only uses of the non-interacting energy levels are

Meson	Mass (MeV)
π	391.4(7)
D	1885.1(4)
D^*	2008.9(6)
D_s	1950.9(3)
D_s^*	2071.2(5)
η_c	2964.4(2)
J/ψ	3044.7(2)
χ_{c0}	3426.3(6)

$\rho_\Lambda^{\vec{p}}$	Energy (MeV)
$\rho_{T_1}^{[000]}$	890(5)
$\rho_{A_1}^{[100]}$	1027(4)
$\rho_{E_2}^{[100]}$	1089(5)

Table 4.2: Ground state masses of stable mesons (left), and the energy of the lowest-lying finite-volume energy level for lattice irrep Λ and momentum $\vec{p}$ relevant for the ρ meson denoted by $\rho_\Lambda^{\vec{p}}$ (right) as measured on this ensemble [67, 94, 76, 93]. Only the statistical uncertainty is quoted.

to show their location on finite-volume spectrum plots and indicate which meson-meson operators should be included in the operator basis. I now present computed spectra for a range of channels, beginning with a detailed discussion of the $\Lambda^{PG} = T_1^{++}$ irrep in the isospin-1 hidden charm sector.

4.5 Isospin-1 hidden charm spectra

To begin, I discuss some of the features of the spectrum computed in the $\Lambda^{PG} = T_1^{++}$ irrep of the isospin-1 hidden-charm sector (with flavour content $c\bar{c}l\bar{l}$ where the light quark and antiquark are coupled to isospin-1) before discussing other irreps in this sector. The lowest spin that subduces in this irrep is $J^{PG} = 1^{++}$. This J^{PG} is interesting because the charged $Z_c(3900)$ state is found in this channel in $J/\psi\pi$ scattering [108]. The irreps will be labelled by G-parity which is a good quantum number in isospin-1 whilst charge conjugation is not a good symmetry. Note that $C = -G$ in isospin-1 for the neutral

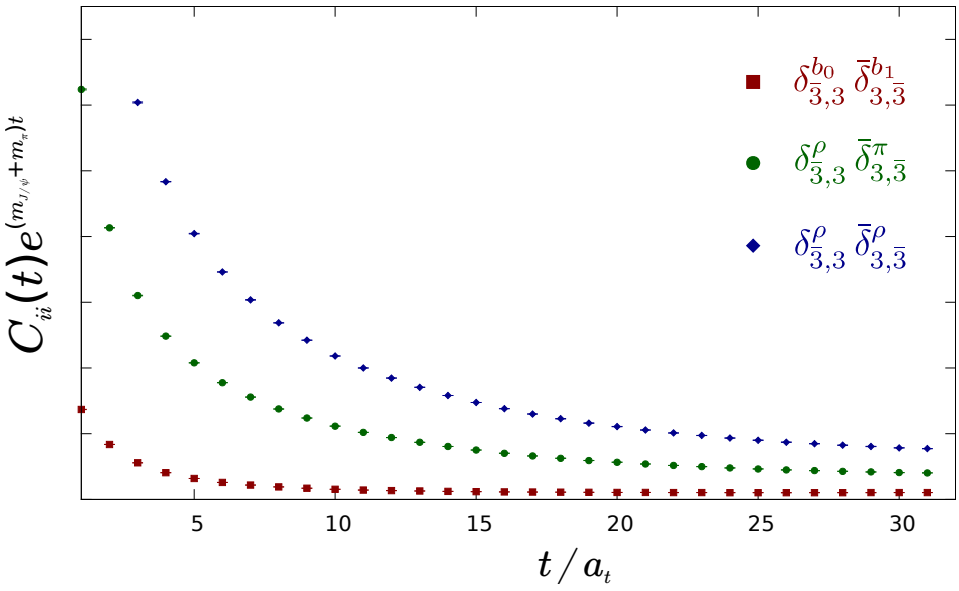

Figure 4.2: $C_{ii}(t)e^{(m_{J/\psi}+m_\pi)t}$ in arbitrary units for the tetraquark operators given in the legend in the $\Lambda^{PG} = T_1^{++}$ isospin-1 hidden-charm channel. Error bars are smaller than the points.

component. The meson-meson and tetraquark operators used in the calculation are given in Table B.1 of Appendix B.

The diagonal elements of the matrix of correlators for the three tetraquark operators in the $\Lambda^{PG} = T_1^{++}$ channel are shown in Figure 4.2. The elements are shown with the exponential time dependence of the J/ψ and the π divided and this shows a plateau in time. The computed signals are seen to be clean, precise and statistically non-zero. Effective masses extracted from these correlation functions are found to be in good agreement with the ground state energy extracted using the variational method later. Figure 4.3 shows the two-point correlator matrix on timeslice 3. This shows that some of the off-diagonal elements between tetraquark and meson-meson operators are non-zero.

After solving the generalised eigenvalue problem of the two-point correlation matrix, the resulting principal correlators for the lowest six energy levels are shown by the points in the leftmost plots in Figure 4.4. The solid curves give the fit to Equation (2.34), with $\chi^2/N_{\text{d.o.f.}} \sim 1$, and the resulting energy levels are shown by the boxes in the central plot

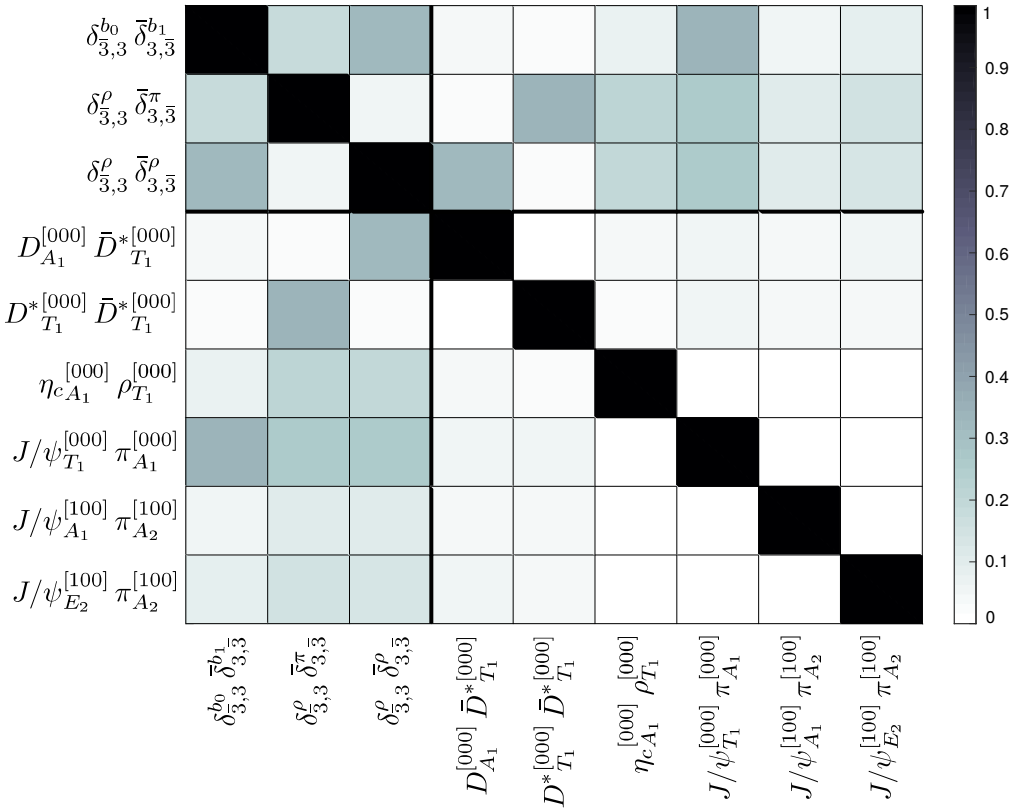

Figure 4.3: Normalised magnitude of elements in the matrix of two-point correlation functions, $|C_{ij}|/\sqrt{C_{ii}C_{jj}}$, on timeslice 3 in the $\Lambda^{PG} = T_1^{++}$ isospin-1 hidden-charm channel. The first three operators are tetraquark operators and the remaining are meson-meson operators ordered as in Table B.1.

with the vertical size of the box representing the one-sigma statistical uncertainty on either side of the mean. The non-interacting meson-meson energy levels are given by the horizontal lines with an adjacent number indicating the degeneracy if it is larger than one. As explained earlier in Section 4.1, these degeneracies can arise when the mesons have non-zero spin. It is observed that the number of energy levels in the extracted spectrum is equal to the number of non-interacting meson-meson levels in the energy region considered and all the computed levels lie close to the non-interacting levels. An important feature to point out is that the higher non-interacting $J/\psi\pi$ level has multiplicity two and I was able to extract the correct number of energy levels associated

with this level since the operator basis contained the relevant meson-meson operators.

Normalised operator-state overlaps are also shown at the bottom of the figure and it can be seen that every energy level has a dominant overlap onto one meson-meson operator type. The energy levels have been coloured by their dominant overlap although it should be emphasised that this is merely a visual aid to compare with the non-interacting levels. It is interesting to see that the third and fourth levels have dominant overlap onto the two linearly-independent $J/\psi\pi$ operators which is not surprising since two degenerate non-interacting levels are expected in this energy region. It is not possible to draw quantitative conclusions about the tetraquark operator overlaps because the absolute normalisations are somewhat arbitrary and renormalisation factors would be needed to relate the overlaps to physical quantities. The only observation that can be made is that most states have some overlap onto one or more tetraquark operators.

To assess the effects of including the tetraquark operators in the operator basis, Figure 4.5 (left panel) shows the $\Lambda^{PG} = T_1^{++}$ spectrum calculated with the full basis of meson-meson and tetraquark operators, with *only meson-meson operators* and with *only tetraquark operators* respectively. No significant deviations are observed between the spectrum computed using the full basis and that computed using the basis of only meson-meson operators which suggests that tetraquark operators are not required to reliably compute the spectrum in this energy region. If only tetraquark operators are used, some poorly determined energy levels are found but it can be seen that the full spectrum is not reliably extracted and this suggests that although the tetraquark operators have some overlap onto the states, they alone do not constitute a sufficient basis of operators.

The spectrum suggests that there are only weak hadron-hadron interactions as the energy levels lie close to the non-interacting levels. From previous studies [94], when a narrow resonance or bound state is present in elastic scattering, an 'extra' finite-volume energy level is observed in that energy region but no evidence for such an extra level is seen in this spectrum, and the number of levels is equal to the number of non-

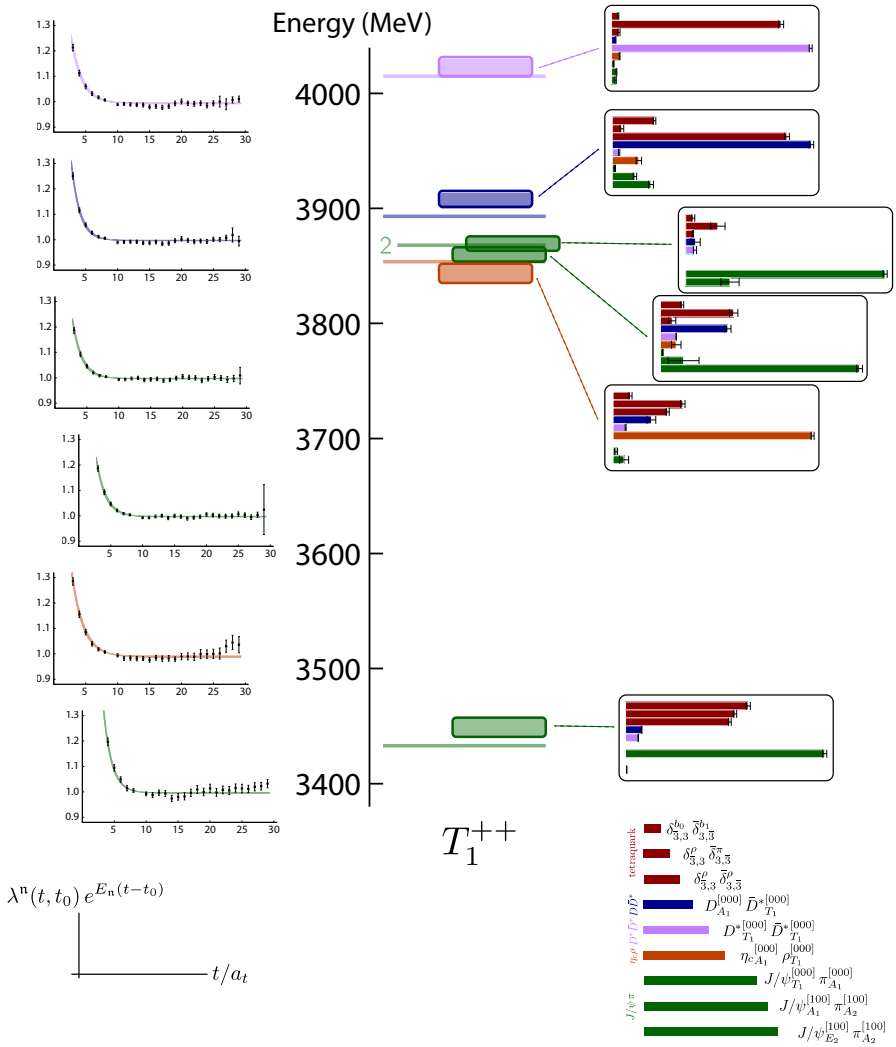

Figure 4.4: The central plot shows the spectrum in the hidden-charm isospin-1 $\Lambda^{PG} = T_1^{++}$ channel using the basis of meson-meson and tetraquark operators in Table B.1. Boxes give the energies with the vertical extent representing the one-sigma statistical uncertainty on either side of the mean and, as a visual aid, are coloured according to their dominant meson-meson operator overlap. Horizontal lines denote non-interacting meson-meson energies with an adjacent number indicating the degeneracy if it is larger than one. The corresponding principal correlators are shown on the left ordered by increasing energy from bottom to top: data (points) and fits (curves) for $t_0 = 9$ are plotted as $\lambda^{\mathfrak{n}}(t,t_0)e^{E_{\mathfrak{n}}(t-t_0)}$ showing the central values and one sigma statistical uncertainties. Histograms on the right show operator-state overlaps for each energy level. The operators are given in the legend and the overlaps are normalised as in Figure 3.3.

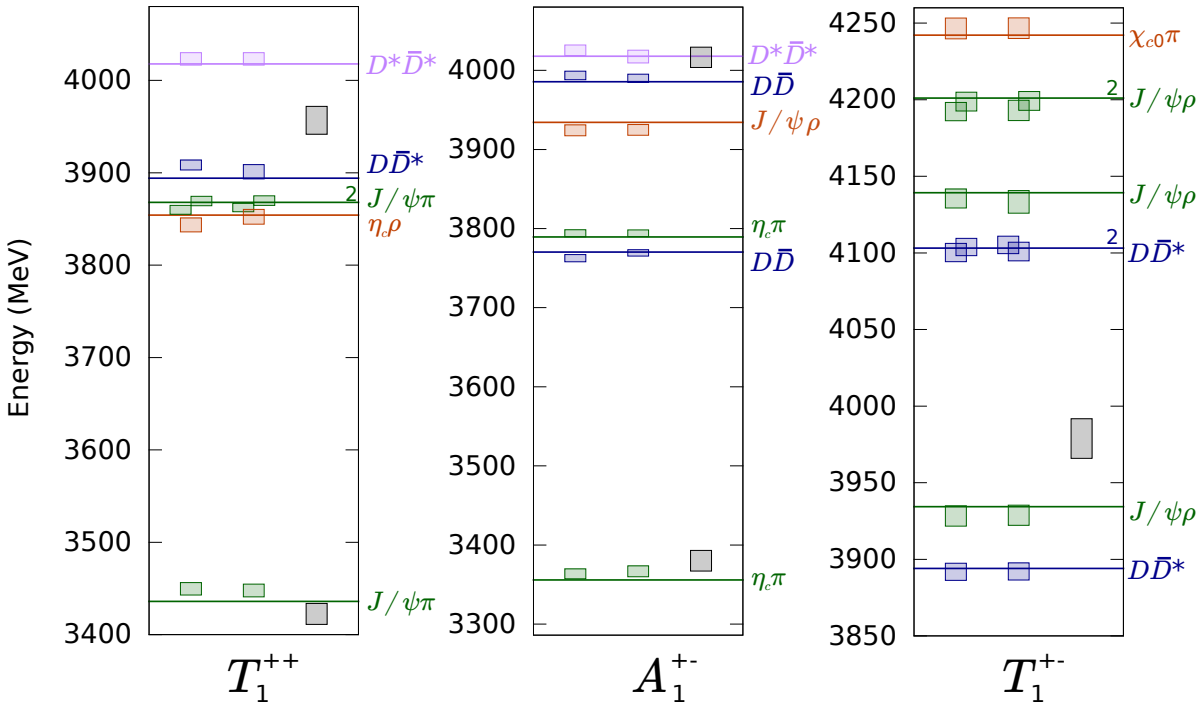

Figure 4.5: As in the spectrum plot of Figure 4.4 but showing the spectra for the isospin-1 hidden-charm sector with $\Lambda^{PG} = T_1^{++}, A_1^{+-}, T_1^{+-}$. Within each plot, the left, middle and right column shows the spectrum determined using the full basis of meson-meson and tetraquark operators, only meson-meson operators and only tetraquark operators respectively.

interacting energy levels. Overall, this gives no indications for a bound state or narrow resonance in this channel. However, this discussion is not directly applicable when considering coupled-channel scattering or broad resonances, for example in Refs. [97, 98]. To draw stronger conclusions and determine if there are bound states or resonances, a Lüscher analysis is necessary to obtain the scattering amplitudes from the finite-volume spectrum. This would require calculations at non-zero momentum and/or different volumes which is beyond the scope of this study. An important conclusion is that the addition of a class of operators resembling compact tetraquarks has little consequence on the finite-volume spectrum and, in turn, the scattering amplitudes.

Moving to other channels in the isospin-1 hidden charm sector, extracted spectra for the $\Lambda^{PG} = A_1^{+-}$ and T_1^{+-} irreps are shown in Figure 4.5 in the middle and right panels respectively. The lowest spin in each of these irreps is respectively $J^{PG} = 0^{+-}$ and 1^{+-}. In general, a similar pattern of features is seen as was found for $\Lambda^{PG} = T_1^{++}$: there are no significant deviations between the spectra calculated using the full basis and only meson-meson operators, the spectrum is not reliably determined if only tetraquark operators are used, and for the full basis, the number of energy levels is equal to the expected number of non-interacting meson-meson levels and they lie close to the non-interacting levels. Furthermore, the operator-state overlaps are found to follow the same qualitative pattern as shown in Figure 4.4. From this, similar conclusions can be made in these channels that the meson-meson interactions are weak and that there are no clear signs of a bound state or narrow resonance.

4.6 Doubly-charmed spectra

Turning to the doubly-charmed sector, Figure 4.6 shows spectra with quark content $cc\overline{ll}$ in the $\Lambda^P = T_1^+, E^+$ and T_2^+ isospin-0 channels where the lowest spin $J^P = 1^+$ appears in T_1^+ and the lowest spin $J^P = 2^+$ subduces in E^+ and T_2^+. Figure 4.7 shows spectra with quark content $cc\bar{l}\bar{s}$ with isospin-1/2 in the irreps $\Lambda^P = A_1^+$ and T_1^+. The operators used to compute the spectra are given in Table B.2 of Appendix B. Similar conclusions can be made as the ones in the hidden charm sector: there are no significant deviations between the spectra including and excluding tetraquark operators, and the spectra can not be reliably extracted using only tetraquark operators. Using the full basis of operators, the number of energy levels in each spectrum is equal to the number of expected non-interacting meson-meson energy levels in the relevant energy region. For most of the energy levels, they lie close to the non-interacting meson-meson energy levels. Because the basis of operators used was sufficiently diverse, I am able to extract many nearly-degenerate energy levels when the meson-meson levels have multiplicity greater than one. Each energy level is found to have a dominant meson-meson operator

overlap. Another conclusion is that the addition of a class of operators resembling compact tetraquarks does not significantly alter the extracted finite-volume spectra

As the flavour of this sector is manifestly exotic and must contain at least four quarks, there are no quark-antiquark states in these channels which makes it particularly suitable to search for compact tetraquark states. In the isospin-0 $J^P = 0^+, 2^+$ channels, the DD and D^*D^* levels are forbidden in S-wave due to Bose symmetry since the flavour wavefunction is antisymmetric in isospin-0 whilst the spin and spatial wavefunctions are symmetric giving an overall antisymmetric wavefunction. These channels are appealing to look for a tetraquark since the low-lying meson-meson states are forbidden. If a low-lying state is found far below the allowed non-interacting meson-meson energy levels, there would be little doubt on it having a compact tetraquark structure. A $J^P = 0^+$ tetraquark would appear in the $\Lambda^P = A_1^+$ irrep and, although a plot is not shown, I calculated the spectrum in this channel with the operators given in Table B.2 and did not find any energy levels below the first allowed non-interacting meson-meson energy level, $DD(2S)$, where $D(2S)$ is the first radial excitation of the pseudoscalar in the charm-light sector and $M_{D(2S)} \approx 2600$ MeV [93]. For a $J^P = 2^+$ state, the breaking of rotational symmetry can be exploited here, with the $J^P = 2^+$ irrep subducing into the two lattice irreps $\Lambda^P = E^+, T_2^+$, by noticing that a meson-meson state subduces differently into the lattice irreps depending on the momentum and lattice irrep combinations of the meson-mesons. This can be seen in Figure 4.7 where the E^+ and T_2^+ irreps contain different non-interacting meson-meson levels. On the other hand, a compact $J^P = 2^+$ state would subduce into both of the irreps $\Lambda^P = E^+, T_2^+$ and the energy levels would appear in both channels. Unfortunately, no such energy levels appearing in both irreps are seen in the figure.

One difference from the hidden charm sector is seen in the $\Lambda^P = T_1^+$ channels in Figures 4.6 and 4.7. In the isospin-0 channel, the non-interacting DD^* and D^*D^* levels can have have degeneracy two. I have reliably extracted two energy levels (the third and fourth) that are found to have dominant overlap onto the two relevant DD^*

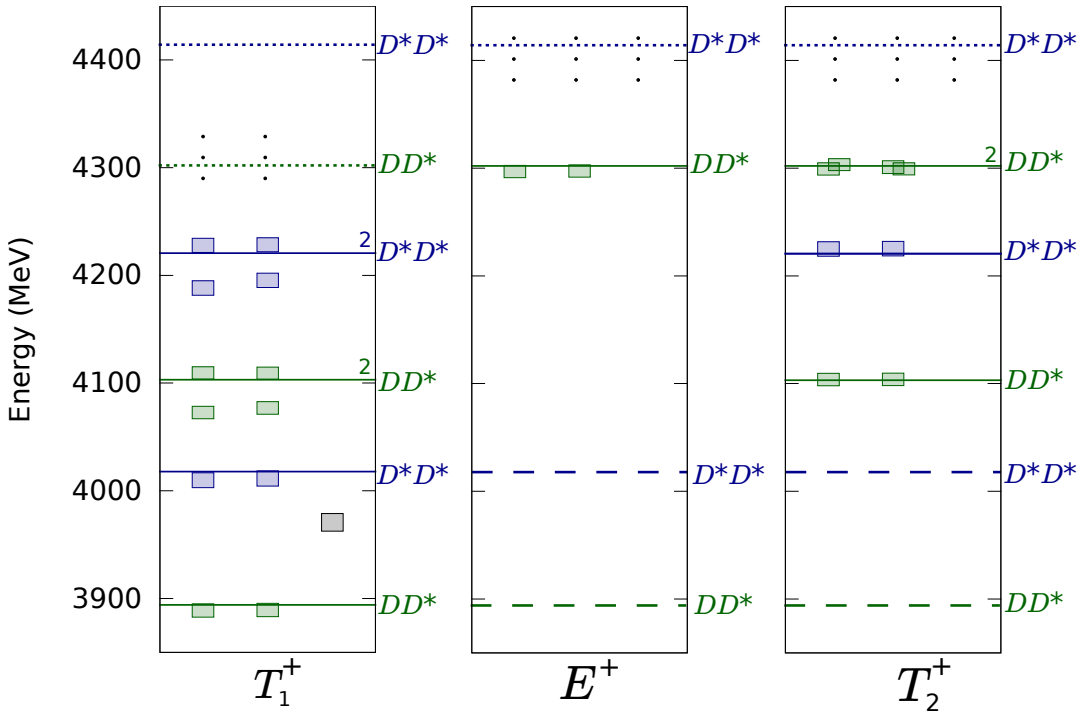

Figure 4.6: As Figure 4.5 but for the isospin-0 doubly-charmed sector with quark flavour $cc\bar{l}\bar{l}$. Dashed lines indicate kinematic thresholds where a non-interacting level is not expected. Dotted lines indicate non-interacting meson-meson levels where the corresponding operators have not been included in the operator basis. Ellipses indicate that additional energy levels have been extracted in/above these regions but they are not plotted as the relevant meson-meson operators have not been included in these energy regions.

operators, and two energy levels (fifth and sixth) that have dominant overlap onto the two corresponding D^*D^* operators. It can be seen that each pair of energy levels is non-degenerate and shifted away from the non-interacting levels. The presence of an energy level below the non-interacting level suggests that there could be an attractive interaction. In order to rigorously quantify this statement, a scattering analysis is needed to relate the finite-volume spectrum to the scattering amplitudes via the Lüscher formalism. As seen in the later chapters, a robust constraint of the scattering amplitudes

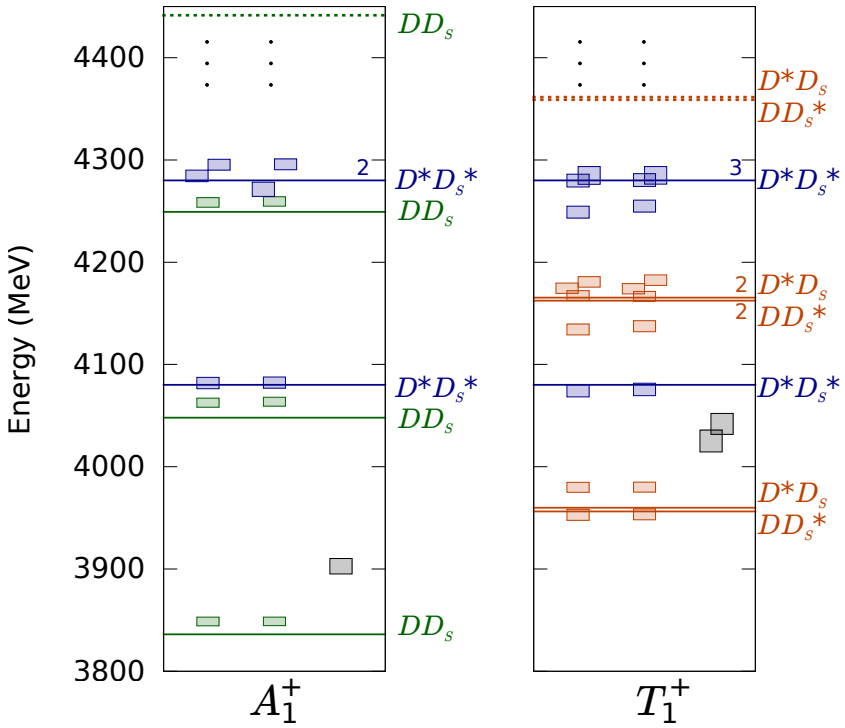

Figure 4.7: As Figure 4.6 but for the isospin-$\frac{1}{2}$ doubly-charmed sector with quark flavour $cc\bar{l}\bar{s}$.

is made from a large number of energy levels which can possibly be obtained in different volumes and overall non-zero momentum. There are not enough energy levels obtained in this calculation to reliably utilise the Lüscher formalism and further finite-volume spectrum calculations are beyond the scope of the study but it would be desirable to calculate this in the future. It is important to stress though that a reliable determination of the coupled S and D-wave scattering amplitudes can only be performed when all these multiple energy levels are robustly extracted. For the isospin-1/2 channel, similar conclusions can be made.

4.7 Systematics and stability of the extracted spectra

Before discussing and interpreting the results further, I consider some systematic effects on the finite-volume spectra and present some tests of varying the operator basis and the number of distillation vectors.

4.7.1 Systematic uncertainties on the spectra

As a first application of these tetraquark operator constructions, the calculations were performed on a relatively small lattice volume, $L \sim 2$ fm, and there is a possibility that this is too small to distinguish the spatial structures of the extended meson-meson and compact tetraquark. To illustrate this statement more concretely, the tetraquark operator can be Fierz rearranged as a product of meson-meson operators. Consider a simple tetraquark operator in the continuum in finite volume V,

$$\mathcal{T}(x) = n_T(\delta_{bd}\delta_{ce} \mp \delta_{be}\delta_{cd}) \left[c^{b\alpha}(x) P^{\alpha\beta} q^{c\beta}(x)\right] \left[\bar{c}^{d\gamma}(x) Q^{\gamma\delta} \bar{q}^{e\delta}(x)\right], \tag{4.13}$$

where Latin indices are for colour and Greek indices denote spin. The Kronecker deltas give the combined $\mathrm{SU}(3)_C$ Clebsch-Gordan coefficients for $(\underline{3}\otimes\underline{3})\otimes(\bar{\underline{3}}\otimes\bar{\underline{3}}) \to \underline{1}$ via either $\bar{\underline{3}}\otimes\underline{3}$ (minus) or $\underline{6}\otimes\bar{\underline{6}}$ (plus). n_T is a normalisation constant that is either $1/\sqrt{12}$ (minus) or $1/\sqrt{24}$ (plus). P and Q are shorthand for the products of the charge conjugation matrix and Dirac gamma matrix within the diquark and antidiquark. Expanding out the colour coupling gives

$$\mathcal{T}(x) = n_T P^{\alpha\beta} Q^{\gamma\delta} \left[-(\bar{c}^{\gamma} c^{\alpha})(\bar{q}^{\delta} q^{\beta}) \mp (\bar{c}^{\gamma} q^{\beta})(\bar{q}^{\delta} c^{\alpha})\right], \tag{4.14}$$

where the colour and spatial indices are now suppressed. A Fierz rearrangement of the spin indices can be applied to rewrite $P^{\alpha\beta}Q^{\gamma\delta} = R^{\gamma\alpha}S^{\delta\beta}$ or $U^{\gamma\beta}V^{\delta\alpha}$ where these new matrices are given by a linear combination of a basis of Dirac gamma matrices Γ_I, i.e. $R = \sum_I R_I\Gamma_I$, $S = \sum_I S_I\Gamma_I$, etc. Therefore, this tetraquark operator can be

rewritten as

$$\mathcal{T}(x) = n_T \left[-(\bar{c}Rc)(\bar{q}Sq) \mp (\bar{c}Uq)(\bar{q}Vc)\right], \tag{4.15}$$

where spin indices have been suppressed. Combining the matrices into one Fierz coefficient gives, $P^{\alpha\beta}Q^{\gamma\delta} = \sum R_I \Gamma_I^{\gamma\alpha} S_J \Gamma_J^{\delta\beta} = \sum F_{IJ} \Gamma_I^{\gamma\alpha} \Gamma_J^{\delta\beta}$. The Fierz coefficients, F_{IJ}, can be projected out with the orthogonality relation $\mathrm{Tr}(\Gamma_I \Gamma_J) = 4\delta_{IJ}$ to give $F_{IJ} = \frac{1}{16}\mathrm{Tr}(\Gamma_I Q \Gamma_J^T P^T)$. A similar arrangement can be made for the UV term. From this example, it is straightforward to see that any tetraquark operator can generally be written in terms of a basis of two-meson operators for some Fierz coefficients, F_{IJ}, as

$$\mathcal{T}(x) = n_T \sum_{I,J} F_{IJ} M_I(x) M_J(x). \tag{4.16}$$

Projecting the tetraquark operator onto definite momentum p,

$$\mathcal{T}(p) = n_T \sum_{I,J} F_{IJ} \int d^3x \; e^{ipx} M_I(x) M_J(x), \tag{4.17}$$

and writing the mesons in momentum space gives

$$\mathcal{T}(p) = n_T \sum_{I,J} F_{IJ} \int d^3x \; e^{ipx} \frac{1}{V} \sum_k e^{-ikx} M_I(k) \frac{1}{V} \sum_l e^{-ilx} M_J(l). \tag{4.18}$$

As a reminder, this operator is considered in finite volume V and the continuum. Performing the integral gives a Kronecker delta and after the summation,

$$\mathcal{T}(p) = \frac{1}{V} n_T \sum_{I,J} F_{IJ} \sum_k M_I(k) M_J(p-k). \tag{4.19}$$

Suppose then that a meson-meson operator with the form

$$\mathcal{O}(p) = \sum_k M_1(k) M_2(p-k). \tag{4.20}$$

has overlap value, Z, onto a meson-meson state $|M_1(k)M_2(p-k)\rangle$. In the non-interacting limit, the overlap of a tetraquark operator onto this meson-meson state is $n_T F_{12} Z/V$ which is mainly suppressed by the volume. This suggests that if the volume is not big enough, there is no way to distinguish the two different structures and the operators

are not completely linearly independent and sufficiently diverse. Figure 4.3 does show the off-diagonal element between the tetraquark and meson-meson operators is non-zero which could give an indication that there is not a large volume suppression. This discussion shows the importance on the volume dependence and further calculations would be required to give some better indication on how the results vary with the volume but this is beyond the scope of the study.

Another systematic effect could arise from calculating with unphysically heavy light quarks, corresponding to $M_\pi = 391$ MeV, and the presence of tetraquarks or molecules could depend on this. It was concluded from the results in this study that there may not be a bound state or narrow resonance in the scattering amplitudes but it is interesting to ask how varying the light quark mass could change this conclusion. If a pole does exist in the scattering amplitudes, changing the quark mass parameter continuously would merely change the position of the pole within the complex plane. Such movement of poles in the complex plane as the light quark mass is reduced has been observed in other lattice QCD calculations [75, 98]. Ultimately, calculations with light-quark masses close to their physical values are necessary to compare with experiment and from another perspective, studying how the spectra change as the quark masses are varied would give insight into the relevant QCD interactions and could be compared with expectations in different models.

Other systematic effects have been discussed in previous sections such as finite L/T and discretisation effects but these are expected to be small.

4.7.2 Varying the operator basis

There have already been some tests of varying the operator basis in this chapter. Comparisons were made between the spectra using the full basis of meson-meson operators and tetraquark operators and using only meson-meson operators, and it was found that there were no significant changes between the two. Additionally, the full finite-volume spectra could not be extracted if only tetraquark operators were used.

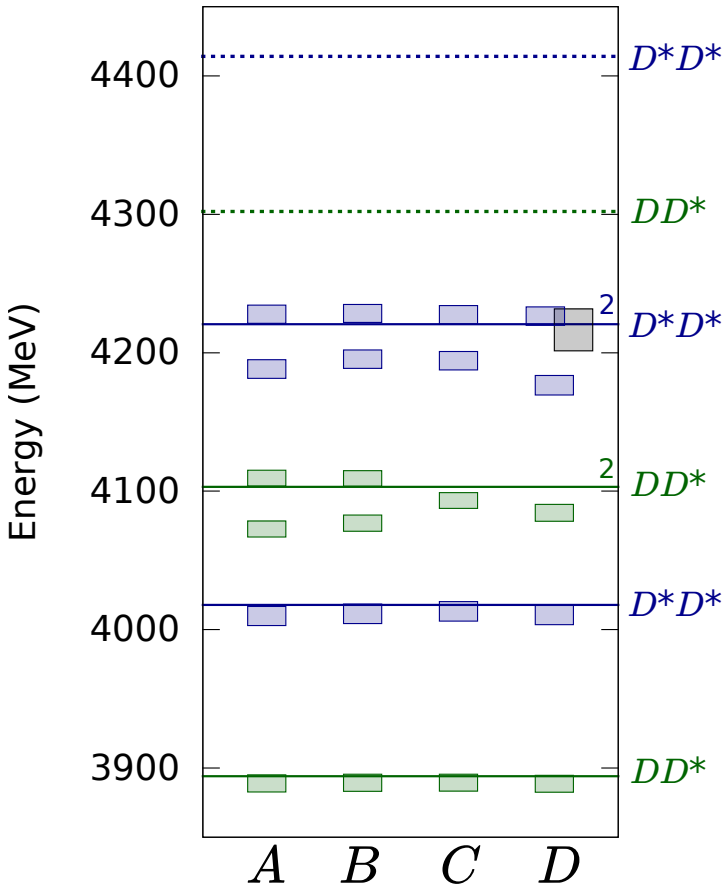

Figure 4.8: As Figure 4.6 but for the $\Lambda^P = T_1^+$ isospin-0 $cc\overline{l}\overline{l}$ channel with different bases of operators: A uses the full basis of meson-meson and tetraquark operators, B uses only meson-meson operators, C uses only meson-meson operators minus one DD^* operator as described in the text, and D uses the operators as in C supplemented with the tetraquark operators.

To illustrate what could happen if a sufficiently diverse set of meson-meson operators is not used, Figure 4.8 shows spectra in the isospin-0 doubly-charmed $\Lambda^P = T_1^+$ channel computed with different operators bases. The meson-meson energy levels can have degeneracies in the non-interacting limit as explained earlier due to the multiple partial waves. Column A shows the previous spectrum computed using the full basis of meson-meson and tetraquark operators and the number of energy levels is equal to

the number of expected non-interacting meson-meson energy levels in the energy region of interest. In column B, only meson-meson operators are used to calculate the spectrum and the same conclusion can be made. Column C shows the spectrum using only meson-meson operators without the $D^{[100]}_{A_2} D^{*[100]}_{E_2}$ operator which is relevant for the non-interacting DD^* level near 4100 MeV. It can be seen that there is one less energy level and the second DD^* level moves somewhere in between which is a behaviour that can occur when there are not enough linearly-dependent operators in the operator basis to reliably extract the complete spectrum [94]. This test shows the clear necessity to ensure the operator basis is sufficiently diverse to extract the spectrum and it is obvious that an attempt to determine the scattering amplitudes from the incomplete spectrum would incorrect. Another reason for requiring an appropriate operator basis can be seen in column D which shows the spectrum calculated with the operators as in column C with the tetraquark operators included – an additional energy level is found compared to column C in the energy region considered. This demonstrates the necessity of accounting for all the relevant meson-meson energy levels in the energy region of interest as otherwise, there is a danger that this level could be mistakenly interpreted as a signal for the presence of a compact tetraquark state.

4.7.3 Varying the number of distillation eigenvectors

If the number of distillation eigenvectors used for the tetraquark operators is too small, the operator may not be able to efficiently interpolate states of interest as it may be too smeared and no longer resemble a compact tetraquark. However, since the computational cost involving tetraquark operators scales much more strongly than meson-meson operators with the number of distillation eigenvectors, this number can not be too large if the calculations are to be practically feasible. I present a systematic test of varying the number of distillation eigenvectors.

The spectrum in the isospin-0 doubly-charmed $\Lambda^P = T_1^+$ channel is shown in Figure 4.9 using different numbers of distillation vectors for tetraquark operators, $\tilde{N}_{\text{vecs}} = 16, 24, 32,$

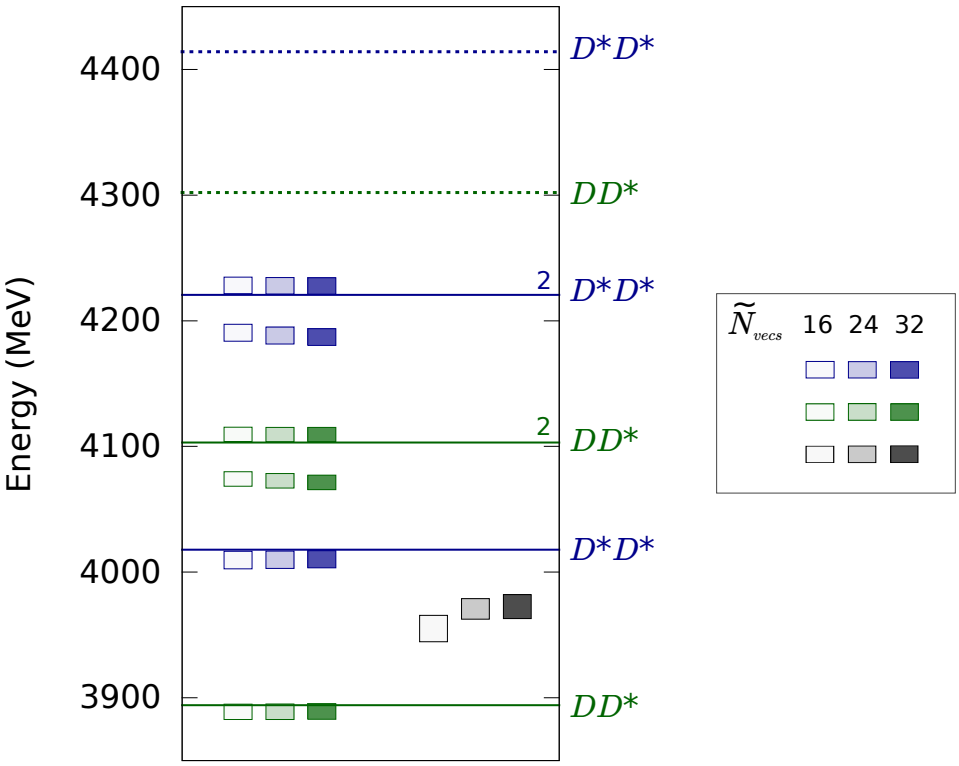

Figure 4.9: As Figure 4.6 but showing the $\Lambda^P = T_1^+$ isospin-0 $cc\overline{l}\overline{l}$ spectrum calculated using tetraquark operators with different numbers of distillation vectors, $\tilde{N}_{\text{vecs}} = 16, 24, 32$. The leftmost columns use the full basis of meson-meson and tetraquark operators, and the rightmost columns use only tetraquark operators.

with the full basis of meson-meson and tetraquark operators, and only tetraquark operators. It can be seen that the results are not highly sensitive to the number of distillation eigenvectors. In addition to this test, I also computed the spectra from all the previous channels using a smaller number of eigenvectors for the meson-meson operators, i.e. $N_{\text{vecs}} = \tilde{N}_{\text{vecs}} = 24$. The results were found to be consistent with the spectra shown in the previous sections. Overall, these tests suggest that the results are not highly dependent on the number of distillation eigenvectors. It has been shown in Ref. [109] that a small number of distillation vectors is sufficient to extract finite-volume spectra provided one does not consider higher momenta, higher spin, or highly excited states.

Because the channels are at zero momentum and the study is focused on relatively low-lying states, this further supports the conclusions made here.

4.8 Discussion and comparisons with other studies

I will now discuss the results in the context of expectations from phenomological models and observations from experiment, and compare with previous lattice calculations. In Appendix A, I describe a simple one-gluon exchange model of a diquark where the two quarks interact via a colour-colour spin-spin interaction and show that the most attractive diquark and anti-diquark configurations have (colour irrep,spin) = $(\underline{\bar{3}}, 0)$ and $(\underline{3}, 0)$ respectively. Therefore, the most favourable tetraquark that can form has $J^P = 0^+$ and on the lattice, this state would subduce into $\Lambda^P = A_1^+$. Additionally, the spin-spin interaction is suppressed by the quark mass and so, some models expect spin-1 diquark configurations with heavy quarks to form and, combining with the spin-0 diquarks, produce a tetraquark multiplet [110]. The lightest multiplet in S-wave contains tetraquarks with $J^P = (0, 1, 2)^+$ with $J^P = 1^+$ subducing into $\Lambda^P = T_1^+$ and $J^P = 2^+$ subducing into the E^+, T_2^+ irreps. Besides the mass of the quarks, this one-gluon exchange model interaction does not depend on the flavours of the quarks. However, when the flavour irreps of the two quarks (antiquarks) are identical, Fermi symmetry requires the overall diquark (anti-diquark) configurations to be antisymmetric and this restricts the allowed combinations.

In the isospin-1 hidden charm sector, the flavour irreps of the individual quarks (antiquarks) in the diquarks (anti-diquarks) are distinct and therefore, no extra constraints from Fermi symmetry are imposed on the allowed configurations. Diquark–anti-diquark models [110, 111], that attempt to explain the $X(3872)$ and the charged Z states, suggest that the lightest tetraquark multiplet has $J^{PG} = 0^{+-}, 1^{++}, 1^{+-}, 2^{+-}$ and I have performed a thorough investigation in all these channels except for $J^{PG} = 2^{+-}$. In the $\Lambda^{PG} = A_1^{+-}$ channel which contains $J^{PG} = 0^{+-}$, expected to be the most attractive, and the $\Lambda^{PG} = T_1^{++}$ and T_1^{+-} channels, which contain $J^{PG} = 1^{++}$ and 1^{+-} respectively,

there are no hints of a bound state or narrow resonance in the extracted spectra, let alone significantly attractive meson-meson interactions.

Comparing with experiment, there is currently no state with $J^{PG} = 0^{+-}$, nor is there any charged charmonium-like candidate with undetermined J^{PG} that is light enough to be identified as the lowest-lying $J^{PG} = 0^{+-}$ tetraquark. The charged $Z_c(3900)$ has been observed with $J^{PG} = 1^{++}$ [15] and is a suitable candidate for a tetraquark but I do not see signs of such a narrow resonance in the computed $\Lambda^{PG} = T_1^{++}$ spectrum. One plausible way to reconcile this is to explain $Z_c(3900)$ as a threshold cusp where it does not originate dynamically from QCD as a pole in the scattering amplitude but instead, the cross section is enhanced due to kinematic effects from the opening of thresholds [25]. Further investigation on this conclusion is beyond the scope of the study but it is interesting to note that a candidate $Z_c(3900)$ has also not been seen in similar lattice QCD calculations which also extracted the finite-volume spectrum with meson-meson and tetraquark operators [101] and other finite-volume spectrum calculations with meson-meson operators [112, 113, 114] although none of these have included all the relevant meson-meson operators like the work here. There is currently no experimental candidate confirmed to have $J^{PG} = 1^{+-}$ but the analogous isospin-1 partner of the $X(3872)$ would appear in this channel. No signals for such a tetraquark state was found in the $\Lambda^{PG} = T_1^{+-}$ channel and this agrees with a previous lattice QCD calculation [103]. However, not all of the energy levels in this study were extracted due to not using a sufficiently diverse set of operators. However, as isospin breaking may be important for the $X(3872)$, simulations with $N_f = 1+1+1$ flavours and electrodynamics would be necessary but these calculations are difficult.

Moving to the doubly-charmed sector, possible diquark configurations are further constrained by Fermi symmetry compared to the hidden charm sector. The $(\bar{3}, 0)$ and $(6, 1)$ cc diquarks are forbidden as they are symmetric under the interchange of quarks and only the $(\bar{3}, 1)$ and $(6, 0)$ diquarks are allowed. In the one-gluon exchange model, the interaction is repulsive for these allowed cc configurations and is least repulsive for

$(\bar{\underline{3}}, 1)$ However, the repulsion is suppressed by the mass of the charm quark such that doubly-charmed tetraquarks may be allowed. The most attractive $(\underline{3}, 0)$ $\bar{q}\bar{q}$ anti-diquark configurations are required to be antisymmetric in flavour belonging in $F = \underline{3}$ and have isospin $I = 0$. Therefore, combining the $(\bar{\underline{3}}, 1)$ cc diquark with the $(\underline{3}, 0)$ $\bar{q}\bar{q}$ anti-diquark gives the most favourable tetraquark with quantum numbers $(I)J^P = (0)1^+$. Other attractive configurations include $(I)J^P = (0)0^+$, $(0)2^+$ containing a $(\bar{\underline{6}}, 1)$ anti-diquark, and $(I)J^P = (\frac{1}{2})0^+, (\frac{1}{2})1^+$ from picking the $I = \frac{1}{2}$ components of the $(\underline{3}, 0)$ anti-diquark. However, no signs of these tetraquarks are seen in any of the computed spectra in the wide range of doubly-charmed channels. The lack of significant deviations found between the spectra including and excluding tetraquark operators is consistent with the results presented in Ref. [102] which computed the spectrum in the $(I)J^P = (0)1^+$ channel. That study used meson-meson and tetraquark operators but, because the operator basis was more restricted than the one in this chapter, they were unable to extract all of the multiple levels which correspond to degenerate meson-meson levels in the non-interacting limit. Computations presented in Ref. [115] find an attractive interaction in the $(I)J^P = (0)1^+$ channel using a less direct approach in which lattice QCD computations are used to extract a potential which is then used to determine scattering amplitudes. They do not find a bound state or resonance for a range of light quark masses corresponding to $M_\pi = 410 - 700$ MeV and conclude that this attractive interaction gets stronger with decreasing pion mass, motivating studies of how the results vary as the light quark mass decreases towards the physical point.

In one-gluon exchange models, the colour-colour spin-spin interaction is always repulsive for the cc diquark, but the repulsion is suppressed by the quark mass which suggests that doubly-bottomed tetraquarks may be more favourable than doubly-charmed tetraquarks. This is supported by lattice QCD calculations of finite volume-spectra using bases of meson-meson and tetraquark-like operators which suggest the existence of a $(I)J^P = (0)1^+$ doubly-bottomed tetraquark [116]. Further support comes from lattice calculations of the potential between two static bottom quarks in the presence

of two light antiquarks [117, 118, 119, 120, 121]. This potential is found to lead to a bound state with $(I)J^P = (0)1^+$. My computed doubly-charmed $(I)\Lambda^P = (0)T_1^+$ spectrum is not inconsistent with there being an attractive interaction although there were no obvious signs of a bound state in this channel. This is also consistent with recent phenomological studies [122, 123, 124] which suggest the doubly-bottom tetraquark is bound and the doubly-charmed tetraquark is unbound. Further calculations using bottom quarks and a Lüscher analysis would highly be of interest. Computations involving the bottom quark with the Clover fermion action used here are not straightforward since $a_t m_b$ is not small leading to large discretisation effects. One possibility is to calculate bottom quark perambulators in future studies with alternative fermion actions such as Non-Relativistic QCD [125] or the Fermilab approach [126].

Overall, this study has improved on previous lattice QCD investigations of tetraquarks in two ways. The first is that a diverse set of tetraquark and meson-meson operators are used to calculate the finite-volume spectrum such that a large number of energy levels could be extracted reliably. For the first time in a lattice QCD calculation, the multiple energy levels associated with meson-meson energy levels which would be degenerate in the non-interacting limit were robustly extracted. The second way is that spectra across a wide range of channels were able to be studied due to the construction of a very general class of tetraquark operators that can be applied to any channel. A generic feature of tetraquark models is that they predict the formation of a large multiplet of states across many different quantum numbers and some of the channels that I studied have never been calculated before. One important conclusion of this work was that the tetraquark operators did not have a significant effect on extracting the finite-volume spectrum. This suggests that a basis of meson-meson operators is reliable to extract spectrum with multiquark states. With this in mind, I will describe in the next chapter an explicit calculation of finite-volume spectrum using single-meson and meson-meson operators in the open-charm sector and use it to determine the scattering amplitudes using the Lüscher method.

Chapter 5

DK Scattering

I will now spend the remainder of this thesis discussing scattering calculations, using the Lüscher formalism to relate the finite-volume spectrum to the scattering amplitudes, having established the necessary techniques to extract finite-volume spectrum. One particularly interesting amplitude is the isospin-0 $DK \to DK$ amplitude which is relevant for the experimental $D_{s0}^*(2317)$ [127] in the isospin-0 charm-strange $J^P = 0^+$ sector. This channel is interesting because quark model predictions [11, 14] expect a broad resonance above the isospin-0 DK threshold but experiment finds this state to be narrow and below the threshold. It is even more puzzling given that this state is expected to be heavier than the corresponding charm-light state, $D_0^*(2400)$ [128], since the strange quark is heavier than the light quarks. In contrast, the $D_0^*(2400)$ is in agreement with quark model expectations as it is found to be a broad resonance above the analogous $D\pi$ threshold. These peculiarities have led to $D_{s0}^*(2317)$ being considered as a candidate for an exotic meson that does not align with the quark-antiquark picture. Some examples of the interpretations are to explain $D_{s0}^*(2317)$ as a DK molecule, a compact tetraquark, or a conventional quark-antiquark state with coupled channel effects; see Ref. [19] for a comprehensive review. It is interesting also to point out that this is part of a bigger puzzle since similar discrepancies are seen in the $J^P = 1^+$ channel with the observation of the $D_{s1}(2460)$ [129] below the D^*K threshold in disagreement with quark model expectations.

Due to the proximity of the $D_{s0}^*(2317)$ to the DK threshold at roughly 40 MeV away, it is clear that a thorough lattice QCD investigation involving this state should include effects from this threshold. Some recent dynamical lattice QCD calculations of

spectrum in this channel have not included the relevant DK operators to account for this threshold and the mass is generally overestimated in the results [130, 30, 93, 83, 77] whilst calculations to include the effects of the DK threshold find results more in line with experiment [44, 45, 48]. Refs. [44, 45] have limitations from using small volumes and a low number of energy levels to constrain the amplitudes. Ref. [48] is calculated with $N_f = 2$ dynamical quarks and quenched strange quarks and this may have a large systematic effect given that DK contains a strange quark. A more detailed comparison of the results here with these other studies will be presented later. In this chapter, I will improve the studies in this area by calculating numerous energy levels of the finite-volume spectra on a sufficiently big lattice with $N_f = 2 + 1$ dynamical quarks. Using a substantially large basis of operators, many energy levels are obtained at rest and non-rest frames. From this spectra, I constrain elastic isospin-0 DK scattering amplitudes across a large energy region and determine the singularity structure of the scattering amplitudes. Before showing the results, I will give a review on the Lüscher method and the particular implementation that I use to obtain the scattering amplitudes from the finite-volume spectra.

5.1 Scattering theory

To begin the discussion on scattering amplitudes and set conventions, I will give a basic review of scattering theory here for elastic two-body scattering where there is only one channel. Consider the kinematics of two spinless particles with masses m_1, m_2. The energy in the centre-of-momentum (cm) frame where the total 3-momentum of the system is zero is related to the Mandelstam $s = (k_1 + k_2)^2$ by

$$\sqrt{s} = E_{cm} = \sqrt{m_1^2 + \vec{k}^2} + \sqrt{m_2^2 + \vec{k}^2} \tag{5.1}$$

where $\vec{k}$ is the cm momentum. Solving this equation for the magnitude of $\vec{k}$ gives

$$k = \left[\frac{1}{4s} \left(s - (m_1 + m_2)^2 \right) \left(s - (m_1 - m_2)^2 \right) \right]^{1/2}. \tag{5.2}$$

Counting the degrees of freedom of this two-body system in the cm frame, there are eight momentum components but $p_i^2 = m_i^2$ and momentum conservation results in only two degrees of freedom to describe the particles. Usual choices are either E_{cm} and the scattering angle θ of $\vec{k}$ in the plane of scattering or the Lorentz invariant Mandelstam variables s and t.

Scattering is described by the scattering matrix (S-matrix) and can be separated into a trivial part and the Lorentz invariant t-matrix as

$$S = 1 + 2i\rho t \tag{5.3}$$

where $\rho = 2k/E_{cm}$ is the phase space. The t-matrix is related to the invariant two-body scattering amplitude by $\mathcal{M} = 16\pi t$. Above threshold, unitarity of the S-matrix ($SS^\dagger = 1$) from conservation of probability imposes

$$t - t^\dagger = 2i\rho t t^\dagger \tag{5.4}$$

which implies Im $t = \rho t t^\dagger$ and Im $t^{-1} = -\rho$. Since unitarity constrains the imaginary part of the t-matrix, it is sufficient to describe the real part by rearranging the unitarity relation leading to

$$(t^{-1} + i\rho)^\dagger = (t^{-1} + i\rho) \equiv K \tag{5.5}$$

which gives a Hermitian matrix K. As the S-matrix is invariant under time-reversal symmetry, the K-matrix must be a symmetric matrix and is therefore real. This K-matrix will be one convenient way to describe the scattering amplitudes later.

It is convenient to do a partial wave decomposition of the t-matrix, t_l, in partial wave l,

$$t(E_{cm}, \theta) = \sum_l (2l+1) P_l(\cos\theta) t_l(E_{cm}). \tag{5.6}$$

Unitarity allows for t_l to be described in terms of a single real phase shift, $\delta_l(E_{cm})$, in partial wave l that depends on the energy,

$$t_l(E_{cm}) = \frac{1}{\rho} e^{i\delta_l} \sin\delta_l(E_{cm}). \tag{5.7}$$

An alternative way to write t_l in terms of the phase shift is to invert this expression and take the real part to obtain Re $t_l^{-1} = \rho \cot \delta_l$. The unitarity relation constrains the imaginary part to give

$$t_l = \frac{1}{\rho \cot \delta_l - i\rho}. \tag{5.8}$$

To obtain observables from the amplitudes, the cross section for partial wave l is given by

$$\sigma_l = \frac{4\pi}{k^2}(2l+1)\rho^2|t_l|^2 = \frac{4\pi}{k^2}(2l+1)\sin^2\delta_l. \tag{5.9}$$

A naive definition of resonances is to identify them as 'bumps' that appear as a standard Breit-Wigner shape in the cross section. For the elastic case, a peak occurs when $\delta_l(M) = \pi/2$ and M is the mass of the resonance. However, this is not so straightforward for coupled channels or broad resonances which do not appear as simple bumps in the cross section [131]. A more rigorous definition is to identify resonances and bound states as the singularity content of the scattering amplitudes in the complex s plane. The square-root in Equation (5.2) means there is a branch cut beginning at $s = (m_1 + m_2)^2$ that can be chosen to extend to positive infinity which leads to two Riemann sheets. The first sheet has $\mathrm{Im}(k) > 0$ and is known as the *physical* sheet as it contains the real energy axis where physical scattering occurs, $s + i\epsilon$ with ϵ approaching zero for positive values. The second sheet has $\mathrm{Im}(k) < 0$ and is known as the *unphysical* sheet. Close to a pole, the t-matrix has the form

$$t_l(s) \sim \frac{g^2}{s_0 - s} \tag{5.10}$$

where g can be interpreted as the coupling of the pole to the amplitude. Poles above threshold on the real axis are forbidden by the unitarity relation Im $t = \rho|t|^2$. On the physical sheet, causality forbids poles off the real energy axis [132] and therefore, the only poles that are allowed are located on the real axis below threshold and these are identified to be bound states with mass $\sqrt{s_0}$. Poles far below threshold should not significantly affect physical scattering but shallow bound states may be observable in the cross section. On the unphysical sheet, poles off the real axis can appear as complex

conjugate pairs and are identified as resonances with mass and width given respectively by the real and imaginary parts, $\sqrt{s_0} = m \pm i\frac{1}{2}\Gamma$. The pole with negative imaginary part has the larger effect on physical scattering as it lies closer to the real energy axis whereas the other pole has to do a full loop around the unphysical sheet to influence the real axis. It is also easy to see that the width of the resonance determines how far it is from the real axis and narrow resonances will give rise to a larger bump in the cross section around its mass whereas broad resonances further away may not have this simple bump-like structure. This interpretation of bound states and resonances as poles in the scattering amplitudes suggests that they should not be thought of as completely distinct as the only difference is where the position of the pole lies on the two Riemann sheets. In fact, it has been seen in lattice QCD calculations that the pole associated with the ρ meson in isospin-1 P-wave $\pi\pi$ scattering transitions from a bound state to a resonance as the mass of the light quarks is decreased to their physical values [69, 94, 75].

5.2 Scattering in a finite-volume

The desired quantities to calculate are hadronic scattering amplitudes but these cannot be calculated directly in lattice QCD for the following reasons. Firstly, there is no clear definition of an asymptotically free state to construct the S-matrix in a finite-volume. The particles cannot be separated infinitely far apart due to the periodic boundary conditions. Furthermore, the correlation functions calculated in finite-volume give a discrete set of poles along the real energy axis and there is no two sheet structure. This can be seen explicitly in Equation (2.30) when the two-point correlation functions are expressed in energy space and rotated back to Minkowski space. Compare this to the infinite-volume correlation functions in the standard Källén-Lehmann spectral representation which contain a continuous spectrum of multiparticle states beginning at threshold, and any bound states appear as poles below threshold. It is clear that resonances which appear above threshold as poles in the complex plane are not described by the finite-volume correlation functions but on the other hand, this difficulty does

not apply to bound states. The main conclusion from these considerations is that scattering cannot be done in a finite-volume. As lattice QCD is necessarily calculated using finite-volumes, it seems like there is no hope to directly calculate the hadronic scattering amplitudes. The solution to this problem is to find some mapping between the finite-volume physics and the infinite-volume physics in which scattering is well-defined and this mapping will be referred to here as the *Lüscher quantisation condition* after Lüscher's pioneering work on this topic [36, 37, 38, 39].

An illustration of this relation can be made for a simple non-relativistic system where two identical spinless bosons, separated by distance $|x|$, scatter in one-dimension. In the infinite-volume, suppose the interaction is described by a potential $V(|x|)$ with a finite range. Far away from the potential, the outgoing wavefunction asymptotically approaches that of a free two-boson system, $\psi(|x|) \sim \cos(p|x| + \delta(p))$ where $\delta(p)$ is the usual scattering phase-shift that describes the scattering. Computing the phase-shift for a given interaction potential is a textbook exercise by obtaining the wavefunction within the interaction and matching the two wavefunctions at the boundary of the interaction.

Suppose now that this system is placed in a finite-volume of size L which is much larger than the range of the interaction. Applying periodic boundary conditions by matching the asymptotic wavefunction and its derivative at $x = \pm L/2$ gives the quantisation condition

$$p = \frac{2\pi}{L} n - \frac{2}{L}\delta(p) \tag{5.11}$$

where n is an integer. This quantisation condition gives the relationship between the finite-volume spectrum in a box of size L, determined by p, and the infinite-volume scattering information $\delta(p)$. Since n can only take integer values, the finite-volume spectrum here is discrete due to the periodic boundary conditions. If there is no interaction, $\delta(p) = 0$ and the quantisation condition recovers the quantisation of momentum in a finite-volume. It can be seen that a non-zero interaction leads to deviations from the free-particle spectrum. This simple example illustrates that scattering information can be inferred by measuring the differences between the computed finite-volume spectrum

and the energy levels for when there are no interactions.

This is the general idea to find a correspondence between the finite-volume and infinite-volume physics. A Lüscher quantisation condition has been generalised to 3+1 dimensions in a relativistic field theory framework to describe two-particle scattering processes for non-rest frames, any number of channels, and any two scattering particles of arbitrary spin [133, 134, 135, 136, 137, 138]. I will give a brief summary following Ref. [134] since the derivation is quite involved. In the field theory framework, it can be shown that the difference between the finite-volume two-point correlation functions and the infinite-volume two-point correlation functions is given by some volume-dependent on-shell quantities plus some off-shell contributions that are exponentially suppressed by $e^{-m_i L}$ where m_i are the scattering particle massses [37]. As explained above, the finite-volume correlation functions contain a discrete set of poles along the real energy axis. These poles are volume-dependent and therefore, must originate from the volume-dependent on-shell quantities since the infinite-volume correlation function has no volume-dependence. The on-shell quantities are functions of energy and will diverge to give a finite-volume pole when they satisfy the quantisation condition,

$$\det[F^{-1}(E_{cm}, \vec{P}, L) + \mathcal{M}(E_{cm})] = 0. \tag{5.12}$$

This condition links the matrix of infinite-volume scattering amplitudes $\mathcal{M}$ and F^{-1} which is a matrix of known energy-dependent functions [138] that depends on box length L in a frame with total momentum $\vec{P}$. For some specified scattering amplitudes, the discrete spectrum in a L^3 volume is the set of energies for when this determinant condition is satisfied. The exact form of these two matrices depends on the number of channels and the spin of the scattering particles, but as mentioned earlier, I will concentrate this study on elastic pseudoscalar-pseudoscalar scattering. In this case, the two quantities are matrices in angular momentum space, l. $\mathcal{M} = 16\pi t$ is the matrix of elastic scattering amplitudes decomposed in terms of partial waves, $\mathcal{M}_l = 16\pi t_l$, and it is diagonal in angular momentum since it is an infinite-volume quantity. On the other hand, F^{-1} is a finite-volume quantity and is not diagonal in angular momentum space

$\vec{P}$	LG($\vec{P}$)	$\Lambda(P)$	l^N
[000]	O_h^D	A_1^+	$0^1, 4^1$
		T_1^-	$1^1, 3^1$
$[n00]$	Dic_4	A_1	$0^1, 1^1, 2^1, 3^1, 4^2$
		E_2	$1^1, 2^1, 3^2, 4^2$
$[nn0]$	Dic_2	A_1	$0^1, 1^1, 2^2, 3^2, 4^3$
		B_1	$1^1, 2^1, 3^2, 4^2$
		B_2	$1^1, 2^1, 3^2, 4^2$
$[nnn]$	Dic_3	A_1	$0^1, 1^1, 2^1, 3^2, 4^2$
		E_2	$1^1, 2^2, 3^2, 4^3$

Table 5.1: The pattern of subductions of pseudoscalar-pseudoscalar partial waves, $l \leq 4$, into some lattice irreps, Λ, where N is the number of embeddings of this l in this irrep. $\vec{P}$ is given in units of $\frac{2\pi}{L}$ and n is an integer.

due to the breaking of rotational symmetry. As discussed later, F^{-1} can be subduced to a particular lattice irrep, Λ, such that it is block diagonal with non-zero elements only when l subduces into Λ. The pattern of subductions of $l \leq 4$ into the lattice irreps that I will consider is given in Table 5.1.

The determinant condition is exact up to the off-shell $e^{-m_i L}$ corrections, where m_i^{-1} governs the range of the interaction, which is analogous to the condition in the one-dimensional case discussed earlier that the volume has to be much larger than the range of the interaction. This quantisation condition is only valid for two-body scattering. Progress to extend the quantisation condition to account for scattering with three or more particles is an active area of research. Currently, a quantisation condition for three identical spinless particles has been formally derived [40, 41, 42, 43] but a practical implementation in lattice QCD calculations has not yet been made. Because of this restriction, scattering calculations cannot rigorously be performed above three-body thresholds. This restriction is one reason why scattering amplitude calculations in lattice

QCD are typically performed with unphysically heavy light quarks because the three-body thresholds are further up in the spectrum and offer a larger energy window to determine the two-body scattering amplitudes.

5.3 Solving the quantisation condition

To make use of the quantisation condition in practice, it is convenient to recast it in a different form by replacing $\mathcal{M} = 16\pi t$ and $F = \frac{i}{16\pi}\rho(1 + i\mathcal{F})$ where $\mathcal{F}(E_{cm}, \vec{P}, L)$ is a known real function.[1] The most general form of $\mathcal{F}$ can be read off from Equation (23) of Ref. [138] which can be reduced to the spinless single-channel case for the purposes of these subsequent calculations. The quantisation condition now reads

$$\det[1 + i\rho t_{(l)}(1 + i\mathcal{F})] = 0. \tag{5.13}$$

The matrices are of infinite dimension with the rows and columns labelled by the partial waves l. To be able to calculate the determinant on a computer, the matrices are truncated up to some number of l. This truncation is justified since contributions from higher partial waves are suppressed at low energies with $\delta_l(k) \sim k^{2l+1}$.

Since the energy levels I extract in lattice calculations are obtained within a lattice irrep Λ at momentum $\vec{P}$, this quantisation condition can calculated to obtain the energy levels within a given irrep by projecting $\mathcal{F}$,

$$\mathcal{F}^{\vec{P},\Lambda}_{ln;l'n'}\delta_{\Lambda\Lambda'}\delta_{\mu\mu'} = S^{l,m}_{\Lambda,\mu,n}\mathcal{F}^{\vec{P}}_{lm;l'm'}S^{l',m'}_{\Lambda',\mu',n'} \tag{5.14}$$

where n labels the n'th embedding of l subducing into the lattice irrep Λ. Writing out fully now the quantisation condition,

$$\det\left[\delta_{ll'}\delta_{nn'} + i\rho t_{(l)}\left(\delta_{ll'}\delta_{nn'} + i\mathcal{F}^{\vec{P},\Lambda}_{ln;l'n'}\right)\right] = 0 \tag{5.15}$$

where $t_{(l)}$ is diagonal in l since it is an infinite-volume quantity and $\mathcal{F}^{\vec{P},\Lambda}$ is block diagonal with non-zero elements only when l subduces into Λ as tabulated in Table 5.1.

[1] Beware of some references that label $\mathcal{F}$ by $\mathcal{M}$ which should not be confused with the scattering amplitude.

Given specified scattering amplitudes up to some l, the energy levels within a finite-volume for lattice irrep Λ at momentum $\vec{P}$ can be calculated by finding the energies that satisfy this determinant equation. However, this is the opposite of what is wanted as lattice QCD calculates the energy levels from which the scattering amplitudes need to be determined. The next section will describe how to calculate the scattering amplitudes from the finite-volume energy levels using the quantisation condition.

5.4 Determining scattering amplitudes

In the simplest of cases, scattering is dominated by the lowest partial wave when considering low-energy scattering since contributions from all the higher partial waves follow a hierarchy, $\delta_l \sim k^{2l+1}$, and can be neglected. Then the matrices, $t(l)$ and $\mathcal{F}$, are 1×1 matrices and the quantisation condition reads

$$\cot \delta_l(E_{cm}) = -\cot \phi_l^{\Lambda}(E, \vec{P}, L) \tag{5.16}$$

where δ_l is the lowest contributing phase shift and $\cot \phi_l^{\Lambda}$ is a known function that is determined from $\mathcal{F}$. Computing the scattering amplitude simply requires inserting an extracted energy level of the finite-volume spectra into this equation to get a single value of δ_l at that energy. By extracting many energy levels in many volumes and at different momenta, many phase shift points can be mapped out across an energy region.

This method quickly fails once more than one partial wave is considered as the quantisation condition becomes one equation containing multiple unknown $\delta_l(E_{cm})$, and is underconstrained. An alternative method is to assume that the scattering amplitudes are smooth functions of energy and parametrise the energy dependence of the scattering amplitudes in terms of some number of parameters, $\{a_i\}$. The Lüscher quantisation condition can be solved to obtain the finite-volume spectrum $\{E_{cm}^{\text{par}}\}$ for the set of parameters which are fit to reproduce the extracted spectrum $\{E_{cm}\}$. Following the

implementation of Refs. [67, 95], a χ^2 function is minimised

$$\chi^2(\{a_i\}) = \sum_{\substack{\vec{P}\Lambda\mathfrak{n} \\ \vec{P}'\Lambda'\mathfrak{n}'}} [E_{cm}(\vec{P}\Lambda\mathfrak{n}) - E_{cm}^{\text{par}}(\vec{P}\Lambda\mathfrak{n};\{a_i\})]\mathbb{C}^{-1}(\vec{P}\Lambda\mathfrak{n};\vec{P}'\Lambda'\mathfrak{n}')[E_{cm}(\vec{P}'\Lambda'\mathfrak{n}') - E_{cm}^{\text{par}}(\vec{P}'\Lambda'\mathfrak{n}';\{a_i\})] \tag{5.17}$$

where $E_{cm}^{\text{par}}(\vec{P}'\Lambda'\mathfrak{n}';\{a_i\})$ is the $\mathfrak{n}$'th solution of the quantisation condition for a t-matrix parametrised with parameters $\{a_i\}$ and $\mathbb{C}$ is the correlation matrix between extracted energy levels from lattice calculations, $E_{cm}(\vec{P}\Lambda\mathfrak{n})$.

The parametrisation of the scattering amplitudes should ensure that unitarity is satisfied and analytical continuation into the complex s plane is possible. For low-energy scattering, the scattering amplitudes are well described by the effective range expansion

$$k^{2l+1}\cot\delta_l = \frac{1}{a_l} + \frac{1}{2}r_l k^2 + \mathcal{O}(k^4) \tag{5.18}$$

where the parameters a_l and r_l are known as the scattering length and effective range. This parametrisation is flexible as it can describe repulsive scattering or attractive scattering and can give rise to a pole in the scattering amplitudes.

A more general approach of parametrising the t-matrix is to use the K-matrix description, in a slightly different form compared to Equation (5.5),

$$t_l^{-1}(s) = \frac{1}{(2k)^l}K_l^{-1}(s)\frac{1}{(2k)^l} + I(s) \tag{5.19}$$

where the $(2k)^{-l}$ factors ensure the correct behaviour at kinematic thresholds [139] and $I(s)$ is a function which must have $\text{Im}[I(s)] = -\rho(s)$ above threshold and $\text{Im}[I(s)] = 0$ below threshold to satisfy unitarity. There is some remaining freedom in its choice and this will be discussed in the next paragraph. The advantage of utilising the K-matrix formulation is that $K_l(s)$ is a real from unitarity and is parametrised in terms of some real parameters whilst $I(s)$ is constrained by unitarity above threshold. Although not seen in this work, the formulation is particularly useful for coupled-channel scattering but in this case, $K_l(s)$ is a 1×1 matrix. The energy dependence of the K-matrix can be parametrised by a pole term and a sum of polynomials

$$K_l(s) = \left(\sum_{n=0}^{N_g} g_l^{(n)} s^n\right)^2 \frac{1}{m_l^2 - s} + \sum_{n=0}^{N_\gamma}\gamma_l^{(n)}s^n \tag{5.20}$$

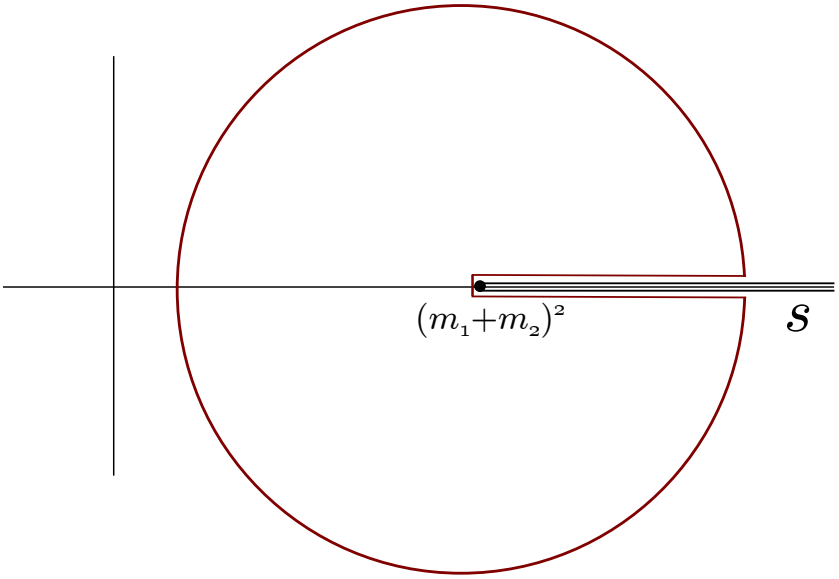

Figure 5.1: A sketch of the complex plane with branch point at $s = (m_1 + m_2)^2$ and branch cut running to positive infinity. The closed contour is continuously deformed around the branch cut and does not cross any singularities.

where $m_l, \{g_l^{(n)}\}, \{\gamma_l^{(n)}\}$ are real parameters. To reduce the reliance on a single parametrisation in this work, many parametrisations, with all combinations up to $N_g = N_\gamma = 1$, will be used to attempt to reproduce the finite-volume spectrum.

As mentioned earlier, $I(s)$ must have $\text{Im}[I(s)] = -\rho(s)$ above threshold and $\text{Im}[I(s)] = 0$ with some remaining freedom in choosing $I(s)$. One of the simplest choices is to pick $\text{Re}[I(s)] = 0$ above threshold. A more sophisticated approach relying on analyticity and unitarity is the Chew-Mandelstam prescription [140] that analytically continues the phase space below threshold, through a dispersion relation relating the real part to the imaginary part. Recall Cauchy's integral formula around some closed contour,

$$I(s) = \frac{1}{2\pi i} \oint ds' \, \frac{I(s')}{s' - s}. \tag{5.21}$$

If there is a branch point at $s_{\text{thr}} = (m_1 + m_2)^2$ with a cut running to positive infinity, the closed contour can be continuously deformed around the branch cut to run along

the real axis without crossing singularities to give the integral

$$I(s) = \frac{1}{2\pi i} \int_{s_{\text{thr}}}^{\infty} ds' \, \frac{I(s' + i\epsilon) - I(s' - i\epsilon)}{s' - s} \tag{5.22}$$

plus an integral around a circular path that approaches zero as the contour is pushed towards infinity. A sketch of this contour is given in Figure 5.1. Using the Schwartz reflection principle, $I(s) = I(s^*)^*$, gives $I(s + i\epsilon) - I(s - i\epsilon) = 2i\text{Im}[I(s)]$ but unitarity gives the imaginary part of $I(s)$ so

$$I(s) = -\frac{1}{\pi} \int_{s_{\text{thr}}}^{\infty} ds' \, \frac{\rho(s')}{s' - s}. \tag{5.23}$$

This integral is divergent but it can be regulated through a subtraction to give

$$I(s) = I(s_{\text{thr}}) - \frac{s - s_{\text{thr}}}{\pi} \int_{s_{\text{thr}}}^{\infty} ds' \, \frac{\rho(s')}{(s' - s)(s' - s_{\text{thr}})}. \tag{5.24}$$

This integral can be solved and the solution is given in Ref. [96]. An extra freedom remains in the subtraction point: a convenient choice used here is to choose $I(s_{\text{thr}})$ such that $\text{Re}[I(s = m_l^2)] = 0$ at the position of the pole, m_l^2, of the K_l-matrix. At the end of the day, the choice of $I(s)$ is arbitrary but the Chew-Mandelstam prescription is numerically tractable since it provides a smoother transition across the threshold. For this reason, I will use the Chew-Mandelstam prescription with the subraction at the pole of the K-matrix in all parametrisations.

5.5 Finite-volume spectrum

Having reviewed the methods to obtain the scattering amplitudes from the finite-volume spectra, the objective now is to determine the isospin-0 DK scattering amplitudes. I will now present the relevant finite-volume spectra in the isospin-0 charm-strange channel that I obtained from lattice QCD calculations. These computations are performed on the $M_\pi = 236$ MeV and 32^3 ensemble described in Section 2.9 with $N_{\text{vecs}} = 256$. Since the calculation of correlation functions contains disconnected contributions, the distillation framework is particularly suitable for handling these contributions. As discussed at the

start of Chapter 3, the anisotropy was calculated from the relativistic dispersion relation for a stable meson to be $\xi_\pi = 3.453(6)$ from the pion, $\xi_K = 3.449(4)$ from the kaon, and $\xi_D = 3.443(7)$ from the D. These numbers are statistically consistent with each other. A conservative approach to incorporate an estimate of systematic uncertainties, that encompasses all of these anisotropies, is to take $\xi = 3.453(17)$ in the subsequent calculations. One important check is that the product of the lightest scattering particle mass and the length of the box, $M_K L > 9$, is sufficiently large to ensure that finite-volume corrections are exponentially suppressed and the Lüscher quantisation condition is valid.

The energy levels in the extracted finite-volume spectrum will be calculated at rest and in frames with momentum $\vec{P} = \frac{2\pi}{L}\vec{N}$. The finite-volume spectrum in the *cm* frame is obtained by boosting the extracted energy, $a_t E$, to the rest frame

$$(a_t E_{cm})^2 = (a_t E)^2 - \left(\frac{2\pi}{\xi L/a_s}\right)^2 \vec{N}^2. \tag{5.25}$$

The positions of the non-interacting meson-meson energy levels are given by Equation (4.2) and are boosted back to the *cm* frame as above. The energies of the relevant stable mesons and thresholds are given in Table 5.2. The σ meson was found to be a broad resonance on this ensemble [98], and so in order to extract energy levels related to the σ meson, the $D_s\pi\pi$ and $D_s^*\pi\pi$ levels will be interpolated by '$D_s\sigma$' and '$D_s^*\sigma$' operators where the σ operator is variationally optimised and contains a linear combination of single-meson and meson-meson operators in a similar manner to how the ρ was treated in Section 4.3. Operators for other channels will be used to disentangle the energy levels and ensure the correct finite-volume spectrum is reliably extracted. The scattering amplitudes will be constrained in the elastic DK region which is far below the three-body thresholds.

The extracted finite-volume spectra are shown in Figures 5.2 and 5.3 labelled by overall momentum and lattice irrep, $[\vec{P}]\Lambda^{(P)}$, calculated using a large basis of single-meson and meson-meson operators in Table B.3 and B.4 of Appendix B. The points show the extracted finite-volume energy levels in the *cm* frame in lattice units ($a_t E_{cm}$);

Meson	Mass
π	0.03928(18)
η	0.09299(56)
K	0.08344(7)
D	0.30922(12)
D^*	0.3304(2)
D_s	0.32344(15)
D_s^*	0.34442(17)

Threshold	Energy
DK	0.39266(14)
$D_s\eta$	0.4165(6)
D^*K	0.4134(2)
$D_s^*\eta$	0.4374(5)
$D_s\pi\pi$	0.4020(3)
$D_s^*\pi\pi$	0.4230(3)

Table 5.2: Left table gives relevant stable meson masses on this lattic ensemble [75, 77] and right table shows the relevant kinematic thresholds measured in lattice units. Only the statistical uncertainty is shown.

black points in the elastic region are used in the subsequent scattering analysis whilst grey points are not. The dashed lines give the kinematic multi-meson thresholds and the curves give the non-interacting energy levels.

Before performing a scattering analysis, some brief comments can be made on the qualitative features of the spectra. Figure 5.2 shows the spectra which have $l = 0$ as the lowest partial wave contribution. As a reminder, the subduction of partial waves is shown in Table 5.1. The presence of an 'extra' energy level compared to the number of non-interacting energy levels in the energy region $a_t E_{cm} = 0.38 - 0.41$ and shifts away from the non-interacting energy levels suggest that there is a significant interaction. These features could possibly arise from a bound state or resonance in the scattering amplitudes in $J^P = 0^+$. In the non-rest frames which contain $l = 1$ contributions, there is an energy level at $a_t E_{cm} \approx 0.34$ far below the kinematic thresholds. This low-lying energy level is not seen in the rest frame $\Lambda^P = A_1^+$ which does not contain $l = 1$ partial contributions so this suggests that there is a deepy bound state in $J^P = 1^+$. Further evidence for this deeply bound state can be seen by the presence of a similar energy level in the irreps in Figure 5.3 which have $l = 1$ as the lowest partial wave contribution.

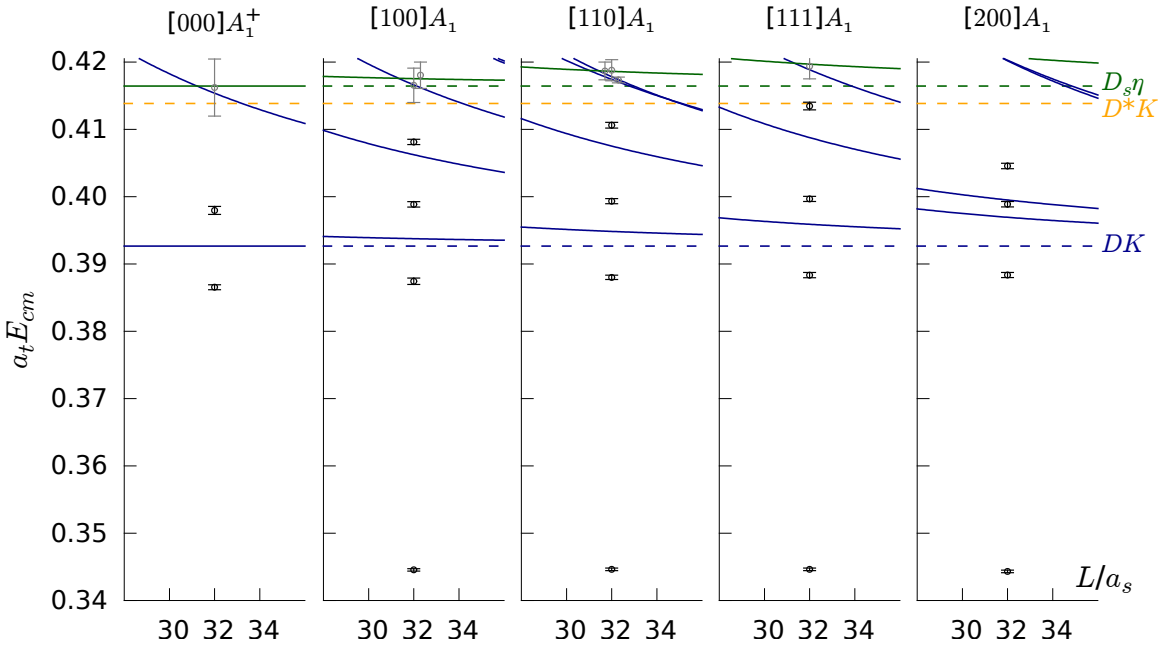

Figure 5.2: Finite-volume spectra, expressed in lattice units in the *cm* frame, in the $[\vec{P}]\Lambda^{(P)} = [000]A_1^+, [100]A_1, [110]A_1, [111]A_1, [200]A_1$ irreps. Points show the energy levels with error bars giving the one-sigma statistical uncertainty on either side of the mean; black points within the elastic region indicate they are used in the subsequent scattering analysis whilst grey points are not. The dashed lines give the DK (blue), $D_s\eta$ (green), D^*K (yellow) thresholds and the solid curves give the corresponding non-interacting meson-meson energies. These irreps have $l = 0$ as the lowest partial wave contribution.

It is also interesting to note the presence of an extra energy level below the D^*K threshold in the non-rest frames at $a_t E_{cm} \approx 0.41$ in Figure 5.3 but it is not seen in the rest frame. These energy levels could arise from a bound state in the D^*K scattering amplitudes in $J^P = 1^+$ which would contribute to the non-rest frames whilst being forbidden by parity in $\Lambda^P = T_1^-$. This bound state would possibly be related to the experimental $D_{s1}(2460)$ state but no further conclusions can be made without determining the D^*K amplitudes. An extended coupled channel analysis would be desirable for future studies but this is beyond the scope of this current work.

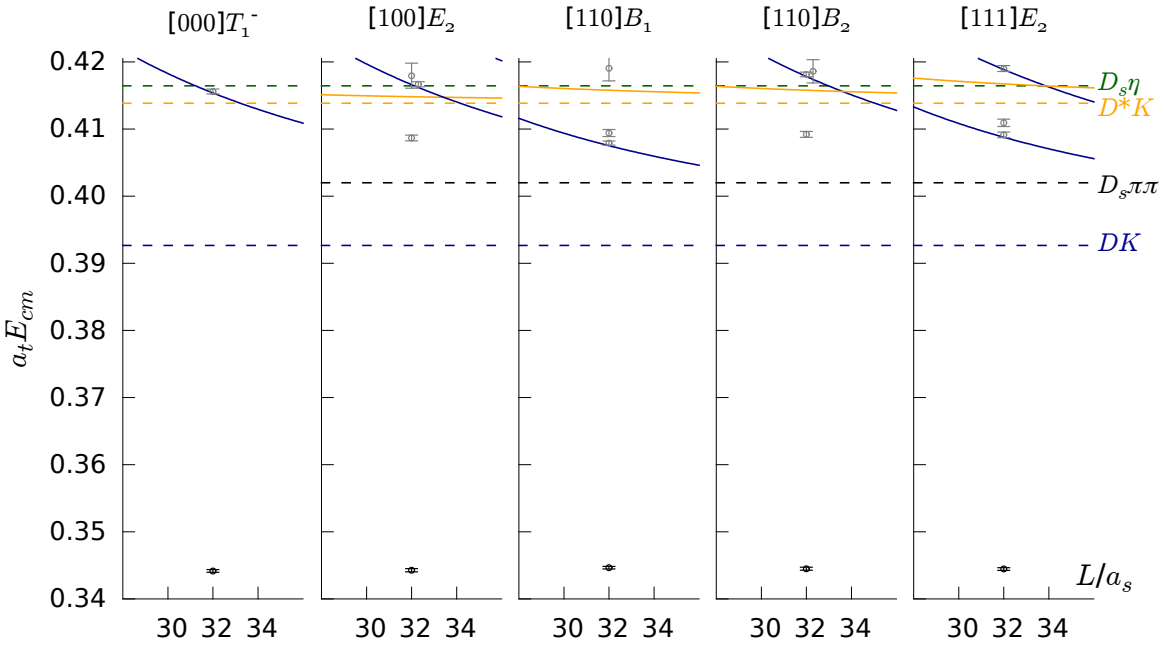

Figure 5.3: As Figure 5.2 but for the $[\vec{P}]\Lambda^{(P)} = [000]T_1^-, [100]E_2, [110]B_1, [110]B_2, [111]E_2$ irreps and the black dashed line gives the $D_s\pi\pi$ threshold. These irreps have $l = 1$ as the lowest partial wave contribution.

5.6 DK scattering amplitudes

In the simplest case where partial wave contributions from $l \geq 1$ are assumed to be suppressed and neglected, the Lüscher quantisation condition reduces to Equation (5.16) and the S-wave phase shift can be solved directly to obtain a single point for each energy level. Taking the one energy level above threshold in the $[000]A_1^+$ irrep in Figure 5.2, the corresponding phase shift point is shown by the black point in Figure 5.5. To obtain more phase shift points from the non-rest frame irreps, it is assumed that the lowest-lying energy level comes entirely from the $l = 1$ contribution as explained in the previous section and they should be excluded. The remaining energy levels in the elastic region are then assumed to only receive partial wave contributions from $l = 0$. The corresponding phase shift points that are mapped out by these energy levels are shown by the grey points in Figure 5.5. It can be seen that the phase shift points appear

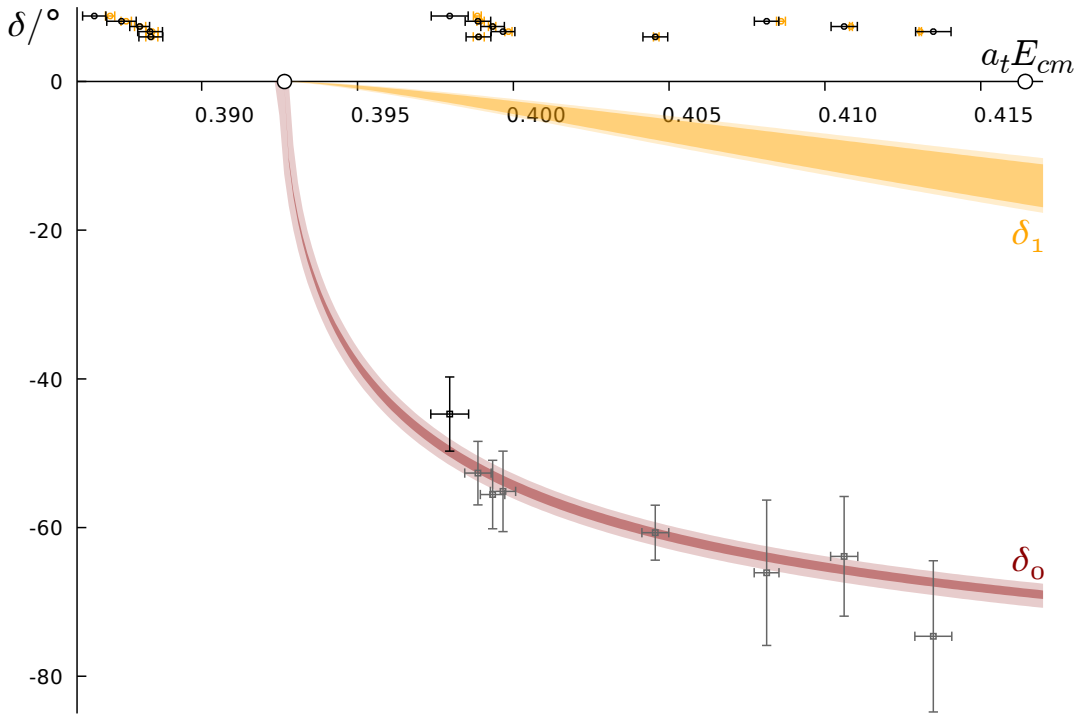

Figure 5.4: The black (grey) points give the S-wave phase shift obtained from the energy levels in the rest (non-rest) frames in Figure 5.2 directly from Equation (5.16) (assuming that $l \geq 1$ partial wave contributions are negligible). The open circle at $a_t E_{cm} = 0.3926$ gives the location of the DK threshold and the next circle indicates the opening of the $D_s\eta$ threshold. For the sample parametrisation described in Equation (5.26), the red (orange) inner band gives the resulting S-wave (P-wave) phase shift with the size of the band representing the one-sigma statistical uncertainty on either side of the mean, and the outer band represents the systematic uncertainty associated with varying the anisotropy and scattering meson masses within their uncertainties. The black circles above the energy axis show the position of the finite-volume energy levels used to constrain the scattering amplitudes within the energy region shown and the orange circles show the energy levels obtained from the sample parametrisation with the error bars showing only the statistical uncertainty.

to lie on the same curve. The rapid dip in the phase shift at the opening of the DK threshold could result from the presence of a nearby pole in the scattering amplitudes.

To proceed further, I will include partial wave contributions from $l = 0, 1$ and assume $l \geq 2$ contributions are negligible. Taking the 23 finite-volume energy levels from the spectra in Figures 5.2 and 5.3, I show a sample fit of a K-matrix parametrisation containing a pole term and a constant for $l = 0$ and a pole term for $l = 1$ that described the extracted spectra well,

$$\begin{aligned} m_0 &= (0.659 \pm 0.008 \pm 0.09) \cdot a_t^{-1} \\ g_0^{(0)} &= 1.25 \pm 0.03 \pm 0.2 \\ \gamma_0^{(0)} &= -2.7 \pm 0.2 \pm 0.2 \\ m_1 &= (0.34445 \pm 0.00011 \pm 0.00010) \cdot a_t^{-1} \\ g_1 &= 2.1 \pm 0.3 \pm 0.1 \\ & \chi^2/N_{\text{dof}} = \tfrac{26.70}{23-5} = 1.48. \end{aligned} \qquad \begin{bmatrix} 1 & 0.53 & -0.10 & 0.01 & -0.02 \\ & 1 & -0.89 & -0.05 & -0.14 \\ & & 1 & 0.03 & 0.12 \\ & & & 1 & 0.09 \\ & & & & 1 \end{bmatrix} \tag{5.26}$$

The first uncertainty gives the statistical uncertainty whilst the second uncertainty arises from systematically varying the anisotropy and scattering hadron masses within their uncertainties. The matrix shows the correlation between each parameter. Figure 5.4 shows the resulting phase shift from this parametrisation for $l = 0$ ($l = 1$) given by the red (orange) inner band with the size of the band representing the one-sigma statistical uncertainty on either side of the mean. The outer band represents the systematic uncertainty from varying the anisotropy and scattering hadron masses. The phase shift curve obtained from this parametrisation agrees with the phase shift points obtained previously. The finite-volume spectrum reproduced by this parametrisation from the Lüscher quantisation condition is given by the orange points and is consistent with the extracted finite-volume spectrum shown by the black circles above the energy axis. It is also important to note that the extracted finite-volume spectrum is spread across a large energy region giving good constraints of the scattering amplitudes across this energy region.

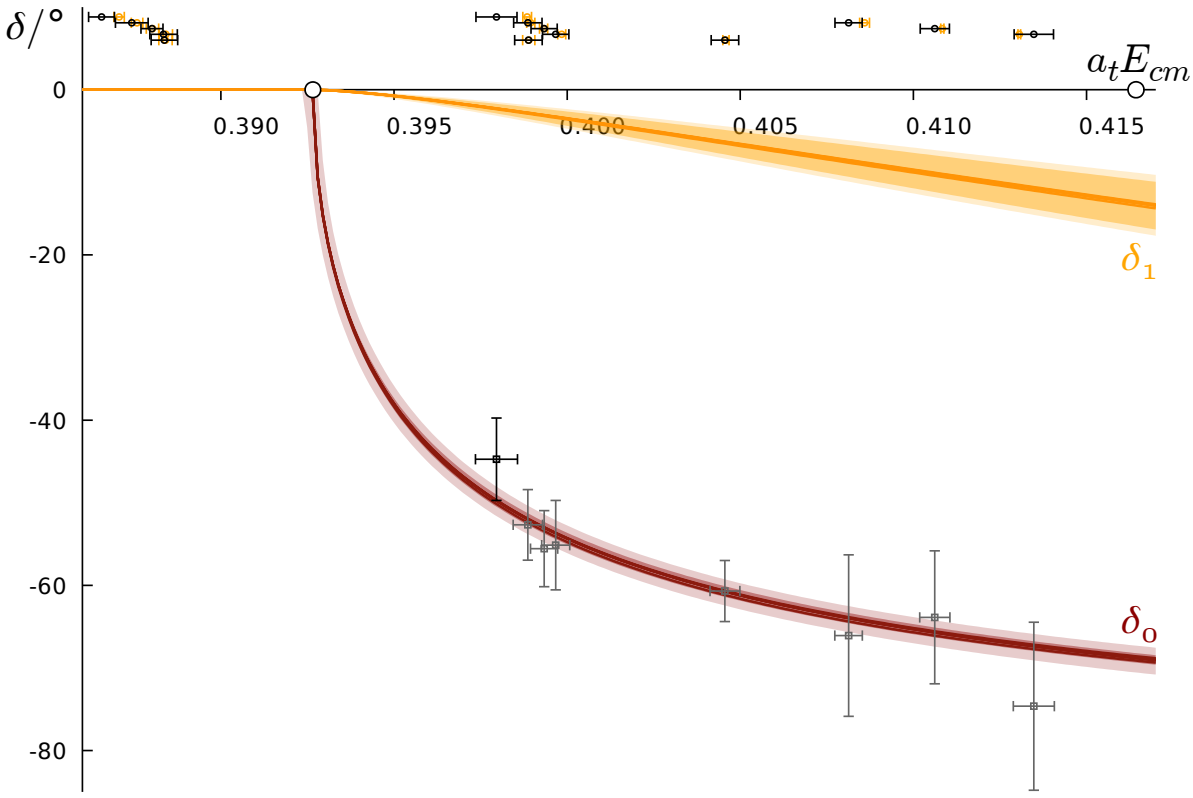

Figure 5.5: As Figure 5.4 but each red (orange) solid curve shows the S-wave (P-wave) phase shift obtained from all the scattering amplitude parametrisations listed in Appendix C.

Another good description of the extracted spectra is given by an effective range expansion for $l = 0$ and a K-matrix parametrisation containing a pole term for $l = 1$,

$$\begin{aligned} a_0 &= (-44.9 \pm 1.1 \pm 0.3) \cdot a_t \\ m_1 &= (0.34445 \pm 0.00012 \pm 0.00008) \cdot a_t^{-1} \\ g_1 &= 2.2 \pm 0.3 \pm 0.1 \\ & \chi^2/N_{\text{dof}} = \tfrac{26.77}{23-3} = 1.34 \end{aligned} \qquad \begin{bmatrix} 1 & -0.34 & -0.35 \\ & 1 & 0.10 \\ & & 1 \end{bmatrix} \quad . \tag{5.27}$$

In physical units, the scattering length is found to be $a_0 = -1.47(4)(1)$ fm. A seperate fit that included the effective range term did not improve the χ^2/N_{dof} and r_0 was found to be statistically consistent with zero.

Many different parametrisations of the scattering amplitudes were used in an attempt to describe the data. In the end, eight parametrisations successfully reproduced the finite-volume spectrum with $\chi^2/N_{\text{dof}} < 1.6$ and parameters that were not statistically consistent with zero, and the full details are listed in Appendix C. The P-wave amplitudes used the same K-matrix parametrised with a pole term in all cases as introducing new parametrisations did not improve the fit or gave parameters that were consistent with zero. The resulting phase shifts for $l = 0$ ($l = 1$) are shown by the solid red (orange) lines for each parametrisation in Figure 5.5 and it is found that there is practically no difference from varying the scattering amplitude parametrisations.

Another method to depict scattering amplitudes is to plot the quantities $k^{2l+1} \cot \delta_l$ – these are shown in Figure 5.6 for S and P-wave. The points in S-wave obtained from solving the Lüscher condition directly are in agreement with the curves obtained from the parametrisations. It can be seen by eye, $k \cot \delta_0 \approx -0.02$ is constant in this energy region, giving the scattering length to be $a_0 \approx -50 \cdot a_t$ and the effective range is zero which is consistent with the earlier results in Equation (5.27). From Equation (5.8), a bound state pole in the scattering amplitude arises when $k^{2l+1} \cot \delta_l = ik^{2l+1}$ and the intersection gives the position of the pole on the real axis of the physical sheet below threshold. The quantity, ik^{2l+1}, is plotted by the dashed curves in the figure and this intersection is seen which provides further evidence that there is a bound state in the scattering amplitudes.

Figure 5.7 shows the quantity $\rho^2 |t_l^2|$ which is proportional to the $DK \to DK$ cross section. The lack of enhancement in P-wave is consistent with there being a deeply bound state far below threshold which is not expected to have a large impact on physical scattering. A sharp rise is observed in S-wave which is indicative of a pole in the scattering amplitude. However, it is interesting to note that this feature does not have the standard Breit-Wigner shape. An understanding of how this enhancement in the cross section originates can be made by studying the singularity structure of the scattering amplitudes.

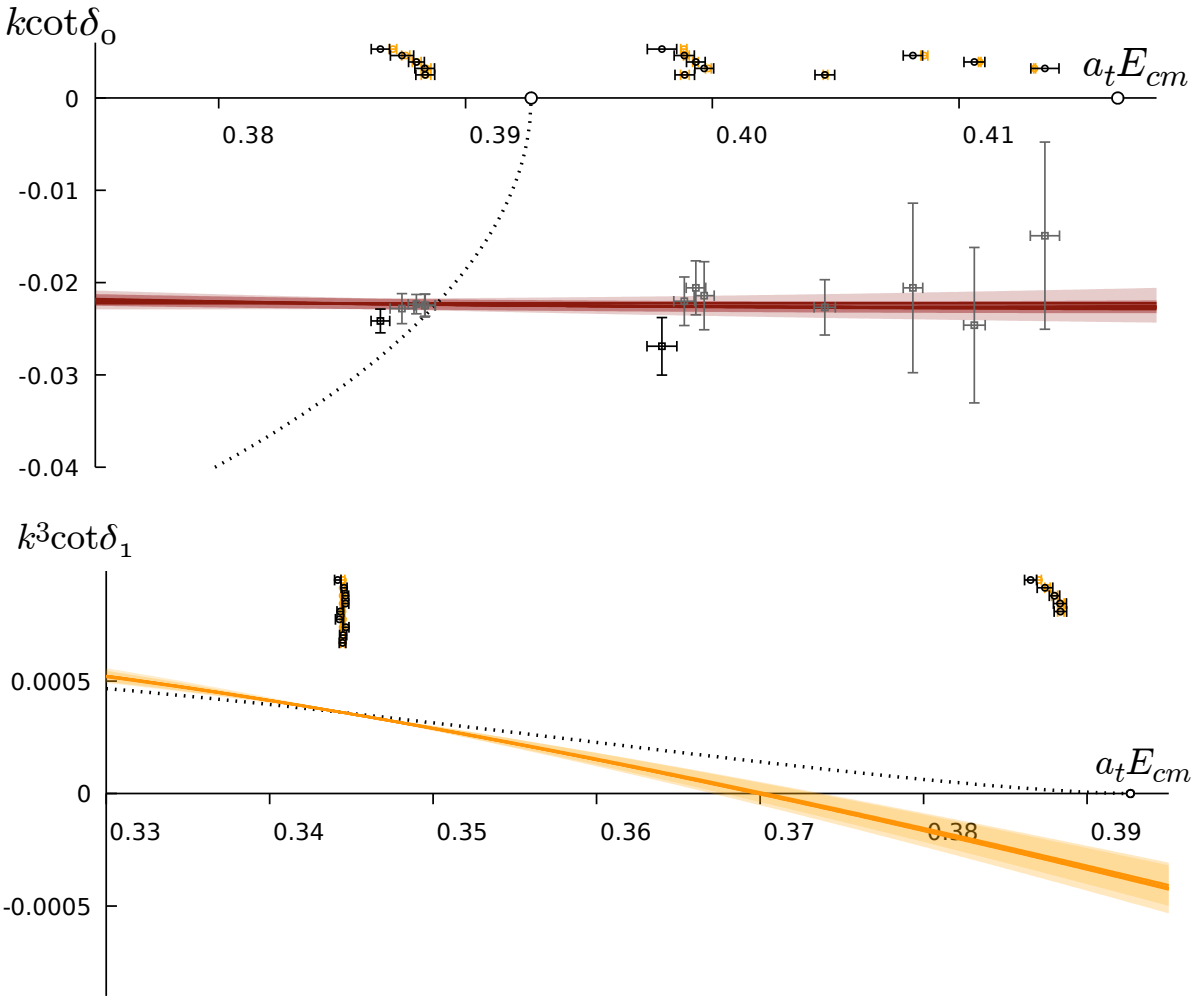

Figure 5.6: As Figure 5.5 but for the quantities $k\cot\delta_0$ (top panel) and $k^3\cot\delta_1$ (bottom panel). The dashed curves show ik^{2l+1}.

5.7 Singularity structure of scattering amplitudes

To rigorously determine the bound state and resonance content, the scattering amplitudes are analytically continued into the complex s plane. Poles are found numerically by performing an integral around a closed contour which would be zero if there are no poles within the contour by the residue theorem.

In P-wave, a bound state pole is found on the real axis of the physical sheet far below the threshold. Due to how deeply bound this state is, it is not expected to

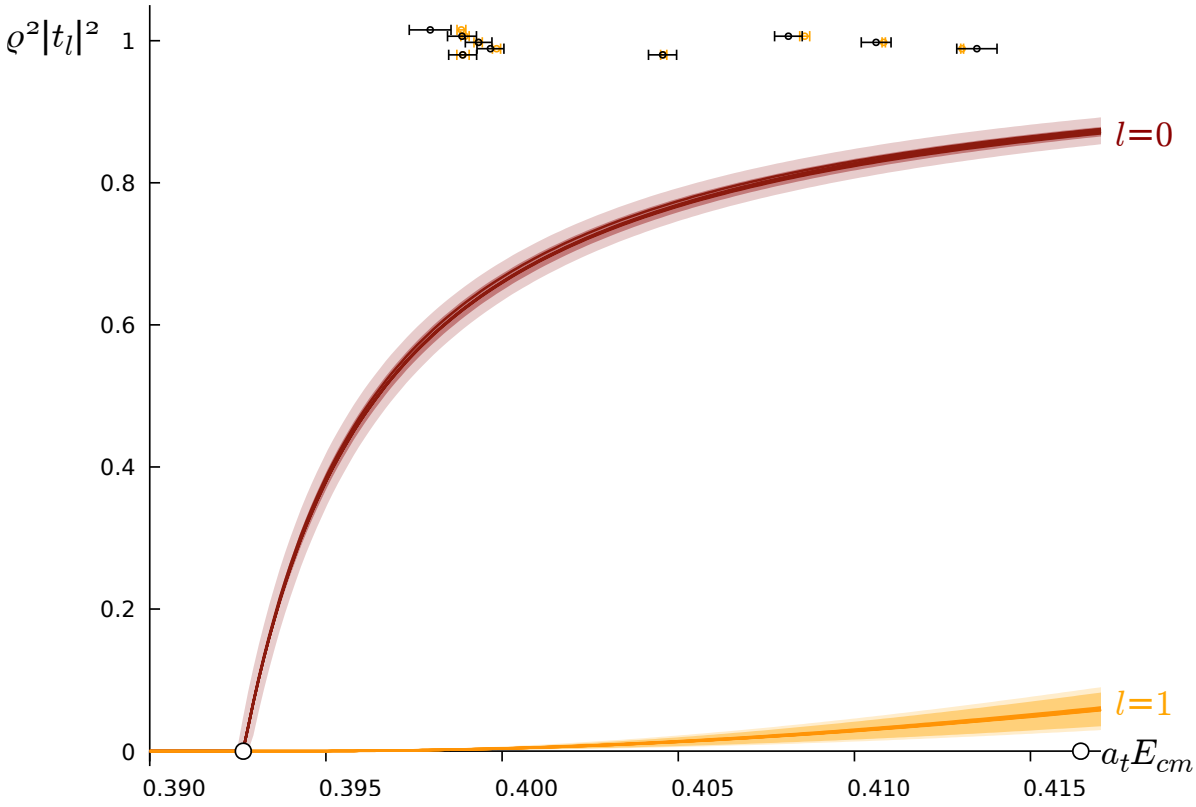

Figure 5.7: As Figure 5.5 but for the quantity $\rho^2|t_l|^2$.

strongly influence physical scattering above threshold and this is consistent with what was shown in the previous section. Averaging over the eight parametrisations gives the mass in physical units of the bound state to be 2066(1) MeV with the error encompassing the uncertainty from all the parametrisations. I identify this bound state, with $J^P = 1^-$, to be the experimental vector $D_s^*(2112)$ state [15].

For the more interesting S-wave case, I find a bound state pole on the real axis of the physical sheet close to the DK threshold and the position of the pole in physical units is plotted in Figure 5.8 for the eight parametrisations. The mass of the bound state is consistent for each parametrisation and averaging gives 2331(3) MeV with the uncertainty encompassing the total uncertainties from the individual parametrisations. The binding energy of the bound state is found to be $\epsilon = 21(3)$ MeV and the proximity of the pole to the threshold should have a significant effect on physical scattering which

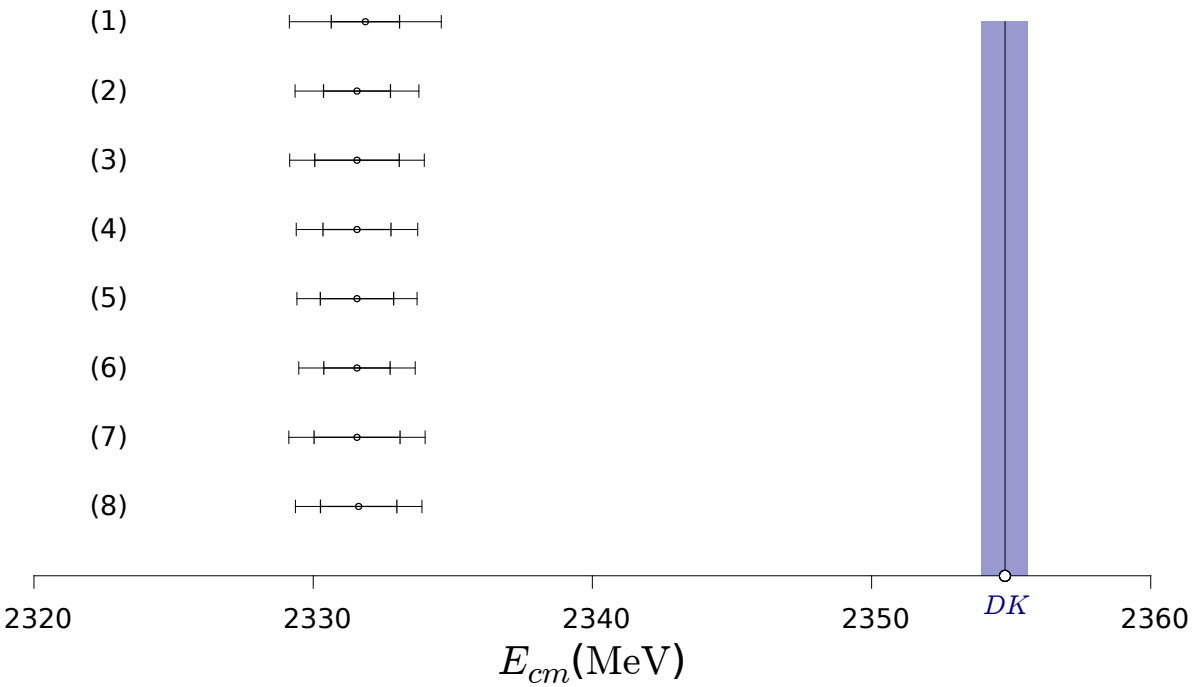

Figure 5.8: The position of the pole on the real axis of the physical sheet extracted from various parametrisations of the S-wave amplitudes identified by the number as listed in Appendix C. The inner error bars show the one-sigma statistical uncertainty and the outer bars give the uncertainty arising from the uncertainty of the scattering meson masses and the anisotropy. The open circle on the axis gives the position of the DK threshold and the blue band represents the statistical uncertainty.

is observed by the enhancement in the cross section in Figure 5.7. The coupling of the pole is plotted in Figure 5.9 – there is no parametrisation dependence and averaging finds $g = 1375(24)$ MeV with the uncertainty encompassing the uncertainty from each parametrisation. No further poles were found on either sheet in the energy region of constraint.

5.8 Pole interpretation

Comparing with experiment, the bound state in S-wave can be identified with the experimental $D^*_{s0}(2317)$ with mass 2317.7(6) [15] which is found to lie slightly below the

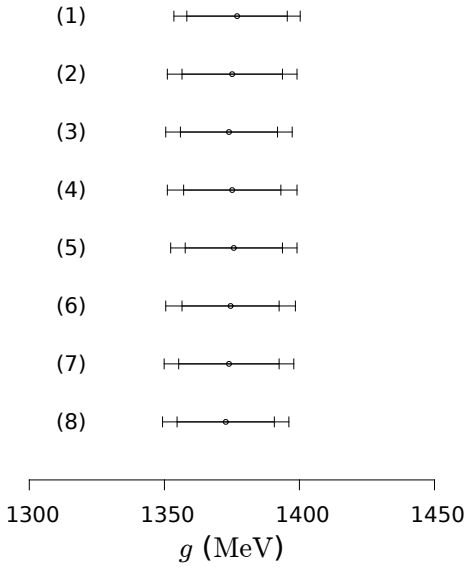

Figure 5.9: As Figure 5.8 but for the coupling of the pole in S-wave.

DK threshold with a binding energy of roughly 40 MeV. Since a complete error budget for the lattice QCD calculation arising from discretisation effects, tuning of parameters, scale setting, etc. has not been computed, it is not surprising to see that there are some mild quantitative differences. For example, a rough estimate of the systematic uncertainty from discretisation effects was found to be approximately 20 MeV [93] which brings these results in agreement with the experimental results. For future studies, a precision calculation with control over all systematic uncertainties would be desirable. In spite of this, the qualitative features of the experimental state and the extracted bound state in S-wave are in good agreement. The experimental state has been observed to decay to $D_s\pi$ which is highly suppressed and arises via $\pi^0 - \eta$ mixing due to isospin breaking. Since the light quarks used in the lattice QCD calculation are degenerate, this isospin violating decay is not allowed and the corresponding scattering amplitudes would need to calculated on a lattice with non-degenerate light quarks. The state has also been measured to decay to $D_s^*\gamma$ and the necessary hadronic matrix elements, to calculate the transition rate, can be obtained within lattice QCD. It would be interesting to compute this relevant quantity for future studies although this would require a set of

new techniques not introduced in this work.

Since the experimental $D_{s0}^{*}(2317)$ is not well described by quark models, this suggests it is not a purely compact $c\bar{s}$ state and its proximity to the DK threshold has led to it being considered as a bound DK molecule. One possible way to test this statement is to measure the compositeness of the computed bound state i.e. measure the probability to find the bound state, $|b\rangle$, in an elementary compact state, $|d\rangle$, $Z = \sum_d |\langle d|b\rangle|^2$. The bound state is purely compact if $Z = 1$ and on the other hand, it is purely composite if $Z = 0$.

Weinberg derived a relation to determine the compositeness of a state that is valid for the following criteria [141]: the state is bound, the state couples to a two-particle threshold with a small binding energy, and this two-body channel has zero orbital angular momentum. Since all of these conditions are reasonably satisfied for this S-wave shallow bound state, the relation can be used and is given by

$$a_0 = -2\frac{1-Z}{2-Z}\frac{1}{\sqrt{2\mu\epsilon}} + \mathcal{O}\left(1/\beta\right), \quad r_0 = -\frac{Z}{1-Z}\frac{1}{\sqrt{2\mu\epsilon}} + \mathcal{O}(1/\beta) \tag{5.28}$$

that relates the scattering length and effective range to Z where μ is the reduced mass of the two-body DK channel, ϵ is the binding energy of the bound state, and β is the range of the interaction. $\frac{1}{\sqrt{2\mu\epsilon}} \gg 1/\beta$ is ensured when the state is loosely bound with small binding energy which was found to be $\epsilon = 21(3)$ MeV from the previous section.

Suppose the bound state is purely composite i.e. $Z = 0$ which predicts $a_0 = -1.50(11)$ fm and r_0 is zero. This is consistent with the effective range parameters computed in Equation (5.27) where the scattering length in physical units is found to be $a_0 = -1.47(4)(1)$ fm. This supports $Z \approx 0$ and suggests that the bound state is mostly a composite state.

Alternatively, Z can be computed directly by solving for Z and putting in the value a_0 obtained from the effective range parametrisation in Equation (5.27). This gives $Z = 2 \pm 33\%$ to be a compact state. Overall, assuming that the Weinberg criteria is reasonably satisfied, the conclusion is that this relation suggests that the bound state is comprised of mostly a composite DK state.

5.9 Comparison with other lattice QCD studies

It is interesting to compare this result with a similar lattice QCD calculation of the $D\pi$ scattering amplitudes [47]. That calculation was performed on the 16^3 and 24^3 lattice with $M_\pi = 391$ MeV as described in Section 2.9 and an additional 20^3 lattice. In S-wave, a bound state was found on the real axis of the physical sheet roughly 1 MeV below the $D\pi$ threshold. One can think of that bound state pole as a 'lighter' version of the bound state pole extracted here in the DK amplitudes where $M_K = 500$ MeV and the mass parameters of the quarks have been varied. In other words, the flavour content of the two scattering particles looks like $(c\bar{q}_1)(q_1\bar{q}_2)$ where $q_1 = q_2$ are light quarks in the $D\pi$ case and for the DK case, q_1 is a light quark and q_2 is a strange quark. It is intriguing to see that the position of the pole moves closer towards the threshold as the mass parameter of the quarks is changed. This suggests that for quark masses closer to the physical point, the pole in $D\pi$ scattering could transition from a bound state to a resonance once the relevant threshold becomes light enough for the decay to happen. This could possibly explain the difference in stability of the $D^*_{s0}(2317)$, which is narrow, and the $D^*_0(2400)$, which is broad, may be due to the heaviness of the strange quark compared to the light quarks.

Comparing with other lattice QCD calculations that determined the DK scattering amplitudes, Lang et. al [44, 45] find a bound state 37(17) MeV below the DK threshold and the effective range parameters were found to be $a_0 = -1.33(20)$ fm and $r_0 = 0.27(17)$ fm. A reliable constraint of the scattering amplitudes requires multiple energy levels across a wide energy region but that study is limited in this way since only three energy levels are extracted. Bali et al. [48] find a bound state with mass 2348(4)(+6) MeV and a binding energy of 26(4)(-3) MeV. The scattering length and effective range were found to be $a_0 = -1.49(0.13)(-0.30)$ fm and $r_0 = 0.20(0.09)(+0.31)$. Although they obtain multiple energy levels from different lattices, they do not extract energy levels in non-rest frames. A more worrying concern is that the strange quark is quenched in their

calculations and there is no rigorous justification that this does not have a significant effect on the results, especially when considering that DK scattering contains a valence strange quark. To give some support to this statement, it has been shown that lattice QCD results of the ρ resonance in $\pi\pi$ scattering are highly sensitive to the quenching of the strange quark [142]. The results I present here overcome the issues with these other studies by calculating on a large lattice with $N_f = 2 + 1$ dynamical quarks. By constructing a large basis of operators of diverse structures, many energy levels were obtained in the rest frame and non-rest frames to give a good constraint of the scattering amplitudes across a large energy region. Overall, the results that I have obtained are in reasonable agreement with the other studies.

Chapter 6

Conclusions and Outlook

At the start of this thesis, I stated that the goal is to further understand exotic mesons from a first principles approach in lattice QCD. Here, an account of how this goal was achieved will be given. To summarise Chapter 3, I calculated extensive spectra in the charmonium sector across a wide range of channels and energies. The use of anisotropic lattices, distillation and the variational method with a large basis of properly constructed operators allows for a reliable extraction of excited state energies. With a reliable spin identification method, the energies of states up to $J = 4$ were computed including states with exotic J^{PC} quantum numbers showing that QCD realises exotic states beyond quark models. Most of the states in the spectra were found to be consistent with the $n^{2S+1}L_J$ pattern predicted by quark models. In addition, a number of states, including those with exotic J^{PC} quantum numbers, were identified to belong in the lightest and first excited hybrid meson supermultiplet. The spectra were compared at two different light quark masses and it was found that there were no qualitative differences between the two spectra. Some of the identified hybrids could possibly be candidates for the experimental states, such as $X(4260)$ or $X(4360)$, but a further understanding of these extracted states can be made in future studies by studying their unstable properties or determining the radiative transitions between states. The radiative transition requires the transition matrix elements, $\langle f|J^{\mu}|i\rangle$, which can be obtained from lattice QCD by calculating three-point correlation functions. Such calculations have been made under the quenched approximation e.g. [49, 50] and it would be desirable for future studies to perform a dynamical computation of these matrix elements.

One limitation with the spectra calculations in Chapter 3 was that the unstable nature of the states above threshold was not taken into account. To begin tackling this

problem, I gave a review on how to construct meson-meson operators in Chapter 4 and then presented a general construction of operators resembling compact tetraquarks that transformed irreducibly under the symmetries of the lattice, have a range of colour-flavour-spin structures and respected other discrete symmetries. As a demonstration, these two types of operators were used to calculate spectra in exotic flavour sectors where the flavour quantum numbers are not accessible by quark models. In the isospin-1 hidden charm and doubly charmed sector, it was found that the tetraquark operators did not have any significant effect on extracting the spectra. For the first time ever, the spectra was reliably extracted by using a sufficiently diverse basis of operators to extract all the relevant meson-meson states when the mesons have spin. The calculations of these channels were performed on a small lattice to maximise efficiency as a demonstration of the feasibility of these operators and it would be interesting to calculate with bigger volumes. Another avenue would be to perform similar calculations in the bottom sector. Finally, the spectra did not show qualitative signs of a bound state or narrow resonance being present in these channels. This presents a puzzle for the exotic charged Z states such as $Z_c(3900)$. One possible explanation for this is that $Z_c(3900)$ can be identified as a threshold cusp which does not originate dynamically from a pole in the scattering amplitudes. To strengthen these conclusions, the scattering amplitudes could be reliably determined in future studies by obtaining more energy levels on different volumes and non-rest frames.

In Chapter 5, a review was given of the Lüscher method that relates the finite-volume spectrum of lattice QCD to the scattering amplitudes in infinite-volume. Utilising the techniques described in the thesis, I computed the finite-volume spectra relevant for isospin-0 DK scattering and obtained the elastic DK scattering amplitudes from the Lüscher formalism. By investigating the singularity structure in the scattering amplitudes, a bound state pole was found in S-wave near threshold. The qualitative features of this pole were found to be consistent with the experimental $D_{s0}^*(2317)$ and it was found that this bound state is mostly a composite DK state, from the Weinberg com-

positeness relation, which is interesting phenomologically. Further understanding of this state could be made in future lattice QCD studies by calculating its radiative transition to $D_s^*\gamma$ which has been measured experimentally and can also be compared with different phenomological models. Another interesting quantity to compute is the charge radius of the state which can be obtained from the relevant matrix elements. This quantity could shed further insight on the compositeness and size of the bound state. In summary, the results here show that lattice QCD is a promising method to further understand exotic mesons from a first principles approach.

Appendix A

Diquark Models

A.1 One-gluon exchange model

The first model to consider is a simple one-gluon exchange model of a diquark where the two quarks interact via a colour-colour spin-spin interaction term [143]

$$H = -\alpha_s A_{12}(\lambda_1 \cdot \lambda_2)(\vec{S}_1 \cdot \vec{S}_2) \tag{A.1}$$

where A_{12} is a model-dependent term that behaves like $1/m_1 m_2$ in the heavy quark limit, λ are the Gell-Mann matrices that span the Lie algebra of $\mathrm{SU}(3)_C$ and $\vec{S}$ is the spin of the quark. The relative factors that arise for the different colour irrep R and spin S combinations are given in Table A.1. From this, it can be seen that the most attractive diquark is the $(R, S) = (\bar{\underline{3}}, 0)$ configuration and similarly, the most attractive anti-diquark is the $(R, S) = (\underline{3}, 0)$ configuration. Hence, a scalar $J^P = 0^+$ tetraquark built from this diquark–anti-diquark combination is expected to be the most favourable formation. Whilst other configurations are less favourable, this one-gluon exchange interaction is suppressed by the masses of the quarks such that in the heavy quark limit, a rich multiplet of tetraquark states in S-wave with $J^P = 0^+, 1^+, 2^+$ is expected to be observed in models such as Ref. [110]. In the case when the flavour irreps of the quarks within the diquark are identical, Fermi symmetry constrains the number of possible configurations. If the flavour irrep is antisymmetric, then the only allowed diquarks are the attractive configurations, $(\bar{\underline{3}}, 0)$ and $(\underline{6}, 1)$. Conversely, when the flavour irrep is symmetric, the only allowed diquarks are the repulsive configurations, $(\bar{\underline{3}}, 1)$ and $(\underline{6}, 0)$. One consequence of this is that the doubly-charmed cc diquark is always repulsive with the least repulsive diquark being $(\bar{\underline{3}}, 1)$. However, the repulsive interaction is suppressed

by the charm quark mass and so it is possible that such doubly-charmed tetraquarks may exist in the heavy quark limit.

		S	
		0	1
R	$\bar{3}$	$\frac{1}{2}$	$-\frac{1}{6}$
	6	$-\frac{1}{4}$	$\frac{1}{12}$

Table A.1: The relative factors of the colour-colour spin-spin interaction within the diquark in equation (A.1) for various colour irreps and spin.

A.2 Non-relativistic diquark model

Another model to consider is a non-relativistic quark model where a diquark state at rest with orbital angular momentum L and spin angular momentum S in total angular momentum J is constructed as

$$\left|\delta_{LS}^{J,m}\right\rangle = \sum_{m_L,m_S} \langle L, m_L; S, m_S | J, m\rangle \sum_{\alpha,\beta} \left\langle \tfrac{1}{2}, \alpha; \tfrac{1}{2}, \beta \middle| S, m_S \right\rangle \int \frac{d^3q}{(2\pi)^3}\, Y_L^{m_L}(\hat{q}) f_{nL}(|\vec{q}|) b_\alpha^\dagger(\vec{q}) b_\beta^\dagger(-\vec{q})|0\rangle\,, \tag{A.2}$$

where $b_\alpha^\dagger(\vec{q})$ is a creation operator for a quark of momentum $\vec{q}$ and J_z component α, and $f_{nL}(|\vec{q}|)$ is a model-dependent wavefunction that is determined by some interaction potential and is specified by L and the principal quantum number n. Annihilating this state with the field expansion of some diquark operator gives

$$\begin{aligned}\left\langle 0\middle|\delta^{J[\Gamma]}\middle|\delta_{LS}^{J,m}\right\rangle = &\sum_{m_L,m_S} \langle L, m_L; S, m_S | J, m\rangle \sum_{\alpha,\beta} \left\langle \tfrac{1}{2}, \alpha; \tfrac{1}{2}, \beta \middle| S, m_S \right\rangle \\ &\times \int \frac{d^3q}{(2\pi)^3}\, Y_L^{m_L}(\hat{q}) f_{nL}(|\vec{q}|)\, u_{(\alpha)}^T(\vec{q}) C\Gamma u_{(\beta)}(-\vec{q})\,,\end{aligned} \tag{A.3}$$

where u is a Dirac spinor. For $\Gamma = \gamma^5$, expanding u in the non-relativistic limit where $|\vec{q}|$ is much smaller than the mass of the quark gives up to leading order

$$\left\langle 0\middle|\delta^{J[\gamma^5]}\middle|\delta^{J,m}_{LS}\right\rangle = \sum_{m_L,m_S} \langle L, m_L; S, m_S|J, m\rangle \times \underbrace{\left(\left\langle \tfrac{1}{2}, -\tfrac{1}{2}; \tfrac{1}{2}, \tfrac{1}{2}\middle|S, m_S\right\rangle - \left\langle \tfrac{1}{2}, \tfrac{1}{2}; \tfrac{1}{2}, -\tfrac{1}{2}\middle|S, m_S\right\rangle\right)}_{\sim\delta_{S0}\delta_{m_S0}} \underbrace{\int \frac{d^3q}{(2\pi)^3}\, Y_L^{m_L}(\hat{q})}_{\sim\delta_{L0}\delta_{m_L0}} f_{nL}(|\vec{q}|)\,. \tag{A.4}$$

Hence, the operator $\delta^{J[\gamma^5]}$ overlaps with the $qq(^{2S+1}L_J = {}^1S_0)$ diquark construction. Similar results for other Γ are shown in Table A.2. Since the energy is expected to increase with orbital angular momentum, the S-wave operators should have largest overlap onto the lowest-lying states.

	1	γ_5	$\gamma_0\gamma_5$	γ_0	γ_i	$\gamma_i\gamma_0$	$\gamma_5\gamma_i$	$[\gamma_i, \gamma_j]$
$qq(^{2S+1}L_J)$	${}^3P_0$	${}^1S_0$	${}^1S_0$	-	${}^3S_1$	${}^3S_1$	${}^3P_1$	${}^1P_1$

Table A.2: The non-relativistic overlap of the diquark operator $\delta^{J[\Gamma]}$ onto the diquark state $qq(^{2S+1}L_J)$.

Appendix B

Operator Lists

The interpolating operators used to calculate the spectra in Figures 4.5, 4.6 and 4.7 in Chapter 4 are listed in Table B.1 for the isospin-1 hidden-charm sector and Table B.2 for the doubly-charmed sector.

The interpolating operators used to calculate the spectra in Figures 5.2 and 5.3 in Chapter 5 are listed in Tables B.3 and B.4.

T_1^{++}	A_1^{+-}	T_1^{+-}
$\delta^{b_0}_{\bar{3},3}\bar{\delta}^{b_1}_{3,\bar{3}}$	$\delta^{a_0}_{\bar{3},3}\bar{\delta}^{a_0}_{3,\bar{3}}$	$\delta^{a_0}_{\bar{3},3}\bar{\delta}^{a_1}_{3,\bar{3}}$
$\delta^{\rho}_{\bar{3},3}\bar{\delta}^{\pi}_{3,\bar{3}}$	$\delta^{\pi}_{\bar{3},3}\bar{\delta}^{\pi}_{3,\bar{3}}$	$\delta^{\rho}_{\bar{3},3}\bar{\delta}^{\pi}_{3,\bar{3}}$
$\delta^{\rho}_{\bar{3},3}\bar{\delta}^{\rho}_{3,\bar{3}}$	$\delta^{\rho}_{6,3}\bar{\delta}^{\rho}_{\bar{6},\bar{3}}$	$\delta^{\rho}_{\bar{3},3}\bar{\delta}^{\rho_2}_{3,\bar{3}}$
$D^{[000]}_{A_1}\bar{D}^{*[000]}_{T_1}$	$D^{[000]}_{A_1}\bar{D}^{[000]}_{A_1}$	$D^{[000]}_{A_1}\bar{D}^{*[000]}_{T_1}$
$D^{*[000]}_{T_1}\bar{D}^{*[000]}_{T_1}$	$D^{[100]}_{A_2}\bar{D}^{[100]}_{A_2}$	$D^{[100]}_{A_2}\bar{D}^{*[100]}_{A_1}$
$\eta_{c\,A_1}^{[000]}\rho^{[000]}_{T_1}$	$D^{*[000]}_{T_1}\bar{D}^{*[000]}_{T_1}$	$D^{[100]}_{A_2}\bar{D}^{*[100]}_{E_2}$
$J/\psi^{[000]}_{T_1}\pi^{[000]}_{A_1}$	$\eta_{c\,A_1}^{[000]}\pi^{[000]}_{A_1}$	$J/\psi^{[000]}_{T_1}\rho^{[000]}_{T_1}$
$J/\psi^{[100]}_{A_1}\pi^{[100]}_{A_2}$	$\eta_{c\,A_2}^{[100]}\pi^{[100]}_{A_2}$	$J/\psi^{[100]}_{A_1}\rho^{[100]}_{E_2}$
$J/\psi^{[100]}_{E_2}\pi^{[100]}_{A_2}$	$J/\psi^{[000]}_{T_1}\rho^{[000]}_{T_1}$	$J/\psi^{[100]}_{E_2}\rho^{[100]}_{A_1}$
		$J/\psi^{[100]}_{E_2}\rho^{[100]}_{E_2}$
		$\chi_{c0\,A_1}^{[100]}\pi^{[100]}_{A_2}$

Table B.1: The interpolating operators used to calculate the spectra in the isospin-1 hidden-charm sector overall at rest for irrep $\Lambda^{P(G)}$ in Chapter 4. For the tetraquark operators, I use the notation $\delta^{\Gamma_1}_{R_1,F_1}\bar{\delta}^{\Gamma_2}_{R_2,F_2}$ where $R_1(R_2)$ is the colour irrep, $\Gamma_1(\Gamma_2)$ is the gamma matrix and $F_1(F_2)$ is the flavour irrep of the diquark (anti-diquark) operator. For meson-meson operators, the optimised single-meson operators used are denoted by $M_\Lambda^{[n_1n_2n_3]}$, where M indicates the meson, Λ is the lattice irrep and $[n_1n_2n_3]$ is the momentum in units of $\frac{2\pi}{L}$. Note that all momenta related to $[n_1n_2n_3]$ by an allowed lattice rotation are summed over as shown in Equation (4.1).

$I=0$				$I=\frac{1}{2}$	
A_1^+	T_1^+	E^+	T_2^+	A_1^+	T_1^+
$\delta^{a_0}_{6,1}\bar{\delta}^{b_0}_{\bar{6},3}$	$\delta^{b_1}_{\bar{3},1}\bar{\delta}^{a_0}_{3,3}$	$\delta^{a_1}_{6,1}\bar{\delta}^{b_1}_{\bar{6},3}$	$\delta^{a_1}_{6,1}\bar{\delta}^{b_1}_{\bar{6},3}$	$\delta^{b_0}_{\bar{3},1}\bar{\delta}^{b_0}_{3,\bar{6}}$	$\delta^{a_1}_{6,1}\bar{\delta}^{b_0}_{\bar{6},3}$
$\delta^{a_1}_{6,1}\bar{\delta}^{b_1}_{\bar{6},3}$	$\delta^{\rho_2}_{\bar{3},1}\bar{\delta}^{\pi_2}_{3,3}$	$\delta^{b_1}_{\bar{3},1}\bar{\delta}^{a_1}_{3,3}$	$\delta^{b_1}_{\bar{3},1}\bar{\delta}^{a_1}_{3,3}$	$\delta^{b_1}_{\bar{3},1}\bar{\delta}^{a_1}_{3,3}$	$\delta^{b_1}_{\bar{3},1}\bar{\delta}^{a_0}_{3,3}$
$\delta^{b_0}_{\bar{3},1}\bar{\delta}^{a_0}_{3,3}$	$\delta^{\rho}_{\bar{3},1}\bar{\delta}^{\pi_2}_{3,3}$	$D^{[110]}_{A_2}D^{*[110]}_{B_2}$	$D^{[100]}_{A_2}D^{*[100]}_{E_2}$	$\delta^{\pi}_{6,1}\bar{\delta}^{\pi}_{\bar{6},\bar{6}}$	$\delta^{\rho}_{\bar{3},1}\bar{\delta}^{\pi}_{3,3}$
$\delta^{b_1}_{\bar{3},1}\bar{\delta}^{a_1}_{3,3}$	$\delta^{\rho}_{\bar{3},1}\bar{\delta}^{\pi}_{3,3}$		$D^{[110]}_{A_2}D^{*[110]}_{A_1}$	$\delta^{\rho}_{\bar{3},1}\bar{\delta}^{\rho}_{3,\bar{6}}$	$\delta^{\rho}_{\bar{3},1}\bar{\delta}^{\rho}_{3,\bar{6}}$
$D^{[000]}_{A_1}D(2S)^{[000]}_{A_1}$	$D^{[000]}_{A_1}D^{*[000]}_{T_1}$		$D^{[110]}_{A_2}D^{*[110]}_{B_1}$	$D^{[000]}_{A_1}D_{s\,A_1}^{[000]}$	$D^{[000]}_{A_1}D^{*[000]}_{s\,T_1}$
	$D^{[100]}_{A_2}D^{*[100]}_{A_1}$		$D^{*[100]}_{A_1}D^{*[100]}_{E_2}$	$D^{[100]}_{A_2}D_{s\,A_2}^{[100]}$	$D^{*[000]}_{T_1}D_{s\,A_1}^{[000]}$
	$D^{[100]}_{A_2}D^{*[100]}_{E_2}$			$D^{[110]}_{A_2}D_{s\,A_2}^{[110]}$	$D^{[100]}_{A_2}D^{*[100]}_{s\,A_1}$
	$D^{*[000]}_{T_1}D^{*[000]}_{T_1}$			$D^{*[000]}_{T_1}D^{*[000]}_{s\,T_1}$	$D^{[100]}_{A_2}D^{*[100]}_{s\,E_2}$
	$D^{*[100]}_{A_1}D^{*[100]}_{E_2}$			$D^{*[100]}_{A_1}D^{*[100]}_{s\,A_1}$	$D^{*[100]}_{A_1}D_{s\,A_2}^{[100]}$
	$D^{*[100]}_{E_2}D^{*[100]}_{E_2}$			$D^{*[100]}_{E_2}D^{*[100]}_{s\,E_2}$	$D^{*[100]}_{E_2}D_{s\,A_2}^{[100]}$
					$D^{*[000]}_{T_1}D^{*[000]}_{s\,T_1}$
					$D^{*[100]}_{A_1}D^{*[100]}_{s\,E_2}$
					$D^{*[100]}_{E_2}D^{*[100]}_{s\,A_1}$
					$D^{*[100]}_{E_2}D^{*[100]}_{s\,E_2}$

Table B.2: As Table B.1 but for the doubly-charmed sector with isospin-0 (left columns) and isospin-$\frac{1}{2}$ (right columns).

$[000]A_1^+$	$[100]A_1$	$[110]A_1$	$[111]A_1$	$[200]A_1$
$D_{A_1}^{[000]}K_{A_1}^{[000]}$	$D_{A_2}^{[100]}K_{A_1}^{[000]}$	$D_{A_2}^{[110]}K_{A_1}^{[000]}$	$D_{A_2}^{[111]}K_{A_1}^{[000]}$	$D_{A_2}^{[200]}K_{A_1}^{[000]}$
$D_{A_2}^{[100]}K_{A_2}^{[100]}$	$D_{A_1}^{[000]}K_{A_2}^{[100]}$	$D_{A_2}^{[100]}K_{A_2}^{[100]}$	$D_{A_2}^{[110]}K_{A_2}^{[100]}$	$D_{A_2}^{[100]}K_{A_2}^{[100]}$
$D_{A_2}^{[110]}K_{A_2}^{[110]}$	$D_{A_2}^{[110]}K_{A_2}^{[100]}$	$D_{A_1}^{[000]}K_{A_2}^{[110]}$	$D_{A_2}^{[100]}K_{A_2}^{[110]}$	$D_{A_2}^{[210]}K_{A_2}^{[100]}$
$D_{A_2}^{[111]}K_{A_2}^{[111]}$	$D_{A_2}^{[200]}K_{A_2}^{[100]}$	$D_{A_2}^{[111]}K_{A_2}^{[100]}$	$D_{A_2}^{[000]}K_{A_2}^{[111]}$	$D_{A_2}^{[110]}K_{A_2}^{[110]}$
$D_{s\,A_1}^{[000]}\eta_{A_1}^{[000]}$	$D_{A_2}^{[100]}K_{A_2}^{[110]}$	$D_{A_2}^{[210]}K_{A_2}^{[100]}$	$D_{A_2}^{[211]}K_{A_2}^{[100]}$	$D_{A_1}^{[000]}K_{A_2}^{[200]}$
$D_{s\,A_2}^{[100]}\eta_{A_2}^{[100]}$	$D_{s\,A_2}^{[100]}\eta_{A_1}^{[000]}$	$D_{A_2}^{[110]}K_{A_2}^{[110]}$	$D_{s\,A_2}^{[111]}\eta_{A_1}^{[000]}$	$D_{A_2}^{[111]}K_{A_2}^{[111]}$
$D_{s\,A_2}^{[110]}\eta_{A_2}^{[110]}$	$D_{s\,A_1}^{[000]}\eta_{A_2}^{[100]}$	$D_{A_2}^{[100]}K_{A_2}^{[111]}$	$D_{s\,A_2}^{[110]}\eta_{A_2}^{[100]}$	$D_{s\,A_2}^{[200]}\eta_{A_1}^{[000]}$
	$D_{s\,A_1}^{*[100]}\sigma_{A_1}^{[000]}$	$D_{s\,A_2}^{[110]}\eta_{A_1}^{[000]}$	$D_{B_1}^{*[110]}K_{A_2}^{[100]}$	$D_{s\,A_2}^{[100]}\eta_{A_2}^{[100]}$
		$D_{s\,A_2}^{[100]}\eta_{A_2}^{[100]}$	$D_{s\,A_1}^{*[111]}\sigma_{A_1}^{[000]}$	$D_{s\,A_1}^{*[200]}\sigma_{A_1}^{[000]}$
		$D_{s\,A_1}^{*[110]}\sigma_{A_1}^{[000]}$		$D_{s\,A_1}^{*[100]}\sigma_{A_1}^{[100]}$
		$D_{E_2}^{*[100]}K_{A_2}^{[100]}$		
$(\bar{\psi}\mathbf{\Gamma}\psi)\times 18$	$(\bar{\psi}\mathbf{\Gamma}\psi)\times 32$	$(\bar{\psi}\mathbf{\Gamma}\psi)\times 52$	$(\bar{\psi}\mathbf{\Gamma}\psi)\times 36$	$(\bar{\psi}\mathbf{\Gamma}\psi)\times 32$

Table B.3: As Table B.1 but for the isospin-0 charm-strange sector in Chapter 5. The momentum and irreps are labelled by $\vec{P}\Lambda^{(P)}$. The number of single-meson operators used is indicated by $(\bar{\psi}\mathbf{\Gamma}\psi)$ where $\mathbf{\Gamma}$ represents all combinations of Dirac gamma matrices and up to three (two) gauge covariant derivatives at rest (non-zero momentum).

$[000]T_1^-$	$[100]E_2$	$[110]B_1$	$[110]B2$	$[111]E_2$
$D_{A_2}^{[100]}K_{A_2}^{[100]}$	$D_{A_2}^{[110]}K_{A_2}^{[100]}$	$D_{A_2}^{[100]}K_{A_2}^{[100]}$	$D_{A_2}^{[111]}K_{A_2}^{[100]}$	$D_{A_2}^{[110]}K_{A_2}^{[100]}$
$D_{A_2}^{[110]}K_{A_2}^{[110]}$	$D_{A_2}^{[100]}K_{A_2}^{[110]}$	$D_{A_2}^{[210]}K_{A_2}^{[100]}$	$D_{A_2}^{[110]}K_{A_2}^{[110]}$	$D_{A_2}^{[100]}K_{A_2}^{[110]}$
$D^{*[100]}_{E2}K_{A_2}^{[100]}$	$D^{*[000]}_{T_1}K_{A_2}^{[100]}$	$D_{A_2}^{[110]}K_{A_2}^{[110]}$	$D^{*[110]}_{B_1}K_{A_1}^{[000]}$	$D^{*[111]}_{E_2}K_{A_1}^{[000]}$
$D_{sA_2}^{[100]}\eta_{A_2}^{[100]}$	$D^{*[100]}_{E_2}K_{A_1}^{[000]}$	$D^{*[110]}_{B_2}K_{A_1}^{[000]}$	$D^{*[100]}_{A_1}K_{A_2}^{[100]}$	$D_{sA_2}^{[110]}\sigma_{A_1}^{[100]}$
$D_s^*[000]_{T_1}\sigma_{A_1}^{[000]}$	$D^{*[100]}_{sE2}\sigma_{A_1}^{[000]}$	$D^{*[110]}_{sB_1}\sigma_{A_1}^{[000]}$	$D^{*[100]}_{E_2}K_{A_2}^{[100]}$	
	$D_{sA_2}^{[110]}\sigma_{A_1}^{[100]}$	$D_{sA_2}^{[111]}\sigma_{A_1}^{[100]}$	$D^{*[110]}_{sB_2}\sigma_{A_1}^{[000]}$	
$(\bar{\psi}\mathbf{\Gamma}\psi)\times 17$	$(\bar{\psi}\mathbf{\Gamma}\psi)\times 52$	$(\bar{\psi}\mathbf{\Gamma}\psi)\times 52$	$(\bar{\psi}\mathbf{\Gamma}\psi)\times 52$	$(\bar{\psi}\mathbf{\Gamma}\psi)\times 68$

Table B.4: As Table B.3 but all single-meson operators run up to two derivatives.

Appendix C

List of Parametrisations

The eight parametrisations that successfully reproduced the finite-volume spectrum, that gave $\chi^2/N_{\text{dof}} < 1.6$ and no parameters were statistically consistent with zero, of the DK scattering amplitudes in Chapter 5 are listed here. All parametrisations of the P-wave amplitudes contain only one pole term so the parametrisations will be described by the S-wave parametrisations. All K-matrix parametrisations will use the Chew-Mandelstam prescription with subtraction at the pole of the K-matrix.

Besides these parametrisations, other forms with all combinations up to $N_g = N_\gamma = 1$ were attempted but it was found that they did not improve the fit or gave parameters statistically consistent with zero. These are not listed here.

C.1 Parametrisation one

The S-wave amplitude is parametrised by an effective range expansion, $k \cot \delta_0 = 1/a_0$, where the a_0 is the scattering length. The parameters are given in Equation (5.27). The effective range term was found to be statistically consistent with zero and not included.

C.2 Parametrisation two

The K-matrix in S-wave has the form $K(s) = \frac{(g^{(0)})^2}{m^2 - s} + \gamma^{(0)}$, and the parameters are given in Equation (5.26).

C.3 Parametrisation three

The K-matrix has the form $K = \frac{g^{(0)}}{m^2-s} + \gamma^{(1)}s$, and the parameters are

$$\begin{aligned} g_0^{(0)} &= 0.667 \pm 0.034 \pm 0.011 \\ \gamma_0^{(1)} &= 6.6 \pm 0.8 \pm 0.3 \\ m_0 &= (0.82 \pm 0.09 \pm 0.06) \\ g_1 &= 2.1 \pm 0.3 \pm 0.1 \\ m_1 &= (0.34445 \pm 0.00011 \pm 0.00006) \cdot a_t^{-1} \\ & \chi^2/N_{\text{dof}} = \tfrac{26.74}{23-5} = 1.49. \end{aligned} \qquad \begin{bmatrix} 1 & -0.86 & -0.31 & -0.03 & -0.02 \\ & 1 & -0.74 & 0.22 & 0.07 \\ & & 1 & -0.43 & -0.14 \\ & & & 1 & 0.15 \\ & & & & 1 \end{bmatrix} \tag{C.1}$$

C.4 Parametrisation four

The K-matrix has the form $K = \frac{(g^{(0)})^2}{m^2-s} + \gamma^{(0)} + \gamma^{(1)}s$ and the parameters are

$$\begin{aligned} g_0^{(0)} &= 1.33 \pm 0.03 \pm 0.01 \\ \gamma_0^{(0)} &= -2.49 \pm 0.11 \pm 0.2 \\ \gamma_0^{(1)} &= 1.7 \pm 0.8 \pm 0.8 \\ m_0 &= (0.82 \pm 0.09 \pm 0.06) \\ g_1 &= 2.1 \pm 0.3 \pm 0.1 \\ m_1 &= (0.34445 \pm 0.00011 \pm 0.00006) \cdot a_t^{-1} \\ & \chi^2/N_{\text{dof}} = \tfrac{26.68}{23-6} = 1.57. \end{aligned} \qquad \begin{bmatrix} 1 & -0.72 & -0.70 & 0.39 & 0.01 & 0.00 \\ & 1 & 0.17 & -0.04 & 0.04 & 0.00 \\ & & 1 & -0.03 & -0.09 & -0.04 \\ & & & 1 & 0.02 & 0.03 \\ & & & & 1 & 0.10 \\ & & & & & 1 \end{bmatrix} \tag{C.2}$$

C.5 Parametrisation five

The K-matrix has the form $K = \frac{(g^{(0)}+g^{(1)}s)^2}{m^2-s}$ and the parameters are

$$\begin{aligned} g_0^{(0)} &= 0.76 \pm 0.03 \pm 0.36 \\ g_0^{(1)} &= 1.3 \pm 0.2 \pm 2.2 \\ m_0 &= (0.76 \pm 0.03 \pm 0.24) \\ g_1 &= 2.1 \pm 0.3 \pm 0.1 \\ m_1 &= (0.34445 \pm 0.00011 \pm 0.00006) \cdot a_t^{-1} \\ & \chi^2/N_{\text{dof}} = \tfrac{26.65}{23-5} = 1.48. \end{aligned} \qquad \begin{bmatrix} 1 & -0.85 & 0.55 & 0.18 & 0.05 \\ & 1 & -0.04 & -0.26 & -0.09 \\ & & 1 & -0.01 & 0.01 \\ & & & 1 & 0.12 \\ & & & & 1 \end{bmatrix} \tag{C.3}$$

C.6 Parametrisation six

The K-matrix has the form $K = \frac{(g^{(0)}+g^{(1)}s)^2}{m^2-s} + \gamma^{(0)}$ and the parameters are

$$\begin{aligned} g_0^{(0)} &= 1.12 \pm 0.03 \pm 4.8 \\ g_0^{(1)} &= 0.3 \pm 0.2 \pm 24.5 \\ \gamma_0^{(0)} &= -2.1 \pm 0.2 \pm 4.8 \\ m_0 &= (0.643 \pm 0.011 \pm 0.033) \\ g_1 &= 2.1 \pm 0.3 \pm 1.1 \\ m_1 &= (0.34445 \pm 0.00011 \pm 0.00006) \cdot a_t^{-1} \\ & \chi^2/N_{\text{dof}} = \tfrac{26.71}{23-6} = 1.57. \end{aligned} \qquad \begin{bmatrix} 1 & -0.65 & -0.62 & 0.30 & 0.03 & 0.01 \\ & 1 & 0.03 & 0.06 & -0.19 & -0.07 \\ & & 1 & 0.19 & 0.08 & 0.02 \\ & & & 1 & -0.02 & 0.01 \\ & & & & 1 & 0.10 \\ & & & & & 1 \end{bmatrix} \tag{C.4}$$

C.7 Parametrisation seven

The K-matrix has the form $K = \frac{(g^{(0)}+g^{(1)}s)^2}{m^2-s} + \gamma^{(1)}s$ and the parameters are

$$\begin{aligned}
g_0^{(0)} &= 0.53 \pm 0.04 \pm 0.76 \\
g_0^{(1)} &= 1.3 \pm 0.3 \pm 2.9 \\
\gamma_0^{(1)} &= 6.8 \pm 1.6 \pm 34.5 \\
m_0 &= (0.66 \pm 0.09 \pm 0.22) \\
g_1 &= 2.1 \pm 0.3 \pm 0.2 \\
m_1 &= (0.34445 \pm 0.00012 \pm 0.00006) \cdot a_t^{-1} \\
&\chi^2/N_{\mathrm{dof}} = \tfrac{26.75}{23-6} = 1.57.
\end{aligned}
\qquad
\begin{bmatrix}
1 & -0.58 & -0.56 & 0.27 & -0.04 & -0.02 \\
 & 1 & 0.00 & -0.47 & 0.06 & 0.01 \\
 & & 1 & -0.64 & 0.32 & 0.10 \\
 & & & 1 & -0.46 & -0.15 \\
 & & & & 1 & 0.16 \\
 & & & & & 1
\end{bmatrix}
\tag{C.5}$$

C.8 Parametrisation eight

The K-matrix has the form $K = \frac{(g^{(1)}s)^2}{m^2-s} + \gamma^{(1)}s$ and the parameters are

$$\begin{aligned}
g_0^{(0)} &= 3.1 \pm 0.6 \pm 0.2 \\
\gamma_0^{(1)} &= 19 \pm 2 \pm 2 \\
m_0 &= (0.59 \pm 0.03 \pm 0.01) \\
g_1 &= 2.1 \pm 0.3 \pm 0.2 \\
m_1 &= (0.34445 \pm 0.00012 \pm 0.00007) \cdot a_t^{-1} \\
&\chi^2/N_{\mathrm{dof}} = \tfrac{26.83}{23-5} = 1.49.
\end{aligned}
\qquad
\begin{bmatrix}
1 & 0.18 & -0.77 & 0.04 & 0.00 \\
 & 1 & -0.75 & 0.31 & 0.09 \\
 & & 1 & -0.25 & -0.08 \\
 & & & 1 & 0.12 \\
 & & & & 1
\end{bmatrix}
\tag{C.6}$$

Bibliography

[1] **SciDAC** Collaboration, R. G. Edwards and B. Joó, "The chroma software system for lattice qcd," *Nucl. Phys. B. Proc. Suppl.* **140** (2005) 832, hep-lat/0409003.

[2] M. A. Clark, R. Babich, K. Barros, R. C. Brower, and C. Rebbi, "Solving Lattice QCD systems of equations using mixed precision solvers on GPUs," *Comput. Phys. Commun.* **181** (2010) 1517–1528, arXiv:0911.3191 [hep-lat].

[3] R. Babich, M. A. Clark, and B. Joó, "Parallelizing the QUDA Library for Multi-GPU Calculations in Lattice Quantum Chromodynamics," in *International Conference for High Performance Computing, Networking, Storage and Analysis (SC)*, pp. 1–11. 2010. arXiv:1011.0024 [hep-lat].

[4] B. Joó, D. Kalamkar, K. Vaidyanathan, M. Smelyanskiy, K. Pamnany, V. Lee, P. Dubey, and W. Watson, "Lattice qcd on intel xeon phitm coprocessors," in *Supercomputing*, J. Kunkel, T. Ludwig, and H. Meuer, eds., vol. 7905 of *Lecture Notes in Computer Science*, pp. 40–54. Springer Berlin Heidelberg, 2013.

[5] J. Osborn, R. Babich, J. Brannick, R. Brower, M. Clark, *et al.*, "Multigrid solver for clover fermions," *PoS* **LATTICE2010** (2010) 037, arXiv:1011.2775 [hep-lat].

[6] R. Babich, J. Brannick, R. Brower, M. Clark, T. Manteuffel, *et al.*, "Adaptive multigrid algorithm for the lattice Wilson-Dirac operator," *Phys.Rev.Lett.* **105** (2010) 201602, arXiv:1005.3043 [hep-lat].

[7] M. Gell-Mann, "A Schematic Model of Baryons and Mesons," *Phys. Lett.* **8** (1964) 214–215.

[8] G. Zweig, "An SU(3) model for strong interaction symmetry and its breaking," *CERN-TH-401* (1964) .

[9] D. J. Gross and F. Wilczek, "Ultraviolet Behavior of Nonabelian Gauge Theories," *Phys. Rev. Lett.* **30** (1973) 1343–1346.

[10] H. D. Politzer, "Reliable Perturbative Results for Strong Interactions?," *Phys. Rev. Lett.* **30** (1973) 1346–1349.

[11] S. Godfrey and N. Isgur, "Mesons in a Relativized Quark Model with Chromodynamics," *Phys. Rev.* **D32** (1985) 189–231.

[12] **IHEP-Brussels-Los Alamos-Annecy(LAPP)** Collaboration, D. Alde *et al.*, "Evidence for a 1^{-+} Exotic Meson," *Phys. Lett.* **B205** (1988) 397.

[13] **COMPASS** Collaboration, M. Alekseev *et al.*, "Observation of a $J^PC = 1^{-+}$ exotic resonance in diffractive dissociation of 190 GeV/c π^- into $\pi^-\pi^-\pi^+$," *Phys. Rev. Lett.* **104** (2010) 241803, arXiv:0910.5842 [hep-ex].

[14] T. Barnes, S. Godfrey, and E. S. Swanson, "Higher charmonia," *Phys. Rev.* **D72** (2005) 054026, arXiv:hep-ph/0505002 [hep-ph].

[15] **Particle Data Group** Collaboration, C. Patrignani *et al.*, "Review of Particle Physics," *Chin. Phys.* **C40** no. 10, (2016) 100001.

[16] **Belle** Collaboration, S. K. Choi *et al.*, "Observation of a narrow charmonium - like state in exclusive $B^\pm \to K^\pm\pi^+\pi^- J/\psi$ decays," *Phys. Rev. Lett.* **91** (2003) 262001, arXiv:hep-ex/0309032 [hep-ex].

[17] **LHCb** Collaboration, R. Aaij *et al.*, "Observation of $J/\psi\phi$ structures consistent with exotic states from amplitude analysis of $B^+ \to J/\psi\phi K^+$ decays," *Phys. Rev. Lett.* **118** no. 2, (2017) 022003, arXiv:1606.07895 [hep-ex].

[18] R. F. Lebed, R. E. Mitchell, and E. S. Swanson, "Heavy-Quark QCD Exotica," *Prog. Part. Nucl. Phys.* **93** (2017) 143–194, arXiv:1610.04528 [hep-ph].

[19] H.-X. Chen, W. Chen, X. Liu, Y.-R. Liu, and S.-L. Zhu, "A review of the open charm and open bottom systems," *Rept. Prog. Phys.* **80** no. 7, (2017) 076201, arXiv:1609.08928 [hep-ph].

[20] V. Mathieu, N. Kochelev, and V. Vento, "The Physics of Glueballs," *Int. J. Mod. Phys.* **E18** (2009) 1–49, arXiv:0810.4453 [hep-ph].

[21] C. A. Meyer and E. S. Swanson, "Hybrid Mesons," *Prog. Part. Nucl. Phys.* **82** (2015) 21–58, arXiv:1502.07276 [hep-ph].

[22] A. Esposito, A. Pilloni, and A. D. Polosa, "Multiquark Resonances," *Phys. Rept.* **668** (2016) 1–97, arXiv:1611.07920 [hep-ph].

[23] H.-X. Chen, W. Chen, X. Liu, and S.-L. Zhu, "The hidden-charm pentaquark and tetraquark states," *Phys. Rept.* **639** (2016) 1–121, arXiv:1601.02092 [hep-ph].

[24] F.-K. Guo, C. Hanhart, U.-G. Meiner, Q. Wang, Q. Zhao, and B.-S. Zou, "Hadronic molecules," *Rev. Mod. Phys.* **90** no. 1, (2018) 015004, arXiv:1705.00141 [hep-ph].

[25] E. S. Swanson, "Cusps and Exotic Charmonia," *Int. J. Mod. Phys.* **E25** no. 07, (2016) 1642010, arXiv:1504.07952 [hep-ph].

[26] K. G. Wilson, "Confinement of Quarks," *Phys. Rev.* **D10** (1974) 2445–2459.

[27] C. Aubin, C. Bernard, C. DeTar, J. Osborn, S. Gottlieb, E. B. Gregory, D. Toussaint, U. M. Heller, J. E. Hetrick, and R. Sugar, "Light hadrons with improved staggered quarks: Approaching the continuum limit," *Phys. Rev.* **D70** (2004) 094505, arXiv:hep-lat/0402030 [hep-lat].

[28] **PACS-CS** Collaboration, S. Aoki *et al.*, "2+1 Flavor Lattice QCD toward the Physical Point," *Phys. Rev.* **D79** (2009) 034503, arXiv:0807.1661 [hep-lat].

[29] **MILC** Collaboration, A. Bazavov *et al.*, "Nonperturbative QCD Simulations with 2+1 Flavors of Improved Staggered Quarks," *Rev. Mod. Phys.* **82** (2010) 1349–1417, arXiv:0903.3598 [hep-lat].

[30] **PACS-CS** Collaboration, Y. Namekawa *et al.*, "Charm quark system at the physical point of 2+1 flavor lattice QCD," *Phys. Rev.* **D84** (2011) 074505, arXiv:1104.4600 [hep-lat].

[31] C. McNeile, C. T. H. Davies, E. Follana, K. Hornbostel, and G. P. Lepage, "Heavy meson masses and decay constants from relativistic heavy quarks in full lattice QCD," *Phys. Rev.* **D86** (2012) 074503, arXiv:1207.0994 [hep-lat].

[32] R. J. Dowdall, C. T. H. Davies, T. C. Hammant, and R. R. Horgan, "Precise heavy-light meson masses and hyperfine splittings from lattice QCD including charm quarks in the sea," *Phys. Rev.* **D86** (2012) 094510, arXiv:1207.5149 [hep-lat].

[33] G. C. Donald, C. T. H. Davies, R. J. Dowdall, E. Follana, K. Hornbostel, J. Koponen, G. P. Lepage, and C. McNeile, "Precision tests of the J/ψ from full lattice QCD: mass, leptonic width and radiative decay rate to η_c," *Phys. Rev.* **D86** (2012) 094501, arXiv:1208.2855 [hep-lat].

[34] S. Durr *et al.*, "Ab-Initio Determination of Light Hadron Masses," *Science* **322** (2008) 1224–1227, arXiv:0906.3599 [hep-lat].

[35] S. Borsanyi *et al.*, "Ab initio calculation of the neutron-proton mass difference," *Science* **347** (2015) 1452–1455, arXiv:1406.4088 [hep-lat].

[36] M. Lüscher, "Volume Dependence of the Energy Spectrum in Massive Quantum Field Theories. 1. Stable Particle States," *Commun. Math. Phys.* **104** (1986) 177.

[37] M. Lüscher, "Volume Dependence of the Energy Spectrum in Massive Quantum Field Theories. 2. Scattering States," *Commun. Math. Phys.* **105** (1986) 153–188.

[38] M. Lüscher, "Two particle states on a torus and their relation to the scattering matrix," *Nucl. Phys.* **B354** (1991) 531–578.

[39] M. Lüscher, "Signatures of unstable particles in finite volume," *Nucl. Phys.* **B364** (1991) 237–251.

[40] K. Polejaeva and A. Rusetsky, "Three particles in a finite volume," *Eur. Phys. J.* **A48** (2012) 67, arXiv:1203.1241 [hep-lat].

[41] R. A. Briceno and Z. Davoudi, "Three-particle scattering amplitudes from a finite volume formalism," *Phys. Rev.* **D87** no. 9, (2013) 094507, arXiv:1212.3398 [hep-lat].

[42] M. T. Hansen and S. R. Sharpe, "Relativistic, model-independent, three-particle quantization condition," *Phys. Rev.* **D90** no. 11, (2014) 116003, arXiv:1408.5933 [hep-lat].

[43] M. T. Hansen and S. R. Sharpe, "Expressing the three-particle finite-volume spectrum in terms of the three-to-three scattering amplitude," *Phys. Rev.* **D92** no. 11, (2015) 114509, arXiv:1504.04248 [hep-lat].

[44] D. Mohler, C. B. Lang, L. Leskovec, S. Prelovsek, and R. M. Woloshyn, "$D^*_{s0}(2317)$ Meson and D-Meson-Kaon Scattering from Lattice QCD," *Phys. Rev. Lett.* **111** no. 22, (2013) 222001, arXiv:1308.3175 [hep-lat].

[45] C. B. Lang, L. Leskovec, D. Mohler, S. Prelovsek, and R. M. Woloshyn, "D_s mesons with DK and D^*K scattering near threshold," *Phys. Rev.* **D90** no. 3, (2014) 034510, arXiv:1403.8103 [hep-lat].

[46] C. B. Lang, L. Leskovec, D. Mohler, and S. Prelovsek, "Vector and scalar charmonium resonances with lattice QCD," *JHEP* **09** (2015) 089, arXiv:1503.05363 [hep-lat].

[47] G. Moir, M. Peardon, S. M. Ryan, C. E. Thomas, and D. J. Wilson, "Coupled-Channel $D\pi$, $D\eta$ and $D_s\bar{K}$ Scattering from Lattice QCD," *JHEP* **10** (2016) 011, arXiv:1607.07093 [hep-lat].

[48] G. S. Bali, S. Collins, A. Cox, and A. Schfer, "Masses and decay constants of the $D^*_{s0}(2317)$ and $D_{s1}(2460)$ from $N_f = 2$ lattice QCD close to the physical point," *Phys. Rev.* **D96** no. 7, (2017) 074501, arXiv:1706.01247 [hep-lat].

[49] J. J. Dudek, R. G. Edwards, and D. G. Richards, "Radiative transitions in charmonium from lattice QCD," *Phys. Rev.* **D73** (2006) 074507, arXiv:hep-ph/0601137 [hep-ph].

[50] J. J. Dudek, R. Edwards, and C. E. Thomas, "Exotic and excited-state radiative transitions in charmonium from lattice QCD," *Phys. Rev.* **D79** (2009) 094504, arXiv:0902.2241 [hep-ph].

[51] M. Creutz, *Quarks, Gluons and Lattices*. Cambridge Monographs on Mathem. Cambridge University Press, 1985.

[52] I. Montvay and G. Münster, *Quantum fields on a lattice*. Cambridge monographs on mathematical physics. Cambridge Univ. Press, Cambridge, 1994.

[53] C. Gattringer and C. Lang, *Quantum Chromodynamics on the Lattice: An Introductory Presentation*. Lecture Notes in Physics. Springer, 2009.

[54] G. P. Lepage and P. B. Mackenzie, "On the viability of lattice perturbation theory," *Phys. Rev.* **D48** (1993) 2250–2264, arXiv:hep-lat/9209022 [hep-lat].

[55] M. Lüscher and P. Weisz, "Computation of the Action for On-Shell Improved Lattice Gauge Theories at Weak Coupling," *Phys. Lett.* **158B** (1985) 250–254.

[56] C. Morningstar, "Improved gluonic actions on anisotropic lattices," *Nucl. Phys. Proc. Suppl.* **53** (1997) 914–916, arXiv:hep-lat/9608019 [hep-lat].

[57] B. Sheikholeslami and R. Wohlert, "Improved Continuum Limit Lattice Action for QCD with Wilson Fermions," *Nucl. Phys.* **B259** (1985) 572.

[58] P. Chen, "Heavy quarks on anisotropic lattices: The Charmonium spectrum," *Phys. Rev.* **D64** (2001) 034509, arXiv:hep-lat/0006019 [hep-lat].

[59] M. Lüscher, S. Sint, R. Sommer, P. Weisz, and U. Wolff, "Nonperturbative O(a) improvement of lattice QCD," *Nucl. Phys.* **B491** (1997) 323–343, arXiv:hep-lat/9609035 [hep-lat].

[60] C. Morningstar and M. J. Peardon, "Analytic smearing of SU(3) link variables in lattice QCD," *Phys. Rev.* **D69** (2004) 054501, arXiv:hep-lat/0311018 [hep-lat].

[61] R. G. Edwards, B. Joo, and H.-W. Lin, "Tuning for Three-flavors of Anisotropic Clover Fermions with Stout-link Smearing," *Phys. Rev.* **D78** (2008) 054501, arXiv:0803.3960 [hep-lat].

[62] **Hadron Spectrum** Collaboration, H.-W. Lin *et al.*, "First results from 2+1 dynamical quark flavors on an anisotropic lattice: Light-hadron spectroscopy and setting the strange-quark mass," *Phys. Rev.* **D79** (2009) 034502, arXiv:0810.3588 [hep-lat].

[63] **ALPHA** Collaboration, F. Knechtli, T. Korzec, B. Leder, and G. Moir, "Power corrections from decoupling of the charm quark," *Phys. Lett.* **B774** (2017) 649–655, arXiv:1706.04982 [hep-lat].

[64] C. Michael, "Adjoint Sources in Lattice Gauge Theory," *Nucl. Phys.* **B259** (1985) 58.

[65] M. Lüscher and U. Wolff, "How to calculate the elastic scattering matrix in two-dimensional quantum field theories by numerical simulation," *Nucl. Phys.* **B339** (1990) 222–252.

[66] B. Blossier, M. Della Morte, G. von Hippel, T. Mendes, and R. Sommer, "On the generalized eigenvalue method for energies and matrix elements in lattice field theory," *JHEP* **04** (2009) 094, arXiv:0902.1265 [hep-lat].

[67] J. J. Dudek, R. G. Edwards, and C. E. Thomas, "S and D-wave phase shifts in isospin-2 $\pi\pi$ scattering from lattice QCD," *Phys.Rev.* **D86** (2012) 034031, arXiv:1203.6041 [hep-ph].

[68] J. J. Dudek, R. G. Edwards, N. Mathur, and D. G. Richards, "Charmonium excited state spectrum in lattice QCD," *Phys. Rev.* **D77** (2008) 034501, arXiv:0707.4162 [hep-lat].

[69] J. J. Dudek, R. G. Edwards, M. J. Peardon, D. G. Richards, and C. E. Thomas, "Toward the excited meson spectrum of dynamical QCD," *Phys. Rev.* **D82** (2010) 034508, arXiv:1004.4930 [hep-ph].

[70] C. E. Thomas, R. G. Edwards, and J. J. Dudek, "Helicity operators for mesons in flight on the lattice," *Phys. Rev.* **D85** (2012) 014507, arXiv:1107.1930 [hep-lat].

[71] R. C. Johnson, "Angular momentum on a lattice," *Phys. Lett.* **114B** (1982) 147–151.

[72] **Lattice Hadron Physics (LHPC)** Collaboration, S. Basak, R. Edwards, G. T. Fleming, U. M. Heller, C. Morningstar, D. Richards, I. Sato, and S. J. Wallace, "Clebsch-Gordan construction of lattice interpolating fields for excited baryons," *Phys. Rev.* **D72** (2005) 074501, arXiv:hep-lat/0508018 [hep-lat].

[73] D. C. Moore and G. T. Fleming, "Angular momentum on the lattice: the case of non-zero linear momentum," *Phys. Rev.* **D73** (2006) 014504, arXiv:hep-lat/0507018 [hep-lat]. [Erratum: Phys. Rev.D74,079905(2006)].

[74] **Hadron Spectrum** Collaboration, M. Peardon, J. Bulava, J. Foley, C. Morningstar, J. Dudek, R. G. Edwards, B. Joo, H.-W. Lin, D. G. Richards, and K. J. Juge, "A novel quark-field creation operator construction for hadronic physics in lattice QCD," *Phys. Rev.* **D80** (2009) 054506, arXiv:0905.2160 [hep-lat].

[75] D. J. Wilson, R. A. Briceno, J. J. Dudek, R. G. Edwards, and C. E. Thomas, "Coupled $\pi\pi, K\bar{K}$ scattering in P-wave and the ρ resonance from lattice QCD," *Phys. Rev.* **D92** no. 9, (2015) 094502, arXiv:1507.02599 [hep-ph].

[76] **Hadron Spectrum** Collaboration, L. Liu, G. Moir, M. Peardon, S. M. Ryan, C. E. Thomas, P. Vilaseca, J. J. Dudek, R. G. Edwards, B. Joo, and D. G. Richards, "Excited and exotic charmonium spectroscopy from lattice QCD," *JHEP* **07** (2012) 126, arXiv:1204.5425 [hep-ph].

[77] **Hadron Spectrum** Collaboration, G. K. C. Cheung, C. O'Hara, G. Moir, M. Peardon, S. M. Ryan, C. E. Thomas, and D. Tims, "Excited and exotic charmonium, D_s and D meson spectra for two light quark masses from lattice QCD," *JHEP* **12** (2016) 089, arXiv:1610.01073 [hep-lat].

[78] **Particle Data Group** Collaboration, K. A. Olive *et al.*, "Review of Particle Physics," *Chin. Phys.* **C38** (2014) 090001 and 2015 update.

[79] R. G. Edwards, J. J. Dudek, D. G. Richards, and S. J. Wallace, "Excited state baryon spectroscopy from lattice QCD," *Phys. Rev.* **D84** (2011) 074508, arXiv:1104.5152 [hep-ph].

[80] L. Levkova and C. DeTar, "Charm annihilation effects on the hyperfine splitting in charmonium," *Phys. Rev.* **D83** (2011) 074504, arXiv:1012.1837 [hep-lat].

[81] Z. Davoudi and M. J. Savage, "Restoration of Rotational Symmetry in the Continuum Limit of Lattice Field Theories," *Phys. Rev.* **D86** (2012) 054505, arXiv:1204.4146 [hep-lat].

[82] G. S. Bali, S. Collins, and C. Ehmann, "Charmonium spectroscopy and mixing with light quark and open charm states from n_F=2 lattice QCD," *Phys. Rev.* **D84** (2011) 094506, arXiv:1110.2381 [hep-lat].

[83] K. Cichy, M. Kalinowski, and M. Wagner, "Continuum limit of the D meson, D_s meson and charmonium spectrum from $N_f = 2 + 1 + 1$ twisted mass lattice QCD," *Phys. Rev.* **D94** no. 9, (2016) 094503, arXiv:1603.06467 [hep-lat].

[84] J. J. Dudek and E. Rrapaj, "Charmonium in lattice QCD and the non-relativistic quark-model," *Phys. Rev.* **D78** (2008) 094504, arXiv:0809.2582 [hep-ph].

[85] J. J. Dudek, "The lightest hybrid meson supermultiplet in QCD," *Phys. Rev.* **D84** (2011) 074023, arXiv:1106.5515 [hep-ph].

[86] T. Barnes, F. E. Close, F. de Viron, and J. Weyers, "Q anti-Q G Hermaphrodite Mesons in the MIT Bag Model," *Nucl. Phys.* **B224** (1983) 241.

[87] M. S. Chanowitz and S. R. Sharpe, "Hybrids: Mixed States of Quarks and Gluons," *Nucl. Phys.* **B222** (1983) 211–244. [Erratum: Nucl. Phys.B228,588(1983)].

[88] P. Guo, A. P. Szczepaniak, G. Galata, A. Vassallo, and E. Santopinto, "Heavy quarkonium hybrids from Coulomb gauge QCD," *Phys. Rev.* **D78** (2008) 056003, arXiv:0807.2721 [hep-ph].

[89] N. Isgur and J. E. Paton, "A Flux Tube Model for Hadrons in QCD," *Phys. Rev.* **D31** (1985) 2910.

[90] **MILC** Collaboration, C. W. Bernard *et al.*, "Exotic mesons in quenched lattice QCD," *Phys. Rev.* **D56** (1997) 7039–7051, arXiv:hep-lat/9707008 [hep-lat].

[91] J. J. Dudek, R. G. Edwards, B. Joo, M. J. Peardon, D. G. Richards, and C. E. Thomas, "Isoscalar meson spectroscopy from lattice QCD," *Phys. Rev.* **D83** (2011) 111502, arXiv:1102.4299 [hep-lat].

[92] J. J. Dudek and R. G. Edwards, "Hybrid Baryons in QCD," *Phys. Rev.* **D85** (2012) 054016, arXiv:1201.2349 [hep-ph].

[93] G. Moir, M. Peardon, S. M. Ryan, C. E. Thomas, and L. Liu, "Excited spectroscopy of charmed mesons from lattice QCD," *JHEP* **05** (2013) 021, arXiv:1301.7670 [hep-ph].

[94] **Hadron Spectrum** Collaboration, J. J. Dudek, R. G. Edwards, and C. E. Thomas, "Energy dependence of the ρ resonance in $\pi\pi$ elastic scattering from lattice QCD," *Phys. Rev.* **D87** no. 3, (2013) 034505, arXiv:1212.0830 [hep-ph]. [Erratum: Phys. Rev.D90,no.9,099902(2014)].

[95] **Hadron Spectrum** Collaboration, J. J. Dudek, R. G. Edwards, C. E. Thomas, and D. J. Wilson, "Resonances in coupled $\pi K - \eta K$ scattering from quantum chromodynamics," *Phys. Rev. Lett.* **113** no. 18, (2014) 182001, arXiv:1406.4158 [hep-ph].

[96] D. J. Wilson, J. J. Dudek, R. G. Edwards, and C. E. Thomas, "Resonances in coupled $\pi K, \eta K$ scattering from lattice QCD," *Phys. Rev.* **D91** no. 5, (2015) 054008, arXiv:1411.2004 [hep-ph].

[97] **Hadron Spectrum** Collaboration, J. J. Dudek, R. G. Edwards, and D. J. Wilson, "An a_0 resonance in strongly coupled $\pi\eta$, $K\overline{K}$ scattering from lattice QCD," *Phys. Rev.* **D93** no. 9, (2016) 094506, arXiv:1602.05122 [hep-ph].

[98] R. A. Briceno, J. J. Dudek, R. G. Edwards, and D. J. Wilson, "Isoscalar $\pi\pi$ scattering and the σ meson resonance from QCD," *Phys. Rev. Lett.* **118** no. 2, (2017) 022002, arXiv:1607.05900 [hep-ph].

[99] R. A. Briceno, J. J. Dudek, R. G. Edwards, and D. J. Wilson, "Isoscalar $\pi\pi, K\overline{K}, \eta\eta$ scattering and the σ, f_0, f_2 mesons from QCD," *Phys. Rev.* **D97** no. 5, (2018) 054513, arXiv:1708.06667 [hep-lat].

[100] A. J. Woss, C. E. Thomas, J. J. Dudek, R. G. Edwards, and D. J. Wilson, "Dynamically-coupled partial-waves in $\rho\pi$ isospin-2 scattering from lattice QCD," arXiv:1802.05580 [hep-lat].

[101] S. Prelovsek, C. B. Lang, L. Leskovec, and D. Mohler, "Study of the Z_c^+ channel using lattice QCD," *Phys. Rev.* **D91** no. 1, (2015) 014504, arXiv:1405.7623 [hep-lat].

[102] A. L. Guerrieri, M. Papinutto, A. Pilloni, A. D. Polosa, and N. Tantalo, "Flavored tetraquark spectroscopy," *PoS* **LATTICE2014** (2015) 106, arXiv:1411.2247 [hep-lat].

[103] M. Padmanath, C. B. Lang, and S. Prelovsek, "X(3872) and Y(4140) using diquark-antidiquark operators with lattice QCD," *Phys. Rev.* **D92** no. 3, (2015) 034501, arXiv:1503.03257 [hep-lat].

[104] **Hadron Spectrum** Collaboration, G. K. C. Cheung, C. E. Thomas, J. J. Dudek, and R. G. Edwards, "Tetraquark operators in lattice QCD and exotic flavour states in the charm sector," *JHEP* **11** (2017) 033, arXiv:1709.01417 [hep-lat].

[105] D. C. Moore and G. T. Fleming, "Multiparticle States and the Hadron Spectrum on the Lattice," *Phys. Rev.* **D74** (2006) 054504, arXiv:hep-lat/0607004 [hep-lat].

[106] J. J. de Swart, "The Octet model and its Clebsch-Gordan coefficients," *Rev. Mod. Phys.* **35** (1963) 916–939. [Erratum: Rev. Mod. Phys.37,326(1965)].

[107] T. A. Kaeding, "Tables of SU(3) isoscalar factors," *Atom. Data Nucl. Data Tabl.* **61** (1995) 233, arXiv:nucl-th/9502037 [nucl-th].

[108] **BESIII** Collaboration, M. Ablikim *et al.*, "Observation of a Charged Charmoniumlike Structure in $e^+e^- \to \pi^+\pi^- J/\psi$ at $\sqrt{s} = 4.26$GeV," *Phys. Rev. Lett.* **110** (2013) 252001, arXiv:1303.5949 [hep-ex].

[109] A. J. Woss and C. E. Thomas, "Utilising optimised operators and distillation to extract scattering phase shifts," *PoS* **LATTICE2016** (2016) 134, arXiv:1612.05437 [hep-lat].

[110] L. Maiani, F. Piccinini, A. D. Polosa, and V. Riquer, "Diquark-antidiquarks with hidden or open charm and the nature of X(3872)," *Phys. Rev.* **D71** (2005) 014028, arXiv:hep-ph/0412098 [hep-ph].

[111] L. Maiani, F. Piccinini, A. D. Polosa, and V. Riquer, "The Z(4430) and a New Paradigm for Spin Interactions in Tetraquarks," *Phys. Rev.* **D89** (2014) 114010, arXiv:1405.1551 [hep-ph].

[112] Y. Chen *et al.*, "Low-energy scattering of the $(D\bar{D}^*)^{\pm}$ system and the resonance-like structure $Z_c(3900)$," *Phys. Rev.* **D89** no. 9, (2014) 094506, arXiv:1403.1318 [hep-lat].

[113] **CLQCD** Collaboration, Y. Chen *et al.*, "Low-energy Scattering of $(D^*\bar{D}^*)^{\pm}$ System and the Resonance-like Structure $Z_c(4025)$," *Phys. Rev.* **D92** no. 5, (2015) 054507, arXiv:1503.02371 [hep-lat].

[114] **HAL QCD** Collaboration, Y. Ikeda, S. Aoki, T. Doi, S. Gongyo, T. Hatsuda, T. Inoue, T. Iritani, N. Ishii, K. Murano, and K. Sasaki, "Fate of the Tetraquark Candidate $Z_c(3900)$ from Lattice QCD," *Phys. Rev. Lett.* **117** no. 24, (2016) 242001, arXiv:1602.03465 [hep-lat].

[115] Y. Ikeda, B. Charron, S. Aoki, T. Doi, T. Hatsuda, T. Inoue, N. Ishii, K. Murano, H. Nemura, and K. Sasaki, "Charmed tetraquarks T_{cc} and T_{cs} from dynamical lattice QCD simulations," *Phys. Lett.* **B729** (2014) 85–90, arXiv:1311.6214 [hep-lat].

[116] A. Francis, R. J. Hudspith, R. Lewis, and K. Maltman, "Lattice Prediction for Deeply Bound Doubly Heavy Tetraquarks," *Phys. Rev. Lett.* **118** no. 14, (2017) 142001, arXiv:1607.05214 [hep-lat].

[117] **European Twisted Mass** Collaboration, P. Bicudo and M. Wagner, "Lattice QCD signal for a bottom-bottom tetraquark," *Phys. Rev.* **D87** no. 11, (2013) 114511, arXiv:1209.6274 [hep-ph].

[118] P. Bicudo, K. Cichy, A. Peters, B. Wagenbach, and M. Wagner, "Evidence for the existence of $ud\bar{b}\bar{b}$ and the non-existence of $ss\bar{b}\bar{b}$ and $cc\bar{b}\bar{b}$ tetraquarks from lattice QCD," *Phys. Rev.* **D92** no. 1, (2015) 014507, arXiv:1505.00613 [hep-lat].

[119] P. Bicudo, K. Cichy, A. Peters, and M. Wagner, "BB interactions with static bottom quarks from Lattice QCD," *Phys. Rev.* **D93** no. 3, (2016) 034501, arXiv:1510.03441 [hep-lat].

[120] A. Peters, P. Bicudo, L. Leskovec, S. Meinel, and M. Wagner, "Lattice QCD study of heavy-heavy-light-light tetraquark candidates," *PoS* **LATTICE2016** (2016) 104, arXiv:1609.00181 [hep-lat].

[121] P. Bicudo, M. Cardoso, A. Peters, M. Pflaumer, and M. Wagner, "$ud\bar{b}\bar{b}$ tetraquark resonances with lattice QCD potentials and the Born-Oppenheimer approximation," *Phys. Rev.* **D96** no. 5, (2017) 054510, arXiv:1704.02383 [hep-lat].

[122] M. Karliner and J. L. Rosner, "Discovery of doubly-charmed Ξ_{cc} baryon implies a stable $bb\bar{u}\bar{d}$ tetraquark," arXiv:1707.07666 [hep-ph].

[123] E. J. Eichten and C. Quigg, "Heavy-quark symmetry implies stable heavy tetraquark mesons $Q_iQ_j\bar{q}_k\bar{q}_l$," arXiv:1707.09575 [hep-ph].

[124] A. Czarnecki, B. Leng, and M. B. Voloshin, "Stability of tetrons," arXiv:1708.04594 [hep-ph].

[125] B. A. Thacker and G. P. Lepage, "Heavy quark bound states in lattice QCD," *Phys. Rev.* **D43** (1991) 196–208.

[126] A. X. El-Khadra, A. S. Kronfeld, and P. B. Mackenzie, "Massive fermions in lattice gauge theory," *Phys. Rev.* **D55** (1997) 3933–3957, arXiv:hep-lat/9604004 [hep-lat].

[127] **BaBar** Collaboration, B. Aubert *et al.*, "Observation of a narrow meson decaying to $D_s^+\pi^0$ at a mass of 2.32-GeV/c^2," *Phys. Rev. Lett.* **90** (2003) 242001, arXiv:hep-ex/0304021 [hep-ex].

[128] **Belle** Collaboration, K. Abe *et al.*, "Study of $B^- \to D^{**0}\pi^-(D^{**0} \to D^{(*)+}\pi^-)$ decays," *Phys. Rev.* **D69** (2004) 112002, arXiv:hep-ex/0307021 [hep-ex].

[129] **CLEO** Collaboration, D. Besson *et al.*, "Observation of a narrow resonance of mass 2.46 GeV/c^2 decaying to $D_s^{*+}\pi^0$ and confirmation of the $D_{sJ}^*(2317)$ state," *Phys. Rev.* **D68** (2003) 032002, arXiv:hep-ex/0305100 [hep-ex]. [Erratum: Phys. Rev.D75,119908(2007)].

[130] D. Mohler and R. M. Woloshyn, "D and D_s meson spectroscopy," *Phys. Rev.* **D84** (2011) 054505, arXiv:1103.5506 [hep-lat].

[131] S. D. Protopopescu, M. Alston-Garnjost, A. Barbaro-Galtieri, S. M. Flatte, J. H. Friedman, T. A. Lasinski, G. R. Lynch, M. S. Rabin, and F. T. Solmitz, "Pi pi Partial Wave Analysis from Reactions pi+ p —¿ pi+ pi- Delta++ and pi+ p —¿ K+ K- Delta++ at 7.1-GeV/c," *Phys. Rev.* **D7** (1973) 1279.

[132] R. J. Eden, P. V. Landshoff, D. I. Olive, and J. C. Polkinghorne, *The Analytic S-Matrix*. Cambridge University Press, May, 2002.

[133] K. Rummukainen and S. A. Gottlieb, "Resonance scattering phase shifts on a nonrest frame lattice," *Nucl. Phys.* **B450** (1995) 397–436, arXiv:hep-lat/9503028 [hep-lat].

[134] C. h. Kim, C. T. Sachrajda, and S. R. Sharpe, "Finite-volume effects for two-hadron states in moving frames," *Nucl. Phys.* **B727** (2005) 218–243, arXiv:hep-lat/0507006 [hep-lat].

[135] Z. Fu, "Rummukainen-Gottlieb's formula on two-particle system with different mass," *Phys. Rev.* **D85** (2012) 014506, arXiv:1110.0319 [hep-lat].

[136] L. Leskovec and S. Prelovsek, "Scattering phase shifts for two particles of different mass and non-zero total momentum in lattice QCD," *Phys. Rev.* **D85** (2012) 114507, arXiv:1202.2145 [hep-lat].

[137] M. T. Hansen and S. R. Sharpe, "Multiple-channel generalization of Lellouch-Lüscher formula," *Phys. Rev.* **D86** (2012) 016007, arXiv:1204.0826 [hep-lat].

[138] R. A. Briceno, "Two-particle multichannel systems in a finite volume with arbitrary spin," *Phys. Rev.* **D89** no. 7, (2014) 074507, arXiv:1401.3312 [hep-lat].

[139] P. Guo, R. Mitchell, and A. P. Szczepaniak, "The role of P-wave inelasticity in $J/\psi \to \pi^+\pi^-\pi^0$," *Phys. Rev.* **D82** (2010) 094002, arXiv:1006.4371 [hep-ph].

[140] G. F. Chew and S. Mandelstam, "Theory of low-energy pion pion interactions," *Phys. Rev.* **119** (1960) 467–477.

[141] S. Weinberg, "Evidence That the Deuteron Is Not an Elementary Particle," *Phys. Rev.* **137** (1965) B672–B678.

[142] D. Guo, A. Alexandru, R. Molina, and M. Dring, "Rho resonance parameters from lattice QCD," *Phys. Rev.* **D94** no. 3, (2016) 034501, arXiv:1605.03993 [hep-lat].

[143] R. L. Jaffe, "Exotica," *Phys. Rept.* **409** (2005) 1–45, arXiv:hep-ph/0409065 [hep-ph].